LINEAR AND CIRCULAR POLARIZED CIRCULAR ARRAY ANTENNAS UTILIZING ORBITAL ANGULAR MOMENTUM FOR WIRELESS APPLICATIONS AT 6.5 GHZ BAND

by
İREM AYLİN DURU

Submitted to the Graduate School of Engineering and Natural Sciences
in partial fulfilment of
the requirements for the degree of Master of Science

Sabancı University
July 2024

ABSTRACT

LINEAR AND CIRCULAR POLARIZED CIRCULAR ARRAY ANTENNAS UTILIZING ORBITAL ANGULAR MOMENTUM FOR WIRELESS APPLICATIONS AT 6.5 GHZ BAND

İREM AYLİN DURU

ELECTRONICS ENGINEERING M.S. THESIS, JULY 2024

Thesis Supervisor: Prof. İbrahim Tekin

Keywords: orbital angular momentum, linear and circular polarization, uniform circular array antennas, wireless communication

This thesis investigates the design, fabrication, and performance evaluation of circular array antennas capable of generating Orbital Angular Momentum (OAM) at 6.5 GHz. Two sets of 4-element circular antenna arrays, one for linear polarization and the other for circular polarization, were constructed using RO4003 material. HFSS simulations showed these antennas can double the capacity at 6.5 GHz by generating vortex waves with mode numbers $l = \pm 1$ and achieve gains over 4.4 dBi. The antennas were fabricated with an LPKF Circuit Board Plotter ProtoMat S63, ensuring high precision. Measurements in an anechoic chamber validated their performance, highlighting the superior spectral efficiency of circularly polarized antennas generating OAM. Prototypes were tested, demonstrating effective OAM-enabled radio links and phase distribution patterns consistent with vortex wave theory. This research advances OAM in wireless communications, showing its potential to enhance spectral efficiency and robustness. Future work includes developing a 4-port antenna by adding cross transmission lines and increasing the number of array elements to generate higher-order OAM modes.

ÖZET

6.5 GHZ BANDINDA KABLOSUZ UYGULAMALAR İÇİN YÖRÜNGESEL AÇISAL MOMENTUM KULLANAN LİNEER VE DAİRESEL POLARİZE DAİRESEL DİZİLİ ANTENLER

İREM AYLİN DURU

ELEKTRONİK MÜHENDİSLİĞİ YÜKSEK LİSANS TEZİ, TEMMUZ 2024

Tez Danışmanı: Prof. Dr. İbrahim Tekin

Anahtar Kelimeler: yörüngesel açısal momentum, doğrusal ve dairesel polarizasyon, düzgün dairesel dizili antenler, kablosuz iletişim

Bu tezde 6.5 GHz frekans bandında Yörüngesel Açısal Momentum (OAM) oluşturabilen dairesel dizi antenlerin tasarım, üretim ve performans değerlendirmesi incelenmektedir. RO4003 malzemesi kullanılarak, biri doğrusal polarizasyon, diğeri dairesel polarizasyon için olmak üzere iki set 4 elemanlı dairesel anten dizisi oluşturulmuştur. HFSS simülasyonları, bu antenlerin 6,5 GHz'de $l = \pm 1$ mod numaralı girdap dalgaları üreterek kapasiteyi iki katına çıkarabildiğini ve 4.4 dBi'nin üzerinde kazanç elde edebildiğini göstermiştir. Antenler, yüksek hassasiyet sağlayan LPKF Devre Kartı Çizici ProtoMat S63 ile üretilmiştir. Yankısız odada yapılan ölçümler, dairesel polarize antenlerin üstün spektral verimlilik ve enterferans dayanıklılığını vurgulayarak performanslarını doğrulamıştır. Yankısız odada yapılan ölçümler, antenlerin performansını doğrulamış ve OAM üreten dairesel polarizasyonlu antenlerin üstün spektral verimliliğini vurgulamıştır. Bu araştırma, OAM'nin kablosuz iletişimdeki uygulanabilirliğini artırarak spektral verimlilik ve dayanıklılığı iyileştirme potansiyelini ortaya koymaktadır. Gelecek çalışmalar, çapraz iletim hatları ekleyerek 4 portlu bir anten geliştirmeyi ve daha yüksek dereceli OAM modları üretmek için dizi eleman sayısını artırmayı içermektedir.

ACKNOWLEDGEMENTS

I would like to extend my sincere gratitude to my thesis supervisor, Prof. İbrahim Tekin. His unwavering support, insightful guidance, and precious expertise have been crucial to the completion of this thesis. His encouragement, dedication and feedbacks have significantly influenced my work and academic growth.

I would like to express my gratitude to Sabancı University for providing me with the opportunity to pursue a master's degree and for providing well-equipped facilities.

I would also like to extend my thanks to the professors I assisted as a TA, my students, and my fellow TA colleagues. Working with you all has been a uniquely enriching experience for me, I have learned a great deal from each of you.

I would like to thank the members of my thesis committee, Özgür Gürbüz and Sema Dumanlı Oktar for their time, valuable guidance and constructive feedback throughout review and evaluation process.

I am grateful to my dear friend Emre Baloğlu for his invaluable support, constant motivation, and reassurances, which gave me the strength to complete this thesis. Meeting Emre has been a pleasure, and I look forward to a lifelong friendship.

I want to express my gratitude to Kadir Uzun for his priceless support as both a trusted friend and a mentor during my academic pursuits. Working with you has been such a privilege. I hope to stay in touch!

Throughout my master's studies, I have been fortunate to receive immense support from my colleagues at Kron Technologies. I am deeply thankful to my directors, Serdal Yıldız and Ekrem Kara, as well as my team leaders, Umut Sezgin and Tunay Akın. Thank you all for your support and understanding made it possible for me to balance both work and my academic studies.

I also want to extend my appreciation to Serdal "abicim" separately. Your presence and support have been invaluable to me, and I am truly grateful to have you by my side. I hope to work together under your guidance for many years to come.

I want to express my heartfelt gratitude to my family for their unwavering support and encouragement throughout my academic journey. I am deeply appreciative of their unconditional love, understanding, and belief in me. I wish to honor my beloved grandmother Yüksel Esen, who passed away during my studies in 2023.

To those who believe in me and accompany me on this adventure

TABLE OF CONTENTS

LIST OF FIGURES

LIST OF ABBREVIATIONS

OAM Orbital Angular Momentum
SPPs Spiral Phase Plates
UCA Uniform Circular Array
EM Electromagnetics
SAM Spin Angular Momentum
CW Clockwise
CCW Counter-Clockwise
Wi-Fi Wireless Fidelity
LG Laguerre-Gaussian
MICs Microwave Integrated Circuits
RF Radio Frequency
WLAN Wireless Local Area Network
CP Circular Polarization
LP Linear Polarization
LHCP Left-Hand Circular Polarization
RHCP Right-Hand Circular Polarization
MSA Microstrip Antenna
HFSS High-Frequency Structure Simulator
SUNUM Sabancı University Nanotechnology Research and Application Center
CoSpace Collaboration Space
P1 Port 1
P2 Port 2
RL Return Loss
IL Insertion Loss
AUT Antenna Under Test

1. INTRODUCTION

Wireless communication technologies are rapidly evolving to meet the increasing demand for higher data rates, more reliable connections, and improved spectral efficiency. Overcoming the limitations of traditional communication systems is becoming immensely significant as the global dependence on wireless networks continues growing. One promising approach to be a prospective solution that requires noteworthy attention is generating Orbital Angular Momentum (OAM) in electromagnetic waves. OAM is a property of electromagnetic fields characterized by a helical phase structure. By enabling multiplexing of multiple data streams at the same frequency, it offers the potential to significantly increase the capacity of wireless communication systems [36].

In the context of antenna design, OAM applications in wireless communications are notably promising. It is possible to benefit from the unique features of OAM modes, such as carrying multiple channels on a single frequency, leading to improved data throughput and enhanced spectral efficiency by integrating OAM concept into antenna systems. For generating and manipulating OAM modes, circular array antennas consisting of multiple radiating elements lined up in a circular arrangement are convenient. Depending on the application, circular array antennas can be designed to operate with either linear or circular polarization, as each offers various advantages.

The literature has investigated a variety of approaches to generate OAM waves, each with distinctive advantages and challenges. In one of the earliest methods, spiral phase plates (SPPs) were used to create a helical phase front by creating a phase shift proportional to the azimuth angle [2]. However, as careful design considerations, such as material selection and manufacturing precision, are required in the applications in the microwave and radio frequency (RF) fields, SPPs have not been widely used as in optical systems.

Utilizing antenna arrays, specifically Uniform Circular Arrays (UCAs), are also used to generate OAM waves by applying a particular phase shift to each array element.

By adjusting the phase distribution throughout the array elements, the OAM mode can be controlled, which makes this method flexible and advantageous in RF applications.

Another approach involves the use of antenna arrays, particularly Uniform Circular Arrays (UCAs), which generate OAM waves by applying a specific phase shift to each element in the array. This method offers flexibility in controlling the OAM mode by adjusting the phase distribution among the elements, making it advantageous in RF applications [45]. Another promising approach is generating vortex electromagnetic (EM) waves by specifically designed antennas or meta-materials. For information encoding, the phase singularity of the wavefront is crucial as in the microwave domain meta-materials allow more compact and efficient OAM wave generation as demonstrated by Tamburini et al. [38]. The use of metamaterials, as explored by Mohammadi et al. [26], allows for more compact and efficient OAM wave generation, especially in the microwave domain.

Another straightforward solution for generating OAM waves is utilizing helical antennas as they can naturally produce a helical phase front [39]. As helical antennas can generate spin angular momentum (SAM) and orbital angular momentum (OAM) simultaneously, they are specifically suitable for applications requiring circular polarization. Mode conversion techniques are also effective in optical and terahertz systems, where precise control over the wavefront is required, by converting conventional waves into OAM waves [44].

In literature, some of these different approaches are followed by researchers to generate OAM. Q. Bai et al. [3] designed a circular array with eight elements to generate OAM mode with mode number $\ell = -1$ at 10 GHz. They located inset fed patches at a radius of 0.6λ and feed the patches using using a feeding network consisting of different microstrip lines which are connected to a single port at the center of the UCA. In another research, Wei et al. [42] focused on designing an UCA operating at 2.5 GHz, which includes four array elements and a circular phase shifter power divider to generate $\ell = 1$ OAM wave. This approach has a simpler feeding network a compact structure where the phase shifter power divider supplies 90° phase difference between patches. X. Bai et al [5] employed another innovative design of a dual circular polarized dual mode OAM generating antenna with four dual circular polarized patches, which enhances the bandwidth. This design allows feeding each patch element with the same phase for clockwise (CW) and counter-clockwise (CCW) circular polarizations. In another study by Huang et al. [16], an antenna consisting four-feed patch and a four-way phase-shifting network is designed to generate $\pm n$ OAM waves in the TM21 mode with mode purity over 90% across a wide band.

This design is suitable for wideband, dual-mode, high-purity OAM beam generation in microwave and millimeter-wave bands.

This thesis focuses on the design, implementation, and analysis of linear and circular polarized circular array antennas for OAM generation at the 6.5 GHz frequency band. The 6.5 GHz band, situated within the microwave spectrum, is of particular interest due to its potential for high capacity wireless communication links and its use in applications such as satellite communications, radar systems, and emerging 5G networks. This band offers advantages such as wider bandwidth and better propagation characteristics compared to lower frequency bands, making it suitable for applications requiring high data rates and reliability. By integrating OAM with circular array antennas at this frequency, this research aims to explore innovative techniques to increase spectral efficiency, increase data transmission rates, and improve overall system performance.

The research involves the development of two distinct circular array antennas, each consisting of four patch elements. The first antenna is designed with linear polarization, while the second is modified to achieve circular polarization by trimming the corners of the patch elements. Both designs are optimized to generate OAM modes, and their performance is evaluated through simulations and experimental measurements.

The comparison of the radiation patterns and phase distributions of the two antennas provides valuable insights into their respective advantages and limitations. By demonstrating the feasibility of generating OAM modes using both linear and circular polarized circular array antennas, this research contributes to the advancement of OAM-based wireless communication systems, particularly in the 6.5 GHz Wi-Fi band. The findings of this thesis lay the groundwork for future developments in high capacity wireless communication systems, where OAM can be leveraged to meet the growing demands of modern communication networks.

This thesis is structured as follows: Chapter 2 provides a comprehensive background on momentum of electromagnetic waves and antennas, specifically polarization, OAM generating circular antenna arrays, laying the groundwork for understanding the theoretical and technical aspects relevant to this research. Chapter 3 discusses the methodology and step-by-step strategies to design circular array antennas with linear and circular polarizations operating at 6.5 GHz. Chapter 4 presents the results and analysis of the measurements, evaluating the performance metrics and validating the proposed methodologies. Chapter 5 summarizes the key conclusions drawn from this research and highlights the contributions to the field of wireless communications, and outlines future research directions.

2. BACKGROUND

This chapter builds the technical infrastructure, laying a foundational understanding of concepts discussed in this thesis. Firstly, the momentum concept in electromagnetics is explained by investigating linear momentum and angular momentum with its sub-components spin angular momentum (SAM) and orbital angular momentum (OAM). Secondly, the general antenna concept is demonstrated by touching upon various antenna design techniques, such as microstrip antennas and antenna arrays.

2.1 Momentum of Electromagnetic Waves

According to Maxwell's theory, electromagnetic radiation is known to transport both energy and momentum [2]. The momentum may consist of two components, which are linear momentum and angular momentum. Angular momentum can be expressed as the rotational analog of linear momentum [13]. Angular momentum can occur in two types, which are spin angular momentum (SAM) and orbital angular momentum (OAM). Electromagnetic beams may carry both of these forms of momenta. The beam possesses SAM if the electric field vector twists around the beam's axis, while it has OAM if the electromagnetic wavefront of the field twists and forms a helical wave vector [8].

2.1.1 Linear Momentum

In electromagnetics, linear momentum **p** is the product of the electromagnetic field's energy density and the velocity of light c in the direction of wave propagation [27], which is defined by:

$$\mathbf{p} = \epsilon_0 \int \mathbf{E} \times \mathbf{B} \, dV \tag{2.1}$$

where $\epsilon_0 \approx 0.85 \times 10^{-12}\,\mathrm{F/m}$ is the permittivity of free space, $\mathbf{E}$ is the electric field vector and $\mathbf{B}$ is the magnetic field vector.

Electromagnetic waves carry energy as described by the Poynting vector as follows:

$$\mathbf{S} = \frac{1}{\mu_0} \mathbf{E} \times \mathbf{B} \tag{2.2}$$

where μ_0 is the permeability of free space. The momentum per unit volume carried by the electromagnetic fields is defined by the momentum density vector:

$$\mathbf{g} = \epsilon_0 \mathbf{E} \times \mathbf{B} \tag{2.3}$$

Conservation of Momentum law asserts that the total momentum of a closed system remains unchanged in the absence of external forces [15]. As Poynting vector and momentum density vector indicates, conservation of linear momentum in electromagnetic wave propagation is ensured.

2.1.2 Angular Momentum

Angular momentum in electromagnetic waves can be divided into two components: spin angular momentum (SAM) and orbital angular momentum (OAM). SAM is associated with the polarization state of the wave (left or right circular polarization), whereas OAM is linked to the spatial distribution of the wave's phase. The difference between SAM and OAM could be explained by an analogy and shown in Figure 2.1. As spinning objects carry SAM, the Earth's rotation around its own axis can be linked to SAM, while the Earth's movement in its orbit around the sun is related to OAM since orbiting objects possess OAM. Electromagnetic beams can carry both SAM and OAM.

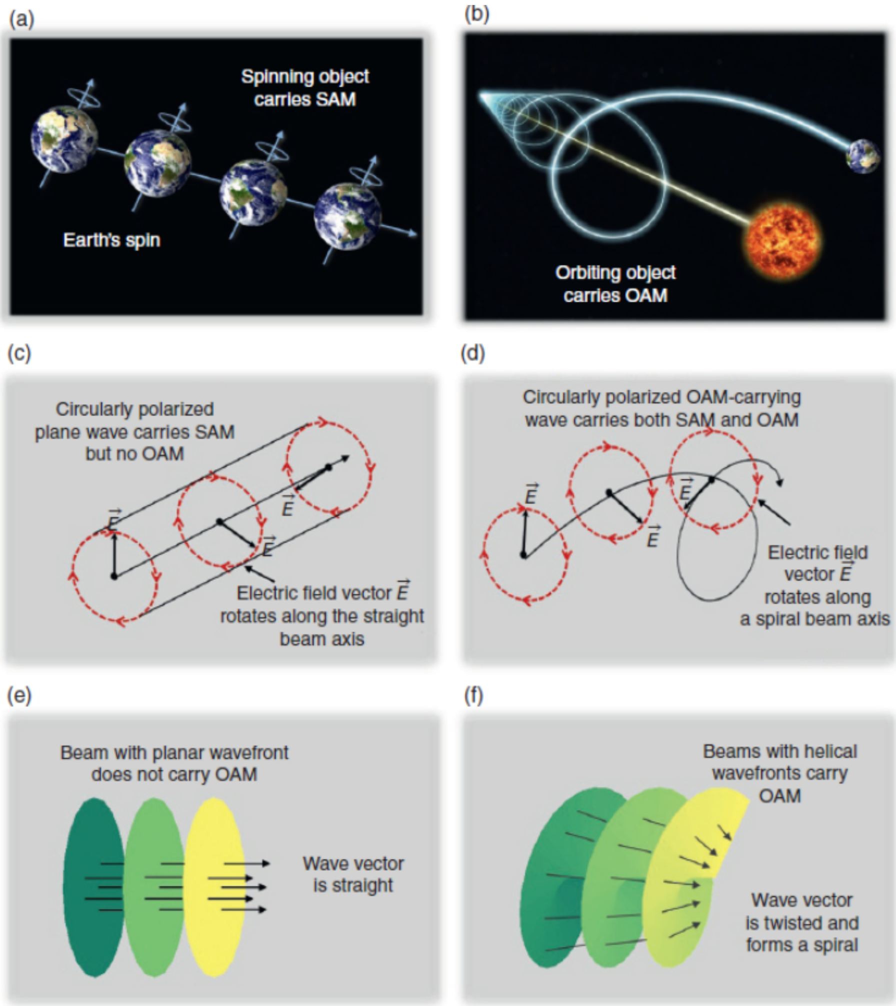

Figure 2.1 Analogy between moving object's and electromagnetic wave's angular momentum

[18]

2.1.2.1 Spin Angular Momentum (SAM)

The foundations of the angular momentum concept has its roots in the early 1900s. In 1909, Poynting [29] theoretically studied SAM of light and put forward the hypothesis that electromagnetic fields can carry angular momentum. After that, Beth [9] verified this statement experimentally in 1936. SAM is called intrinsic angular momentum as it only depends on polarization and does not depend on the axis choice. Letting s be the mode number, s = 0 and corresponds to linearly polarized waves while s = ±1 corresponds to right and left-hand polarized waves [8]. These early studies only considered circularly polarized light beams.

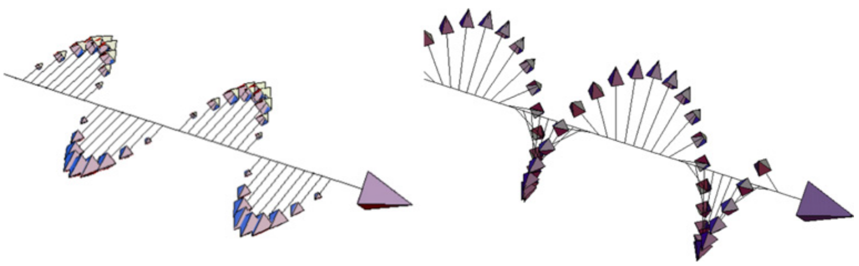

Figure 2.2 Light with linear polarization carries no SAM (left), light with circular polarization carries SAM (right)
[43]

2.1.2.2 Orbital Angular Momentum (OAM)

Orbital angular momentum (OAM) is a property of electromagnetic waves associated with the spatial structure of wave fronts. In recent years, researchers have paid major attention to OAM because of its promising potential for enhancing communication systems. Early studies of OAM are first observed in the context of quantum mechanics. In 1992, Allen et al. [2] showed that light beams with helical phase fronts carry OAM. This discovery drew attention to OAM and pioneered new research in optics and electromagnetics.

OAM is characterized by a helical phase structure of the form $\exp(i\ell\phi)$, where ℓ is the topological charge or the OAM mode number, and ϕ is the azimuthal angle. The integer ℓ determines the number of twists in the phase front per wavelength. Beams carrying OAM are often described by Laguerre-Gaussian modes in cylindrical coordinates.

(2.4)

$$\psi_{\ell,p}(r,\phi,z)=C\cdot\left(\frac{r}{w(z)}\right)^{|\ell|}\exp\left(-\frac{r^2}{w^2(z)}\right)L_p^{|\ell|}\left(\frac{2r^2}{w^2(z)}\right)\exp\left(i(2p+|\ell|+1)\zeta(z)\right)\exp(i\ell\phi)$$

where:

- $L_p^{|\ell|}$ are the generalized Laguerre polynomials,
- $w(z)$ is the beam waist,
- $\zeta(z)$ is the Gouy phase,
- C is a normalization constant.

Orbital Angular Momentum (OAM) waves are generated through distinct methodologies in optical and radio frequency domains. In optics, methods such as Spiral Phase Plates (SPPs) and diffraction gratings are employed to manipulate phase fronts of light beams, imparting OAM characteristics [10]. SPPs use varying thicknesses to induce phase shifts, transforming Gaussian beams into OAM-carrying beams, while diffraction gratings create interference patterns to encode OAM states [23, 39].

In radio frequencies, the adaptation of optical principles extends to cover larger wavelengths and lower frequencies. In order to generate OAM, the phase of radio waves is altered using various techniques such as plane wave transformers, including modified SPPs and flat phase plates [7, 17]. Additionally, circular phased arrays are utilized to manipulate phase shifts across antenna elements to effectively produce OAM waves, which are widely used for radar and satellite communication applications [39]. These approaches exhibit diverse applications and technological implications of OAM across different frequency bands and demonstrate promising results, making it a popular research topic among researchers.

OAM communication has been effectively applied in several advanced technological areas. As an instance, it is used in free-space optical communications to multiplex data streams, reaching terabit-level data transmission rates [1]. In the wireless networks area, OAM has a pivotal role in the development of 6G technology due to its spectral efficiency and data throughput [11]. Furthermore, OAM has been integrated into air-to-ground communication systems for drones, which significantly improves bandwidth efficiency and communication reliability [14].

2.2 Antennas

An antenna is a transducer that converts guided electromagnetic waves to radiated waves in free space or vice versa and is characterized by its radiation pattern, directivity, gain, efficiency, polarization, and bandwidth [6]. It serves as the interface between guided waves and free-space waves, whereas its dimensions are typically related to the operating wavelength, and its performance is governed by the principle of reciprocity [19].

Antennas operate based on fundamental principles of electromagnetics, where electric currents in conductors generate electromagnetic fields that radiate outward into space. The performance characteristics of an antenna is determined by the size and shape of the antenna, along with its design parameters such as frequency, impedance, and radiation pattern [30].

Antennas play a vital role in various applications, including wireless communication, radar systems, satellite communication, and broadcasting. They are designed to radiate or receive electromagnetic waves within explicit frequency bands to satisfy the requirements of different communication standards in diverse environmental conditions [12].

2.2.1 Microstrip Antennas (MSA)

Microstrip antennas have a great impact in modern antenna design because of their compact size, low profile structure, and compatibility with microwave integrated circuits (MICs) [35]. This section provides an overview of various microstrip antenna types, theoretical background, design considerations, and antenna arrays, specifically uniform circular array (UCA).

2.2.1.1 Rectangular Patch

Microstrip patch antennas are a popular choice for various wireless communication applications due to their low profile, lightweight, and ease of integration with printed circuit boards [20]. They consist of a dielectric substrate with a radiating patch on one side and a ground plane on the other [34]. These antennas operate based on the principle of microstrip transmission line theory, where the patch acts as a resonant element and the substrate as a dielectric medium. The antenna's operating frequency, impedance matching, bandwidth, and radiation characteristics are determined by dimensions of the patch, substrate material properties, and feeding mechanism [30].

Due to their compact size and directional radiation patterns, these antennas are extensively used in satellite communication systems, mobile devices, radar systems, and wireless local area networks (WLANs). In order to achieve desired specifications and improve antenna performance, advanced design techniques such as parasitic elements, stacked patches, and aperture-coupling are employed [12].

A rectangular patch antenna can be designed once the material properties of the substrate, such as the dielectric constant (ϵ_r) and height (h), are determined.

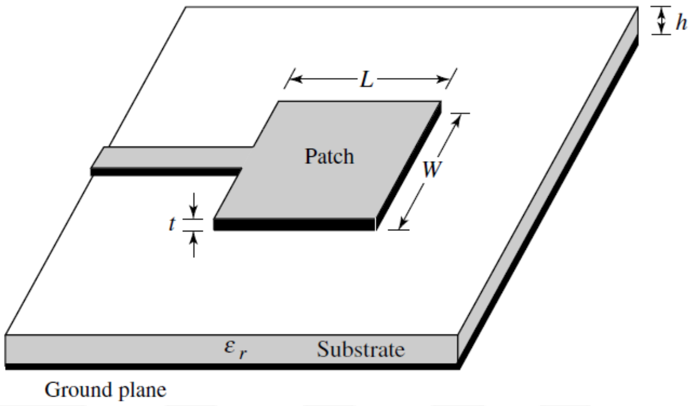

Figure 2.3 Rectangular microstrip antenna with design parameters [6]

Specifying the material properties of chosen substrate and resonant frequency (f_r), W and L parameters can be calculated by (2.5) - (2.8).

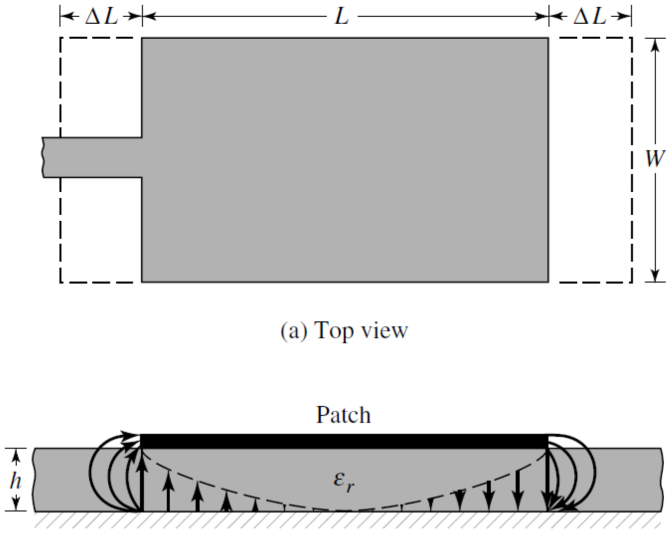

(a) Top view

(b) Side view

Figure 2.4 Rectangular patch antenna with physical and effective lengths [6] for $\frac{W}{h} > 1$,

$$\epsilon_{reff} = \frac{\epsilon_r + 1}{2} + \frac{\epsilon_r - 1}{2}[1 + 12\frac{h}{W}]^{-\frac{1}{2}} \tag{2.5}$$

$$W = \frac{1}{2f_r\sqrt{\mu_0\epsilon_0}} + \sqrt{\frac{2}{\epsilon_r + 1}} \tag{2.6}$$

$$\frac{\Delta L}{h} = 0.412\frac{(\epsilon_{reff} + 0.3)(\frac{W}{h} + 0.264)}{(\epsilon_{reff} - 0.258)(\frac{W}{h} + 0.8)} \tag{2.7}$$

$$L = \frac{1}{2f_r\sqrt{\epsilon_{reff}}\sqrt{\mu_0\epsilon_0}} - 2\Delta L \tag{2.8}$$

The far-field components for a rectangular microstrip patch antenna with z-axis normal can be calculated by (2.9) - (2.11) [37] where $\beta = \frac{2\pi}{\lambda}$ is the propagation constant.

$$E_\theta = E_0 \cos\phi f(\theta,\phi) \tag{2.9}$$

$$E_\phi = -E_0 \cos\theta \sin\phi f(\theta,\phi) \tag{2.10}$$

$$f(\theta,\phi) = \frac{\sin[\frac{\beta W}{2}\sin\theta\sin\phi]}{\frac{\beta W}{2}\sin\theta\sin\phi}\cos(\frac{\beta L}{2}\sin\theta\sin\phi) \tag{2.11}$$

2.2.1.2 Circular Polarization

When the patches that are reviewed in previous sections, which are rectangular and circular patch, are used with no modifications in typical feeding structure or patch integrity, they radiate primarily waves with linear polarization. Nevertheless, by making slight changes in the feed arrangements and patch geometry, circular or elliptical polarization can be achieved [6].

Circular polarization (CP) can be created by exciting two out of phase orthogonal modes. For this purpose, different approaches can be followed such as using single feed or multiple feeds and adjusting physical properties of the patch. The first approach is feeding a square patch from two points on orthogonal edges, where ports are excited with equal amplitude and 90° time-phase difference. Here, leading or lagging phase determines if the radiation is left-hand circularly polarized (LHCP) or right-hand circularly polarized (RHCP). Another approach is making slight perturbations in the symmetric structure of conventional single feed patches, which generate orthogonal modes of equal amplitude and quadrature phase internally. In practice, slightly modified square or circular patches are popular, even though various different shaped patches are capable of generating circular polarization [37].

In Figure 2.5(a), a nearly square patch of slightly differing sides of L by L+δL is modelled as two orthogonal dipoles, which leads to marginal length differences to half-wave resonant. As a consequence of proper length difference, the radiated fields are expected to be 90° out of phase. In (b) and (c) of the same figure, different shapes are designed by modifying conventional square patches such as inserting a slot into the square patch and trimming the corners respectively. While previous patches are edge fed, the patch in Figure 2.5(d) is created by positioning the feed point off-center of the radiating edge and probe-fed, which is widely preferred because of its compact feed beneath the patch [37].

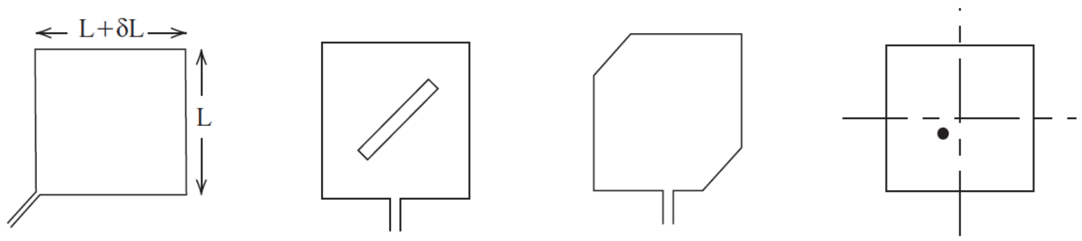

(*a*) Nearly square corner-fed patch.

(*b*) Slotted square patch.

(*c*) Corner trimmed square patch.

(*d*) Offset probe-fed square patch.

Figure 2.5 Single feed rectangular microstrip patches to generate circular polarization
[37]

In Figure 2.6(a) and (b), circular polarization is obtained by feeding the patch from two adjacent edges, thus exciting two orthogonal modes: TM^x_{010} and TM^x_{001}. By feeding the patch with a 90° hybrid or 90° power divider. In a circular patch, feeding the patch with two angular separated feeds leads to circular polarization for TM^z_{110} mode. In the design shown in Figure 2.6(c), in order to generate orthogonal fields to each other, two coax feeds are separated by 90°. This two probe arrangement also ensures that mutual coupling between two probes is minimized. Additionally, a 90° hybrid is utilized to have a 90° phase difference between the fields of two feeds [6].

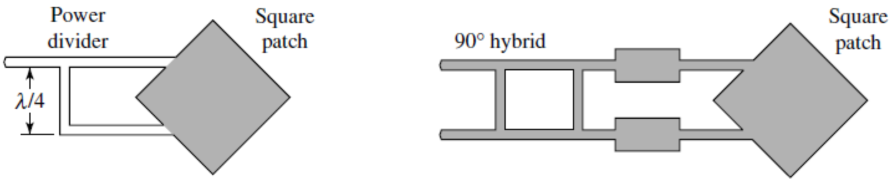

(a) Square patch driven at adjacent sides through a power divider

(b) Square patch driven at adjacent sides through a 90° hybrid

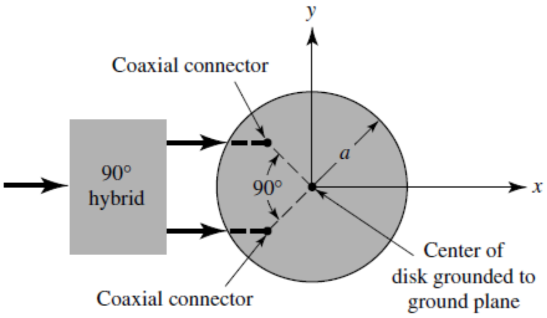

(c) Circular patch fed with coax

Figure 2.6 Various rectangular and circular patch designs for circular polarization [6]

2.2.2 Antenna Arrays

Antenna arrays contain multiple antenna elements arranged in specific configurations to achieve desired radiation patterns and performance characteristics [30]. These antennas are essential in modern wireless communication systems, offering advantages such as increased gain, improved spatial coverage, and adaptive beamforming capabilities.

Antenna arrays can be categorized into various types, such as linear arrays, planar arrays, and conformal arrays, based on their layout, where each type serves different purposes. While linear arrays are suitable for scanning beams in a particular direction, planar arrays provide sectorized coverage in cellular networks, and conformal arrays comply with curved surfaces such as aircraft or vehicles [12].

Adjusting the spacing, amplitude, and phase of individual antenna elements, desired antenna design requirements, and specific performance metrics, such as radiation patterns, can be achieved in the design and optimization step of the antenna array. Advanced techniques such as digital beamforming and phased antenna arrays further improve the versatility and efficiency of antenna arrays in diverse applications.

2.2.2.1 Uniform Circular Array (UCA)

A uniform circular array (UCA) is a specific subcategory of antenna arrays where antenna elements are spaced equidistant and arranged circularly around a center point. This structure offers benefits in diverse applications thanks to its unique radiation pattern characteristics and operational effectiveness. UCAs can achieve highly directive radiation patterns with minimized side lobes and enhanced main lobe. Thus, they are opted for applications requiring precise beamforming and spatial coverage [6].

The circular geometry of UCAs inherently supports polarization diversity, enabling simultaneous reception or transmission of signals with different polarization states. This feature is beneficial in mitigating signal fading and enhancing communication reliability in diverse propagation environments [24]. Practical implementations of UCAs involve optimizing parameters such as element spacing and number of elements, tailored to specific operational frequencies and application requirements. Advanced signal processing techniques, including adaptive beamforming and interference mitigation strategies, further enhance the performance of UCAs in complex radio frequency scenarios [41].

UCAs represent a robust antenna design that combines directional beamforming capabilities with polarization diversity, making them well-suited for modern communication systems, radar applications, and wireless networks where efficient spectrum utilization and reliable signal reception are outstanding [37].

2.2.2.2 OAM Generating Uniform Circular Array (UCA) Antenna

Uniform Circular Array (UCA) antennas, with their elements arranged evenly along a circle, excel at generating OAM modes. In this methodology, the phase difference between the first and the last element of the circular array is $2\pi\ell$. For an N element UCA, the phase difference of two consecutive elements is:

$$\delta\varphi = \frac{2\pi\ell}{N} \tag{2.12}$$

where ℓ is the mode number. Besides, it is notable that the number of OAM modes can be generated by a UCA with N elements conforms to the inequality:

$$-\frac{N}{2} < \ell < \frac{N}{2} \tag{2.13}$$

In order to generate two OAM modes with mode numbers $\ell = \pm 1$, the minimum number of array elements must be 4 and the phase step between each element is $\delta\varphi = \frac{2\pi\ell}{N} = \pi/2$ radians $= 90^\circ$. The proposed design consists of evenly spaced 4 array elements with an equal distribution of the signal power among the elements [40].

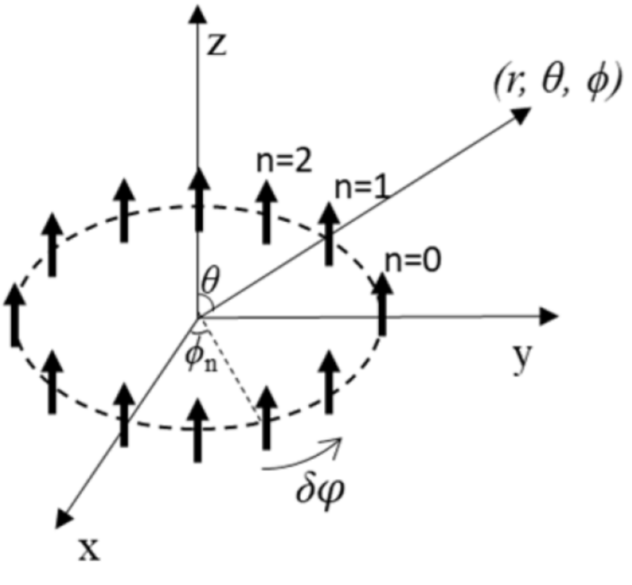

Figure 2.7 An illuastration of UCA

[21]

An illustration of UCA can be found in Figure 2.7. The electric field vector $\mathbf{E}$(r,θ,φ) at a point (r,θ,φ) where an OAM antenna composed of dipoles in a circular arrangement is emitting radiation is described by Equation 2.14.

$$\mathbf{E}(r,\theta,\phi) = -\mathbf{j}\frac{\mu_0 \omega d}{4\pi}\frac{e^{ikr}}{r}\sum_{n=0}^{N-1} e^{-i(\mathbf{k}\cdot\mathbf{r}_n - \ell\varphi_n)} \tag{2.14}$$

$$\approx \mathbf{j}\frac{\mu_0 \omega d}{4\pi}\frac{e^{ikr}}{r} N_i e^{i\ell\varphi} J_\ell(k\alpha \sin\theta) \tag{2.15}$$

In Equation 2.14, $\mathbf{j}$, φn, α, J_l, μ_0, d and k indicate constant current density, $\frac{2\pi n}{N}$, antenna radius, ℓ-order Bessel function, magnetic conductivity, dipole length and wave number respectively. Here, nth array element has phase of $\phi_n = l\varphi_n = \frac{2\pi l n}{N}$. In this equation, $\sum_{n=0}^{N-1} e^{-i(\mathbf{k}\cdot\mathbf{r}_n - \ell\varphi_n)}$ is the array factor and if N is large enough, it corresponds to $N_i e^{i\ell\varphi} J_\ell(k\alpha \sin\theta)$. In Expression 2.15, $e^{i\ell\varphi}$ demonstrates the relation between azimuth angle ϕ and vector potential.

3. ANTENNA DESIGN

In this chapter, the strategies followed during the final UCA antenna generating OAM waves with linear and circular polarizations were demonstrated step by step. First, the design details of the building block of UCA, which are patch antennas, were discussed, and HFSS (3D High-Frequency Structure Simulator) simulation results were investigated. Then, these patches were located around a circular array, and the design choices made during the process were discussed along with their simulation outcomes. Lastly, the final design obtained by joining patches with transmission lines was analyzed with simulation data.

3.1 Microstrip (Patch) Antenna Design

Patch antennas are a critical component of the system, and their design directly impacts the performance and efficiency of the generated OAM modes. Two separate patch antennas were designed to demonstrate the differences between OAM antennas with circular and linear polarization: one with linear polarization and the other with circular polarization. This section presents the design details and simulation results of the patch antennas used in the 6.5 GHz OAM antenna array.

3.1.1 Linearly Polarized Patch Antenna Design

Each linearly polarized patch antenna in the array is designed with a square geometry, measuring 11.5 mm x 11.5 mm. The substrate material selected for the design is Rogers Corporation RO4003C, which has a dielectric constant (ϵ_r) of 3.55, a loss tangent ($\tan\sigma$) of 0.0027, and a thickness of 0.813 mm [32]. The choice of this substrate was based on its excellent high-frequency performance and low-loss characteristics, making it ideal for the 6.5 GHz application.

The design process involved calculating the resonant frequency and dimensions of the patch antenna to ensure optimal performance at 6.5 GHz. The patch antenna was modeled and simulated using HFSS (High-Frequency Structure Simulator) to evaluate its performance characteristics, including return loss and radiation pattern.

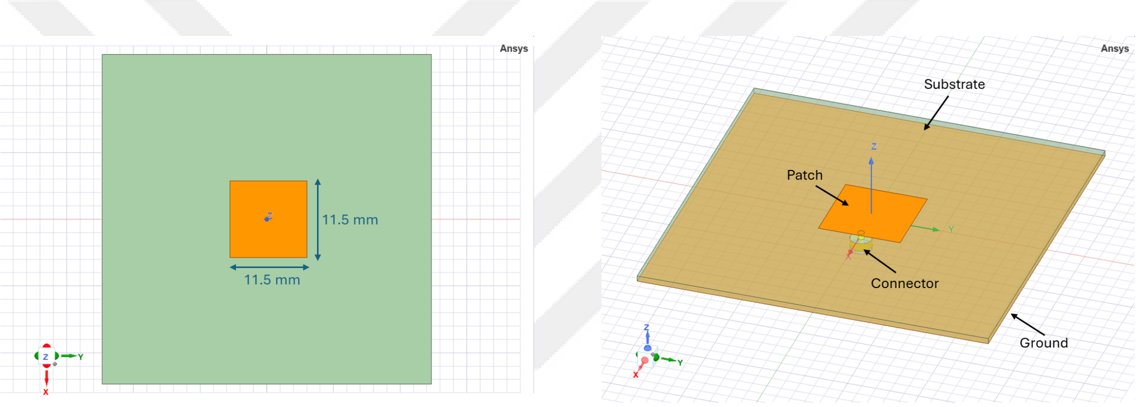

(a) Front view

(b) Structure

Figure 3.1 Designed patch antenna for linear polarization

The return loss (S11) is a critical measure of how well the antenna is matched to the transmission line. A lower return loss indicates better impedance matching, leading to more efficient radiation and minimal reflection. The return loss vs. frequency graph for the linearly polarized patch antenna design is shown in Figure 3.2. The graph indicates the antenna is well-matched at the 6.5 GHz frequency band, with a return loss of less than -6 dB across the desired frequency range.

During the design process, parametric sweep is utilized to achieve the best patch side lengths that conform to desired performance metrics such as return loss and gain at specified frequency bands. Better return loss values are obtained for different patch side lengths of a single patch antenna than the one presented in Figure 3.2. However, in order to preserve impedance matching (to minimize signal reflection and maximize power transfer) with transmission lines and phase difference, patch side lengths with worse but acceptable return loss results are preferred for a single patch to have better overall UCA antenna performance.

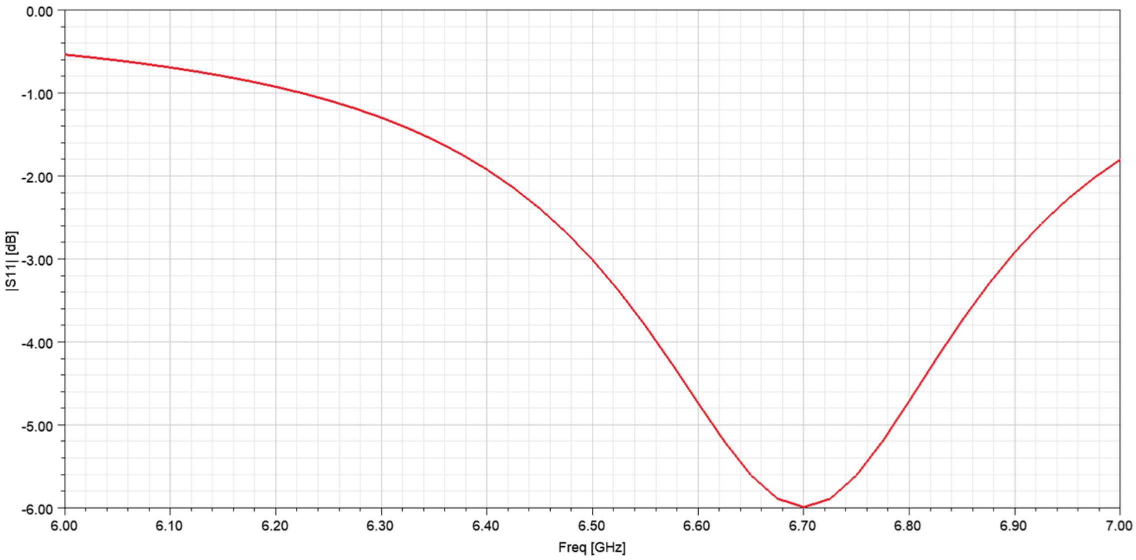

Figure 3.2 Return loss vs. frequency plot of linearly polarized patch antenna

The 3D radiation pattern provides a comprehensive view of the antenna's radiation characteristics in all directions. It is essential for understanding the directivity and gain of the antenna. The simulation results for the 3D radiation pattern of the linearly polarized patch antenna at 6.5 GHz are illustrated in Figure 3.3. The radiation pattern shows a directional main lobe with a realized gain of 4.2 dBi, confirming that the antenna efficiently radiates energy in the desired direction.

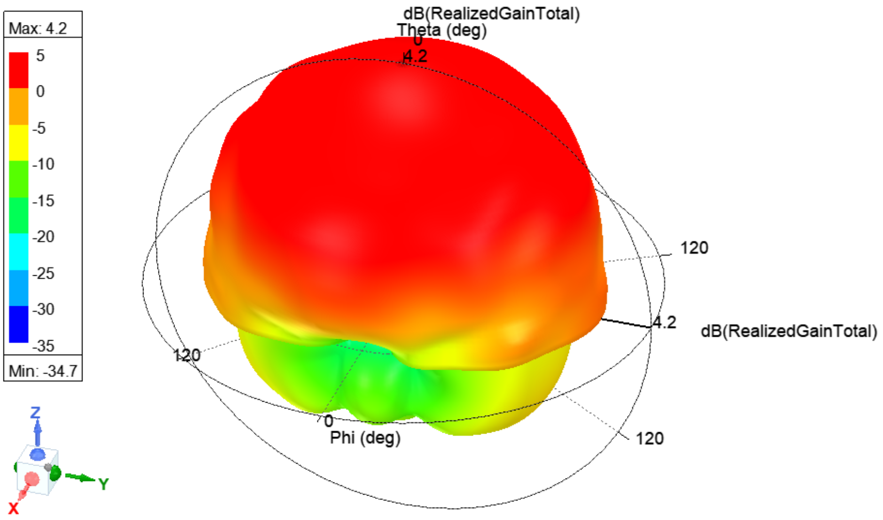

Figure 3.3 Simulated 3D radiation pattern of linearly polarized patch antenna

3.1.2 Circularly Polarized Patch Antenna Design

The design of the linearly polarized patch antenna was modified by trimming patch corners to achieve circular polarization. This technique introduces two orthogonal modes with a 90° phase difference, resulting in circular polarization. The corners were trimmed to a depth of 1 mm, causing a perturbation that splits the degenerate modes, leading to circular polarization. The modified patch antenna was then modeled and simulated using HFSS to evaluate its performance.

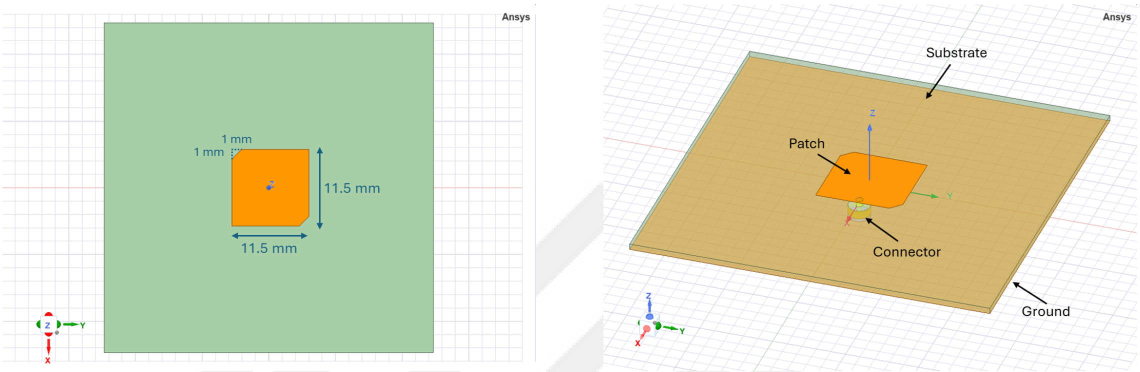

(a) Front view (b) Structure

Figure 3.4 Designed patch antenna with circular polarization

Similar to the linearly polarized patch antenna, the return loss of the circularly polarized patch antenna is a crucial parameter. Figure 3.5 shows the return loss vs. frequency graph for the circularly polarized patch antenna design. The graph indicates that the antenna is well-matched at the 6.5 GHz frequency, with a return loss of less than -10 dB across the desired frequency range.

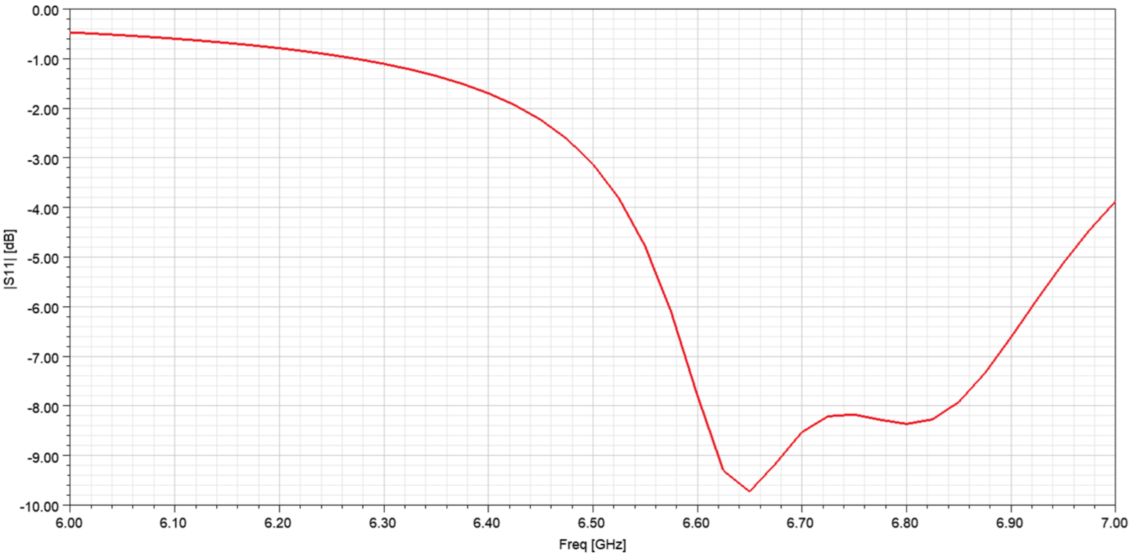

Figure 3.5 Return loss vs. frequency plot of circularly polarized patch antenna

The 3D radiation pattern of the circularly polarized patch antenna provides insight into its radiation characteristics and polarization purity. The simulation results for the 3D radiation pattern at 6.5 GHz are illustrated in Figure 3.6. The pattern demonstrates a directional main lobe with a realized gain of 4.4 dBic, confirming the effectiveness of the corner trimming technique in achieving circular polarization.

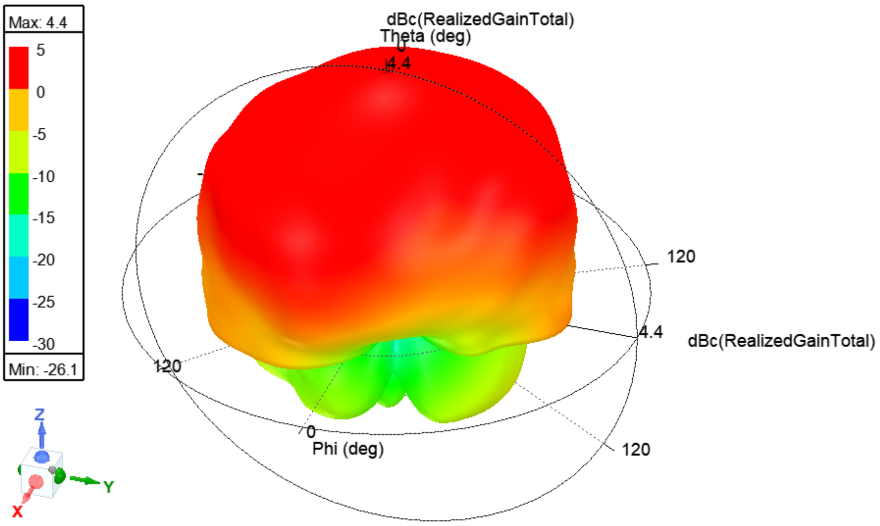

Figure 3.6 Simulated 3D radiation pattern of circularly polarized patch antenna

These simulation results demonstrate that the linearly and circularly polarized patch antennas meet the required specifications and can be used as array elements in a uniform circular array to generate OAM at the 6.5 GHz Wi-Fi band. The return loss indicates efficient impedance matching, while the 3D radiation patterns confirm effective radiation characteristics. The conversion from linear to circular polarization through corner trimming is efficient as the main lobe gain is higher and return loss is lower in circularly polarized patch antenna.

In the following sections, these patch antennas will be integrated into a uniform circular antenna array, and the performance analysis of the complete system will be discussed.

3.2 Patch Antenna Array

In their 8-element phased patch array design operating at 10 GHz frequency, Q. Bai et al. [4] present E-plane radiation patterns for 0.5λ and 0.7λ radius values for OAM modes with $l = 0$ and $l = 1$, which can be found in Figure 3.7. For OAM mode with mode number $l = 0$, the UCA radiates in the axis of maximum gain, which is the boresight direction. Moreover, it is clearly observed in Figure 3.7(a) that as the array radius increases, the main lobe beamwidth diminishes while the side lobe radiation increases. For OAM mode with mode number $l = 1$ as in Figure 3.7(b), as the opposite pair of patch elements are out of phase a null (singularity) occurs at boresight. Considering these, different radius values such as $\frac{\lambda}{4}$, $\frac{\lambda}{2}$, $\frac{3\lambda}{4}$ and λ are set, and their effects are observed in the HFSS simulation. Eventually, $\frac{\lambda}{2}$ is determined to be the optimal radius value. The main lobe beam width is the widest, and the transmission lines connecting single patches are not too long; therefore, the losses are the lowest.

After designing the patch antennas with linear and circular polarization, four of these antennas were placed in a uniform circular array with a radius of $\lambda = 12.45$ mm, which is nearly half wavelength ($\lambda = 12.25$ mm) by utilizing Optimetrics (Parametrics and Optimization) tool of HFSS. The phase difference between the patches was calculated to be 90°. This phase difference is crucial because maintaining a constant phase difference between adjacent elements in a uniform circular array ensures constructive interference in the desired direction. Figure 3.8 shows a sketch representing the patch antenna array. With $N = 4$ patch antennas, the phase step between each element should be $\Delta\phi = \frac{360°}{N} = 90°$. This phase step ensures the array generates two orthogonal OAM modes with $l = \pm 1$.

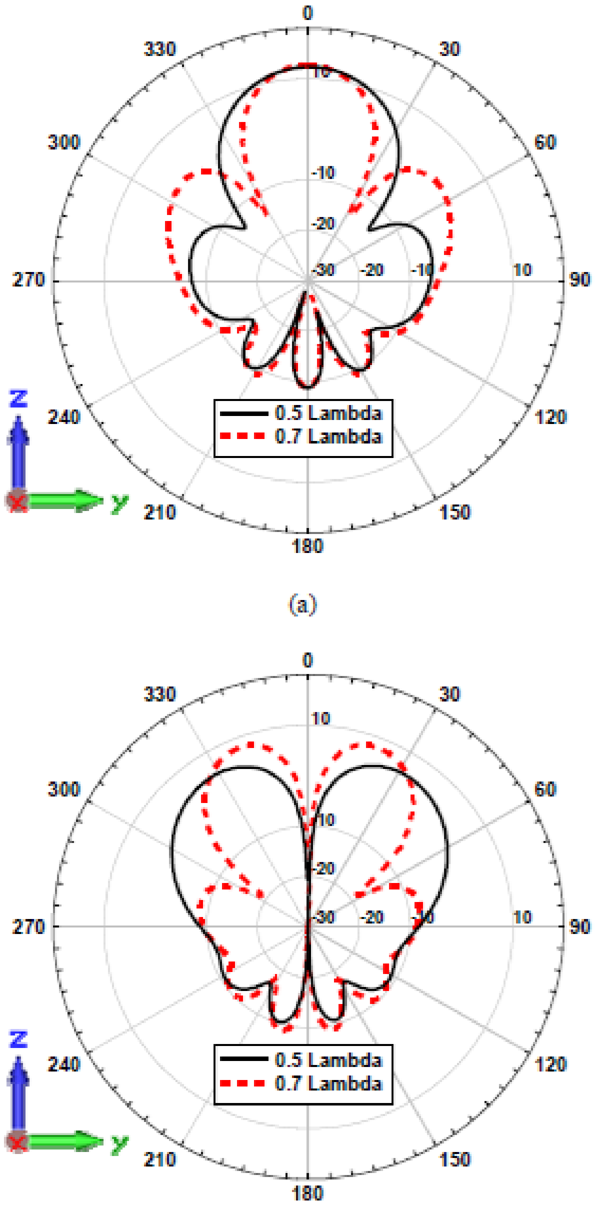

(a)

(b)

Figure 3.7 Radiation patterns of circular array with 0.5λ and 0.7λ radius working at OAM mode number (a) $\ell = 0$, (b) $\ell = 1$
[4]

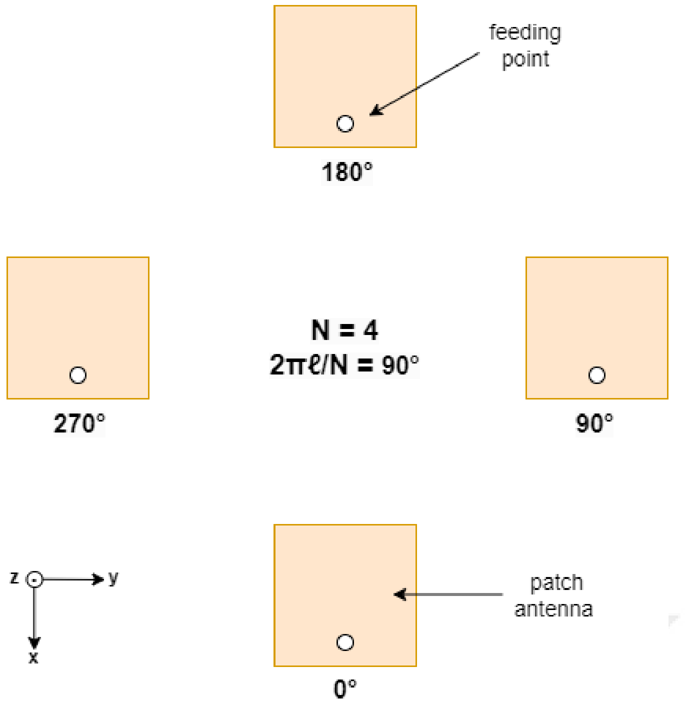

Figure 3.8 Structure of the phased patch antenna array

The observation plane for the phase pattern is positioned 210 mm away from the antenna surface to accurately observe the phase pattern as shown in Figure 3.9. This setup allows for clear visualization of the 2π phase variation in one complete turn and the null at the center of the magnitude pattern, confirming the generation of OAM waves with $l = \pm 1$.

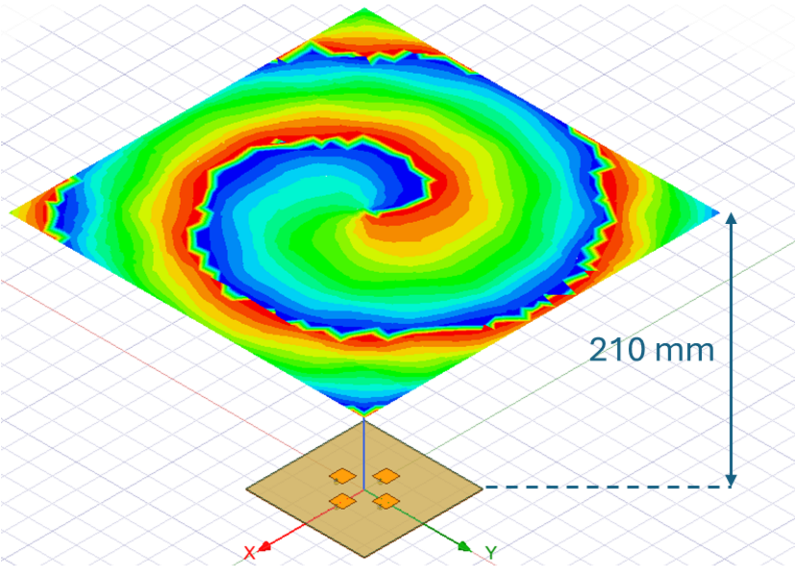

Figure 3.9 Observation Plane

3.2.1 Patch Antenna Array with Linear Polarization

The 3D radiation pattern, 2D radiation patterns with $\phi = 0°$ and $\phi = 90°$ slices, and the E_x and E_y phase patterns were obtained for both polarization cases. Figure 3.11 exhibits 3D radiation pattern of linearly polarized antenna array consisting of 4 patch elements. Null point (singularity) are seen at the center of radiation pattern in this figure. The radiation occurs mainly in the desired direction with maximum 3.3 dBi gain. In Figure 3.12, slices that are taken from $\phi = 0°$ and $\phi = 90°$ shown. Singularities are more clearly observed in these patterns at the same place, at $\theta = 0°$.

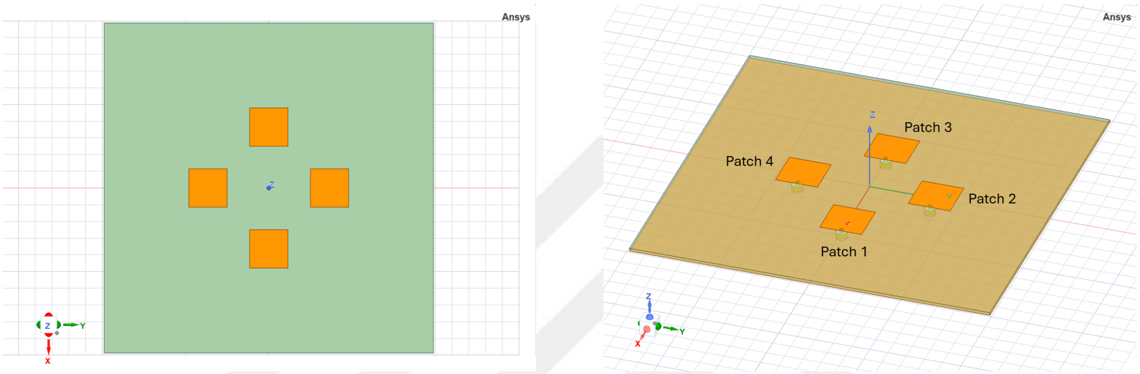

(a) Top view (b) Structure

Figure 3.10 Structure of the phased patch antenna array with linear polarization

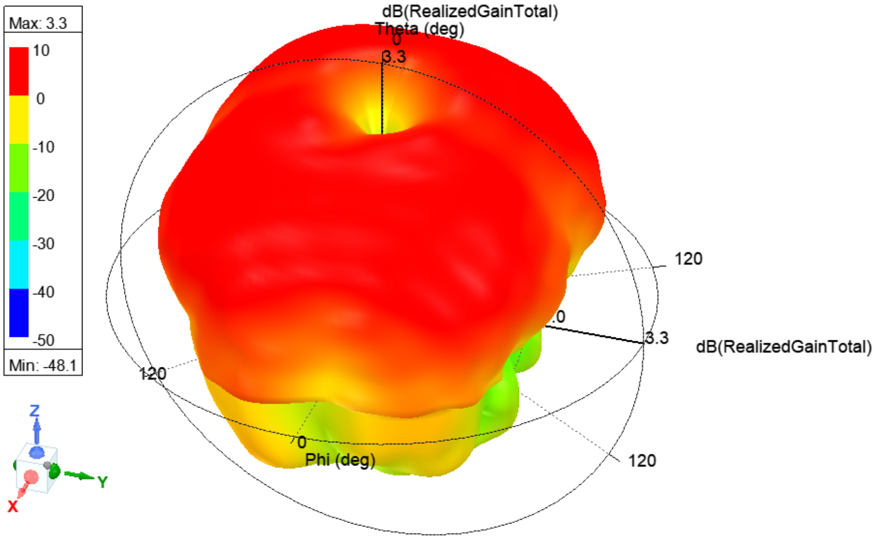

Figure 3.11 3D radiation pattern of the linearly polarized patch array

Phase patterns for two poles, which are E_x and E_y, are presented in Figure 3.13. A rotation in the CCW direction for the E_x phase was observed for the linear polarization case. Nevertheless, no rotation is observed for the E_y phase. The observed rotation in the E_x phase but not in the E_y phase for the linear polarization case is likely due to the nature of linear polarization, where the electric field oscillates primarily in a single plane (in this case, along the x-axis). The antenna array is designed to manipulate the phase of the E_x component, resulting in a CCW rotation. However, since the E_y component is not the primary direction of polarization, it remains mainly unaffected and exhibits no significant rotation. This behavior reflects the inherent characteristics of linear polarization and the specific design of the antenna array.

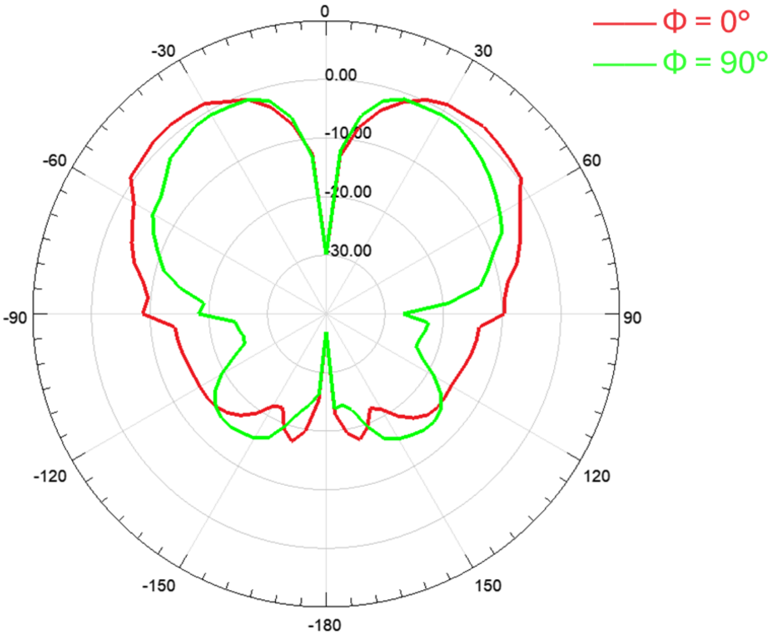

Figure 3.12 2D radiation pattern of the linearly polarized patch antenna array

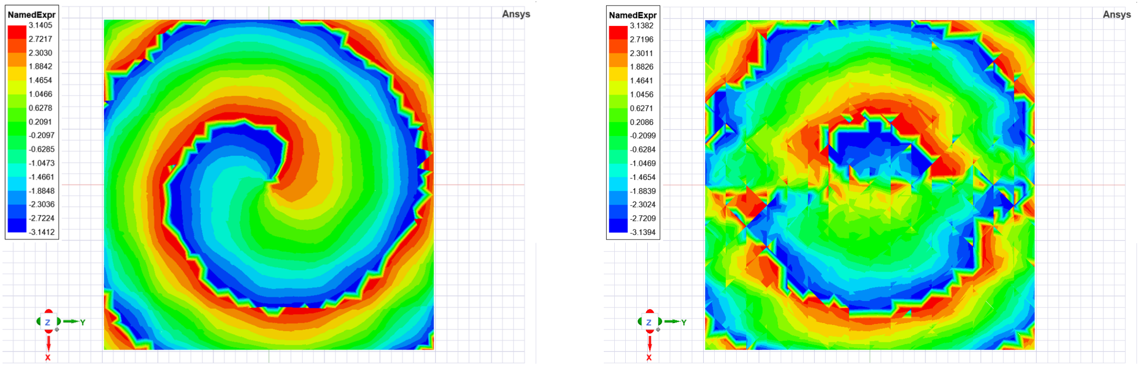

(a) E_x phase

(b) E_y phase

Figure 3.13 Phase patterns of the patch antenna array with linear polarization

3.2.2 Patch Antenna Array with Circular Polarization

For the circularly polarized patch antenna array, the overall patch alignment and antenna structure can be seen in 3.14. 3D radiation pattern in Figure 3.15 and 2D radiation patterns consisting of slices taken from $\phi = 0°$ and $\phi = 90°$ in Figure 3.15 demonstrate that a singularity occurs at the same place, which is at the center of the pattern. In this case, the maximum realized gain is calculated as 5.1 dBic, which reveals a better radiation performance than the linearly polarized patch antenna array.

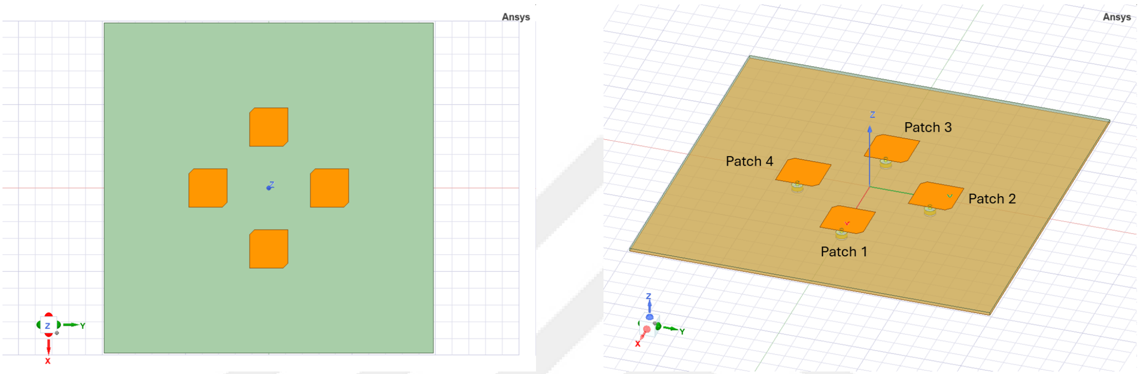

(a) Top view (b) Structure

Figure 3.14 Structure of the patch antenna array with circular polarization

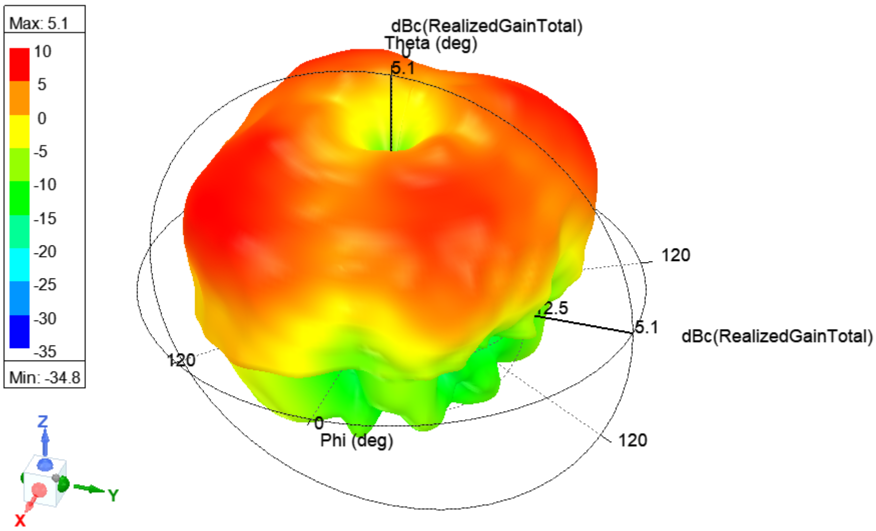

Figure 3.15 3D radiation pattern of the patch antenna array with circular polarization

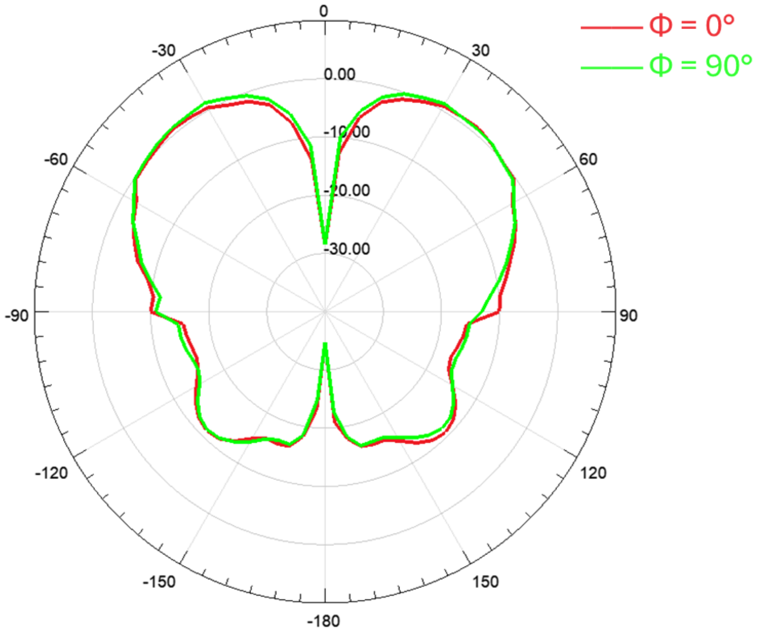

Figure 3.16 2D radiation pattern of the patch antenna array with circular polarization

Figure 3.17 presents E_x and E_y phase patterns for the circularly polarized patch antenna. The directions of the E_x and E_y phase patterns appear in the same direction. This happens as circular polarization inherently involves a 90° phase shift between the orthogonal components (E_x and E_y) of the electric field within each patch antenna. When the patch antennas are placed in a circular array with an additional 90° phase shift between adjacent patches, the phase shifts align in such a way that the E_x and E_y components rotate synchronously in the same direction. This synchronization of phase rotation is an indication of circular polarization, ensuring that the resultant electromagnetic wave maintains a consistent circular polarization state throughout the radiation pattern.

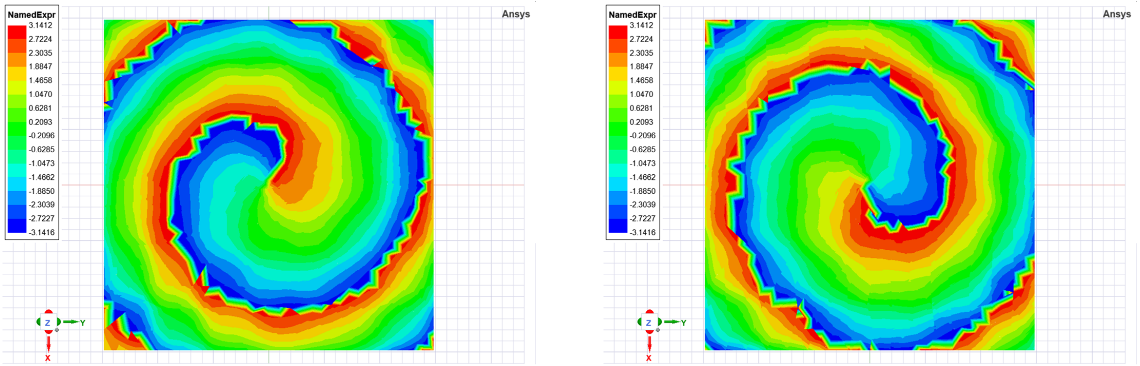

(a) E_x phase

(b) E_y phase

Figure 3.17 Phase patterns of the patch antenna array with circular polarization

In circular polarization, both the E_x and E_y components are involved, with equal amplitude and a 90° phase difference between them, creating a rotating electric field vector. This results in both E_x and E_y phase components exhibiting rotation, typically in the same direction. For example, in left-hand circular polarization (LHCP), the electric field vector rotates in a counter-clockwise direction when looking in the direction of propagation, meaning both E_x and E_y phases rotate synchronously.

Comparatively, in linear polarization, only one component (e.g., E_x) is primarily active, leading to a situation where only that component's phase rotates, as observed in the linear polarization case. The E_y component, being minimal or zero, shows no rotation. Thus, the key difference between linear and circular polarization lies in the involvement and behavior of both components: circular polarization results in synchronized rotation of both E_x and E_y phases, while linear polarization affects primarily one component, leaving the other unaffected.

3.3 OAM Antenna Design

As the final step, the patches in the circular array were connected with microstrip lines to create a two-port system, ensuring that the phase differences between patches are maintained. The patches were connected to each other using two different type of microstrip lines. In this chapter, first the step-by-step design process of these microstrip lines are examined. For each type of transmission lines, the design choices are discussed in detail and the simulation results such as return loss, insertion loss and phase for sub-segments are shown.

Then, the sub-segments are merged to realize the overall UCA antenna. The 3D radiation pattern, 2D radiation patterns with $\phi = 0°$ and $\phi = 90°$ slices, and the E_x and E_y phase patterns were obtained for both polarization cases. Different from previous observations, phase patterns were obtained by exciting port 1 (P1) and port 2 (P2) separately. For both linear and circular polarization, the direction of rotations in phase patterns was observed to be in reverse order for different port excitations.

3.3.1 Design of Microstrip Lines

This section investigates the design tricks behind the transmission lines that connect patches, and the lengths of microstrip lines with different types are determined. Two different transmission lines are used in the UCA, named Γ-line and s-line, due to their shape similarities to these letters and shown in Figure 3.18.

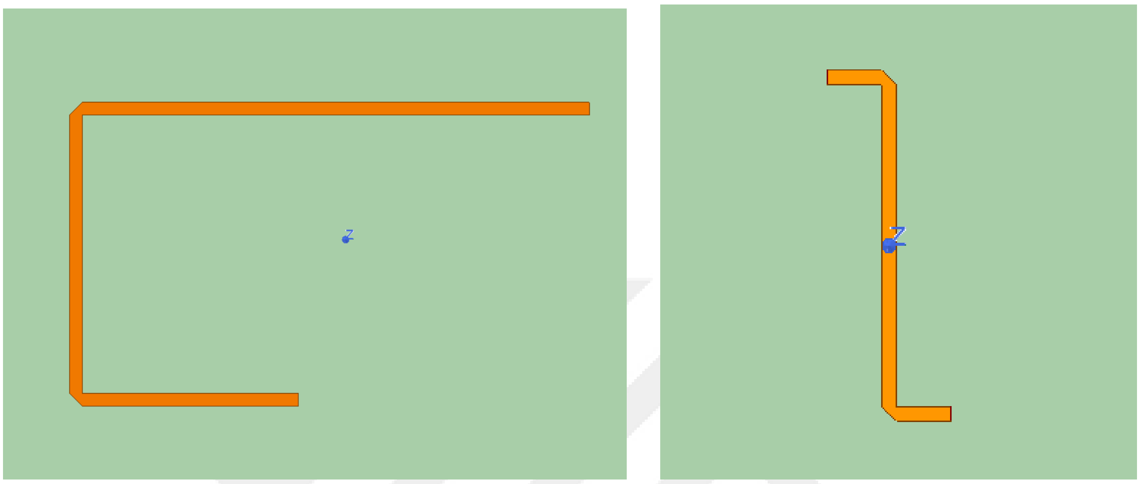

(a) Γ-line (b) S-line

Figure 3.18 Designed microstrip lines

In order to maintain the 90° phase differences between patches and fit to the radius of UCA, these two transmission lines need to have different lengths, which can be expressed as:

$$\begin{cases} m\lambda + \frac{\lambda}{4}, & \text{for s-line} \\ n\lambda + \frac{3\lambda}{4}, & \text{for } \Gamma\text{-line} \end{cases}$$

where m and n are integers.

After performing calculations, simulation, and optimizations to achieve desired phase differences between patches, the s-line and Γ-line lengths were designated as 24.9 mm and 64.3 mm, respectively.

The width of transmission lines was chosen as 0.8 mm to achieve a characteristic impedance of 50 Ω, suitable for RF and microwave applications. Substrate properties, operating frequency, and manufacturability are considered in this choice. Simulations and optimization ensure the width meets design requirements, minimizing signal loss and reflections.

Mitered bends are used in microstrip lines to reduce discontinuities and reflections caused by 90° bends. Thus, impedance matching, minimized signal reflections and radiation losses, and improved overall signal integrity are maintained. A portion of the bend at a 45° angle was cut off to shorten the path and maintain a consistent impedance for each microstrip line.

The equations used in calculations of transmission line performance evaluations are as follows:

$$\text{Return Loss (RL)} = 20 \times \log_{10}(|\Gamma|) \tag{3.1}$$

Here, the reflection coefficient Γ is defined as:

$$\Gamma = \frac{Z_L - Z_0}{Z_L + Z_0} \tag{3.2}$$

where Z_L is the load impedance and Z_0 is the characteristic impedance.

The reflected power is given by:

$$\text{Reflected Power} = |\Gamma|^2 \tag{3.3}$$

The transmitted power is given by:

$$\text{Transmitted Power} = 1 - |\Gamma|^2 \tag{3.4}$$

where $|\Gamma|$ is the magnitude of the reflection coefficient.

The insertion loss is calculated by:

$$\text{Insertion Loss (IL)} = -10 \times \log_{10}\left(\frac{P_{\text{out}}}{P_{\text{in}}}\right) \tag{3.5}$$

where P_{in} is the input power and P_{out} is the output power.

3.3.1.1 Γ-Line

This section shows simulation results for a single Γ-line, a patch and a Γ-line, two patches, and a Γ-line. Here, the aim was to achieve a gamma line obeying the length condition given in Equation 3.3.1. For this purpose, the theoretical transmission line length was calculated, and the parameter optimization tool of HFSS was utilized to attain the desired s-parameters and phase result. The simulation results show slight deviations from calculations as a feed line with 5 mm length and 1 mm width is used to feed the sub-components.

In Figures 3.19, 3.20 and 3.21, the return loss (S11), insertion loss (S21) and phase plots of a single Γ-line are shown. In the return loss plot, the S11 parameter is observed to be -8.55 dB at 6.5 GHz while it is -32.7 dB at 7.15 GHz, which shows a frequency shift. Utilizing Equations 3.1, 3.3 and 3.4 on this observation, it can be concluded that at 7.15 GHz, less than 0.1% of the signal is reflected back, which means most of the signal is transmitted forward. In the insertion loss plot, the S21 parameter is -0.3 dB at 7.15 GHz, while it is -0.93 dB at 6.5 GHz. Deploying these findings on Equation 3.5, it is calculated that the signal loses about 18.72% of its power at 6.5 GHz and 7% of its power at 7.15 GHz as it passes through the transmission line.

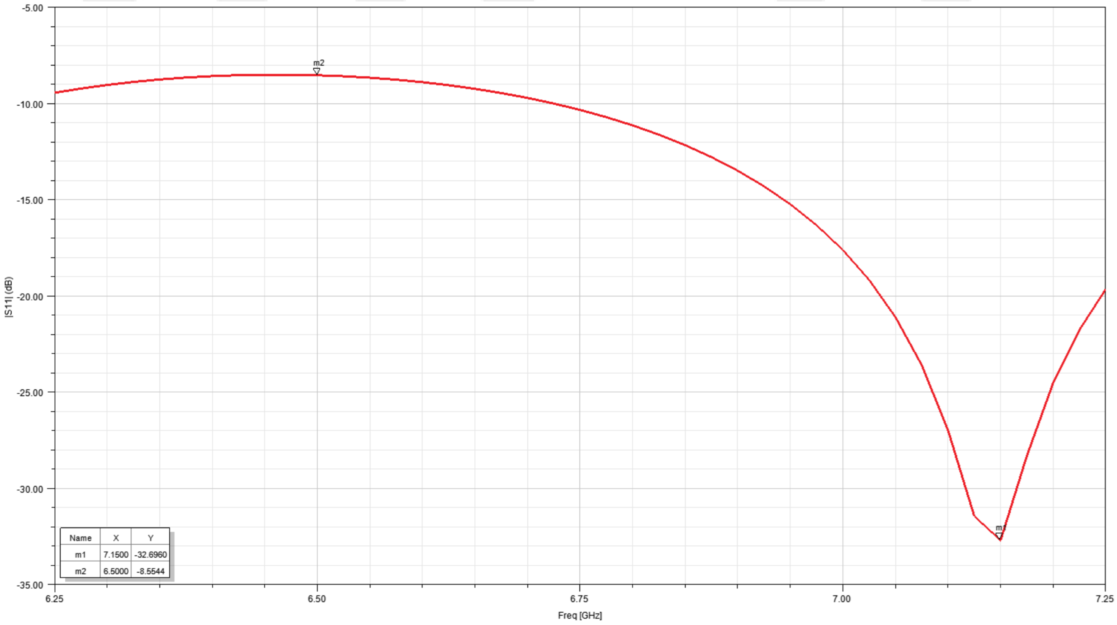

Name	X	Y
m1	7.1500	-32.6960
m2	6.5000	-8.5544

Figure 3.19 Γ-Line Return loss vs. frequency

Lastly, the phase for Γ-line was intended to be 270° at the design considerations, yet it is simulated to be $-98.21°$ at phase plot in Figure 3.21. There is a minor acceptable deviation of 8.21° from the intended value.

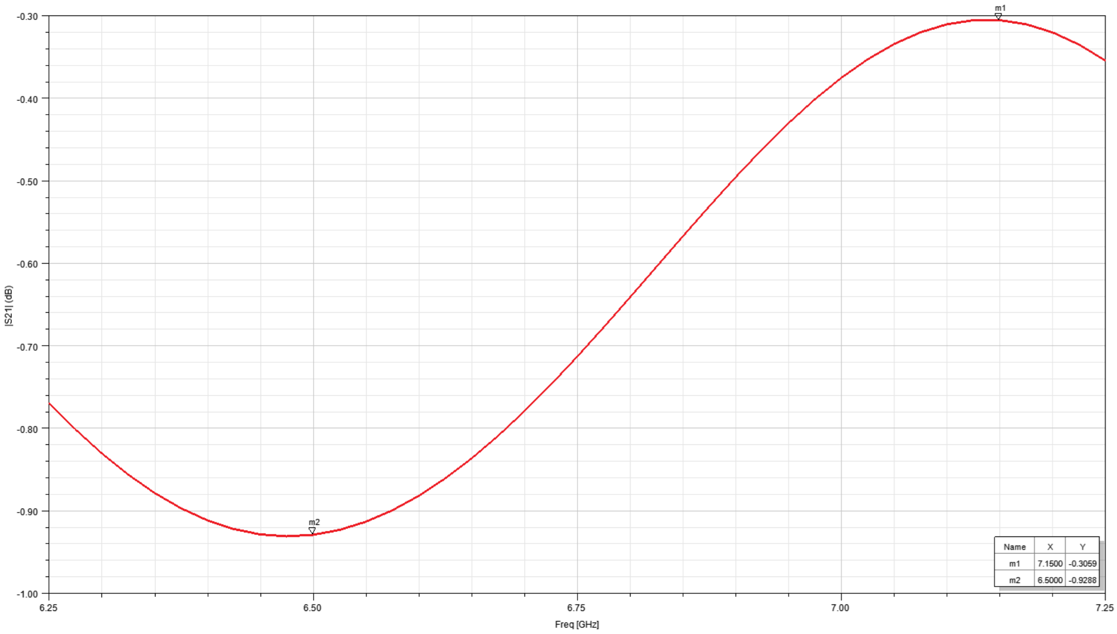

Figure 3.20 Γ-Line Insertion loss vs. frequency

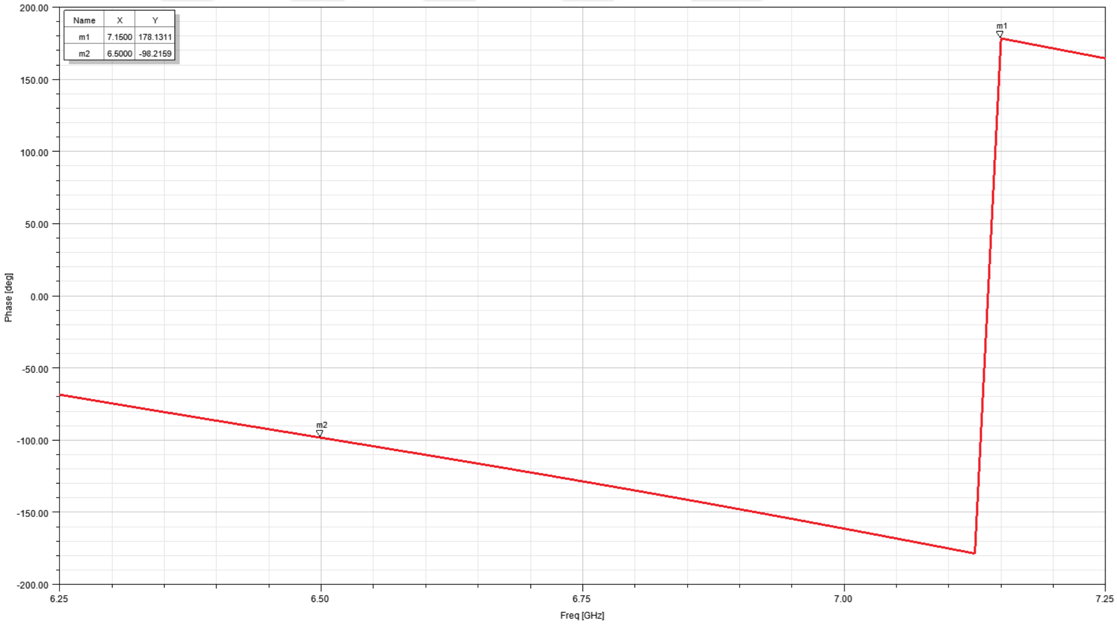

Figure 3.21 Γ-Line Phase vs. frequency

Next, a patch and a feed line are added to the Γ-line, the resulting geometry is displayed in 3.22, and simulations were performed in the same manner. In Figures 3.23, 3.24 and 3.25, the return loss (S11), insertion loss (S21) and phase plots of a patch and a Γ-line are shown. In the simulated return loss plot, the S11 parameter is obtained as -7.58 dB at 6.5 GHz and -20.4 dB at 6.675 GHz. A frequency shift again aroused as in the preceding case.

In the insertion loss plot, the S21 parameter is -1.1 dB at 6.7 GHz, while it is -2.05 dB at 6.5 GHz. Here, it can be noticed that the component becomes less efficient as transmitted power reduces and more power is lost due to the attached patch. The phase of the sub-component is marked as approximately 30° at 6.5 GHz.

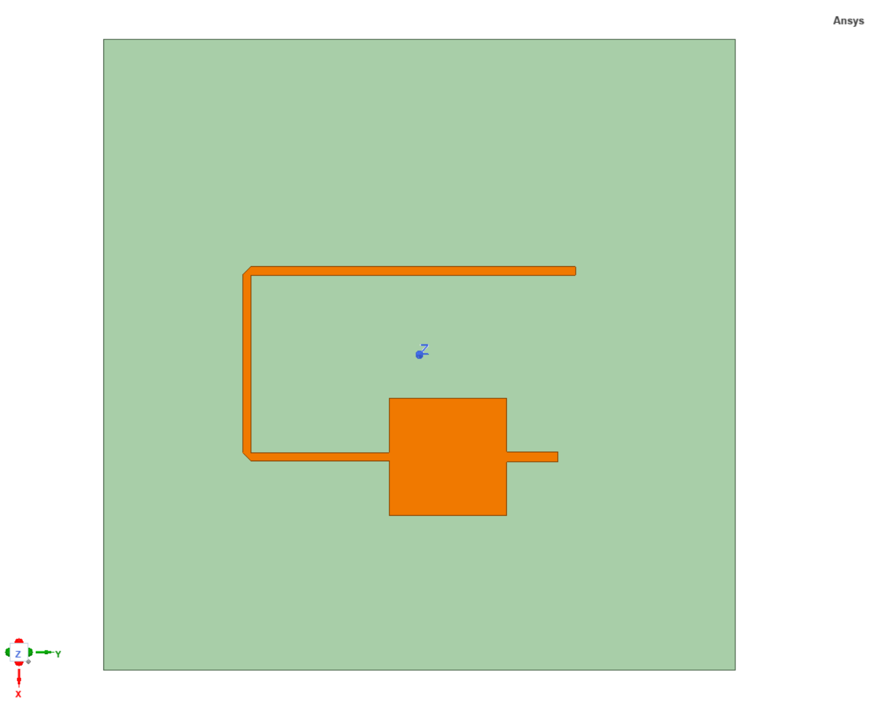

Figure 3.22 Patch and Γ-Line

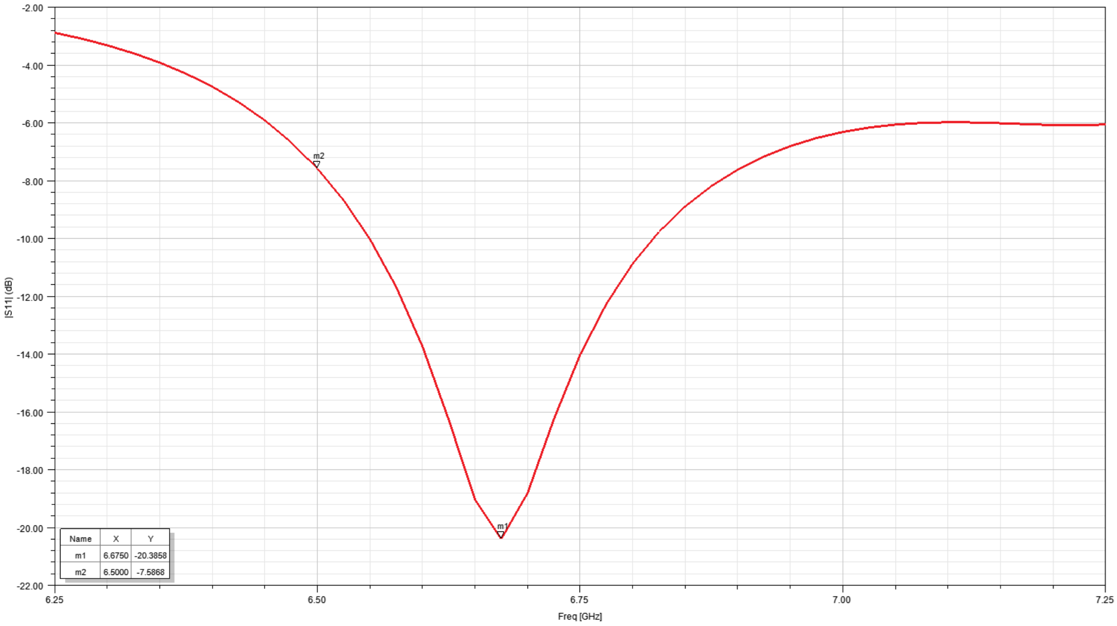

Figure 3.23 Patch and Γ-Line Return loss vs. frequency

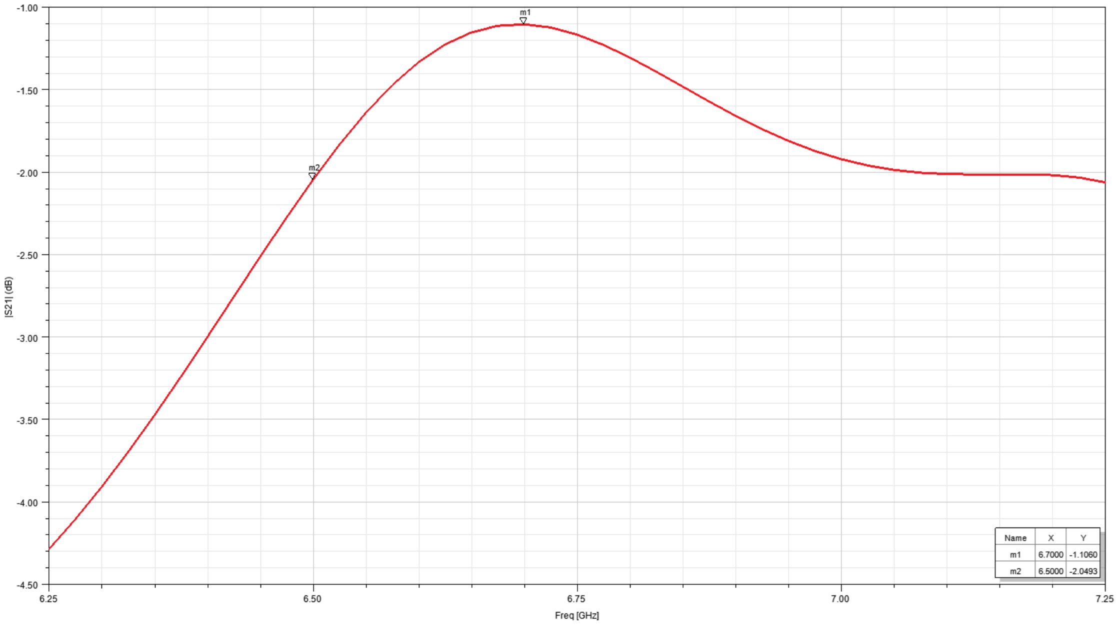

Figure 3.24 Patch and Γ-Line Insertion loss vs. frequency

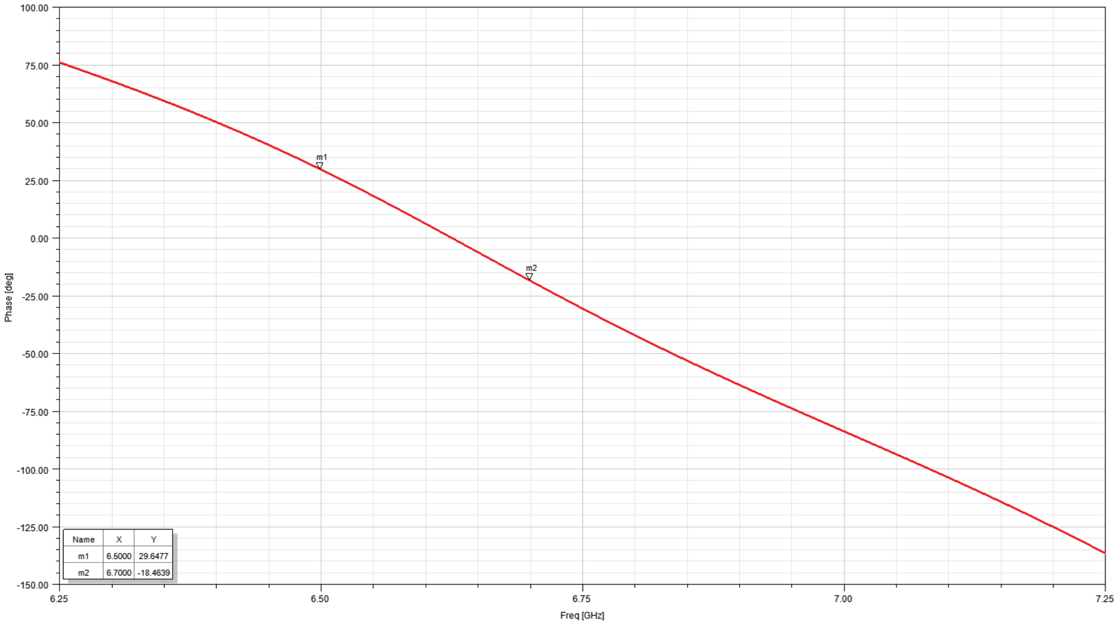

Figure 3.25 Patch and Γ-Line Phase vs. frequency

As a further step, another patch is attached to the previous structure, which can be seen in Figure 3.26. In Figure 3.27, the S11 parameter is -21.5 dB in 6.525 GHz and -14.77 dB in 6.825 GHz. The -10 dB bandwidth is approximately 500 MHz. In the insertion loss plot shown in 3.28, the S21 value is -2.16 dB at 6.5 GHz, whilst it is -2.28 dB at 6.9 GHz. The same bandwidth is also noticeable in this plot.

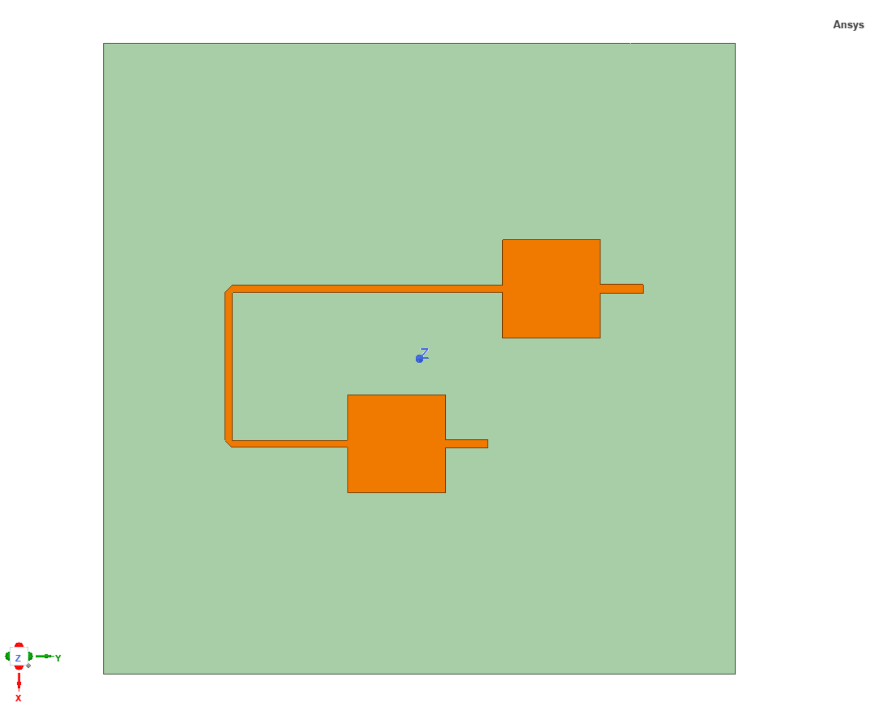

Figure 3.26 2 patches and Γ-Line

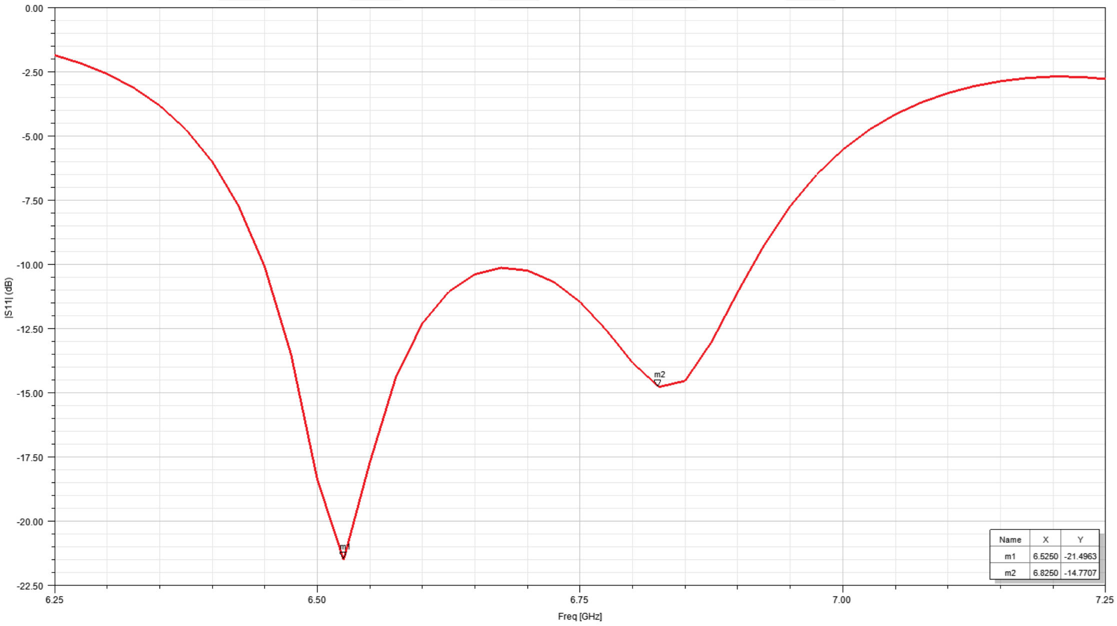

Figure 3.27 2 patches and Γ-Line Return loss vs. frequency

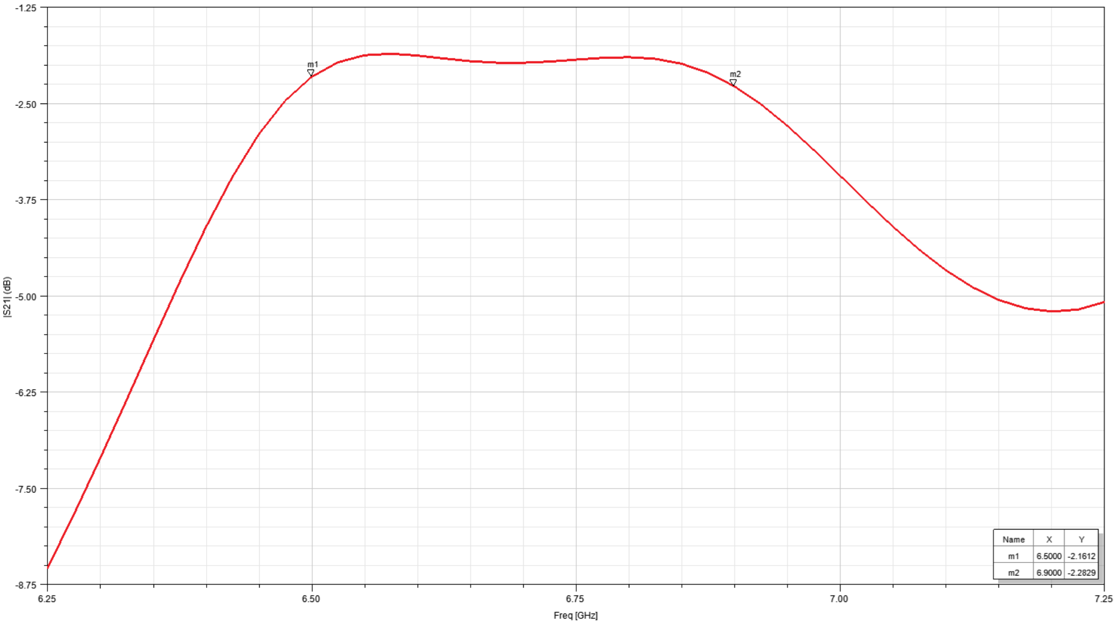

Figure 3.28 2 patches and Γ-Line Insertion loss vs. frequency

The phase vs. frequency graph for the sub-component, including two patches and a Γ-Line, can be seen in Figure 3.29. In this graph, the phase is 153.5° at 6.5 GHz and 43.13° at 6.825 GHz. These phase values are affected by two feed lines connected to the patches.

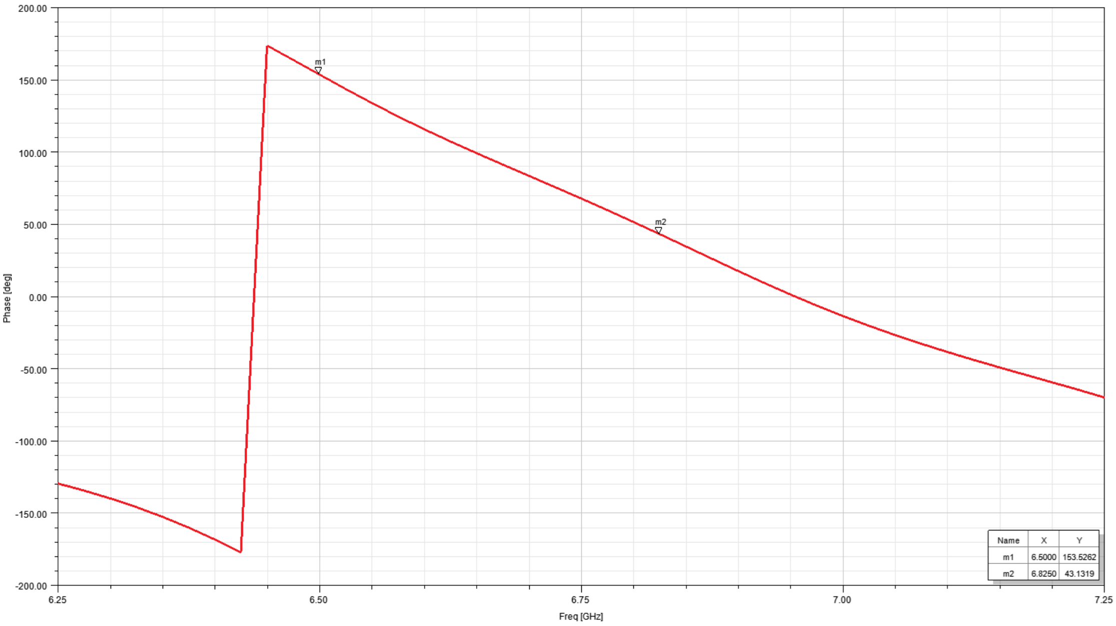

Figure 3.29 2 patches and Γ-Line Phase vs. frequency

3.3.1.2 S-Line

In this section, the same process followed for the Γ-line was also repeated for the s-line. The simulation results for a single s-line, a patch, and an s-line, as well as two patches and an s-line, are given. The length of the s-line was determined considering the length criteria in 3.3.1 to satisfy the phase difference between array elements and radius of the UCA as it highly affects the length of this particular line since the available space is limited. To this end, the theoretical s-line length is calculated to guarantee a 90° phase difference between two patches. Then, the calculated length is slightly changed using parameter sweep and optimization tools of HFSS to have better simulation results serving the ultimate goal of generating OAM modes through the designed UCA antenna.

Figures 3.30, 3.31, and 3.32 demonstrate the return loss, insertion loss, and phase plots of a single s-line, respectively. In the return loss plot, the S11 parameter is observed to be -11.83 dB at 6.5 GHz and shows a decreasing behavior with increasing frequency. It has the best value of -28.15 dB at 7.25 GHz, which is the maximum value in the specified frequency range. By making use of Equations 3.1, 3.3 and 3.4, it can be concluded that at 7.15 GHz, less than 0.1% of the signal is reflected back, which means most of the signal is transmitted forward. This indicates that at 6.5 GHz, approximately 92.6% of the power is transmitted, and around 7.4% is reflected back, while at 7.25 GHz, 0.16% of the power is reflected, and approximately 99.84% of the power is transmitted.

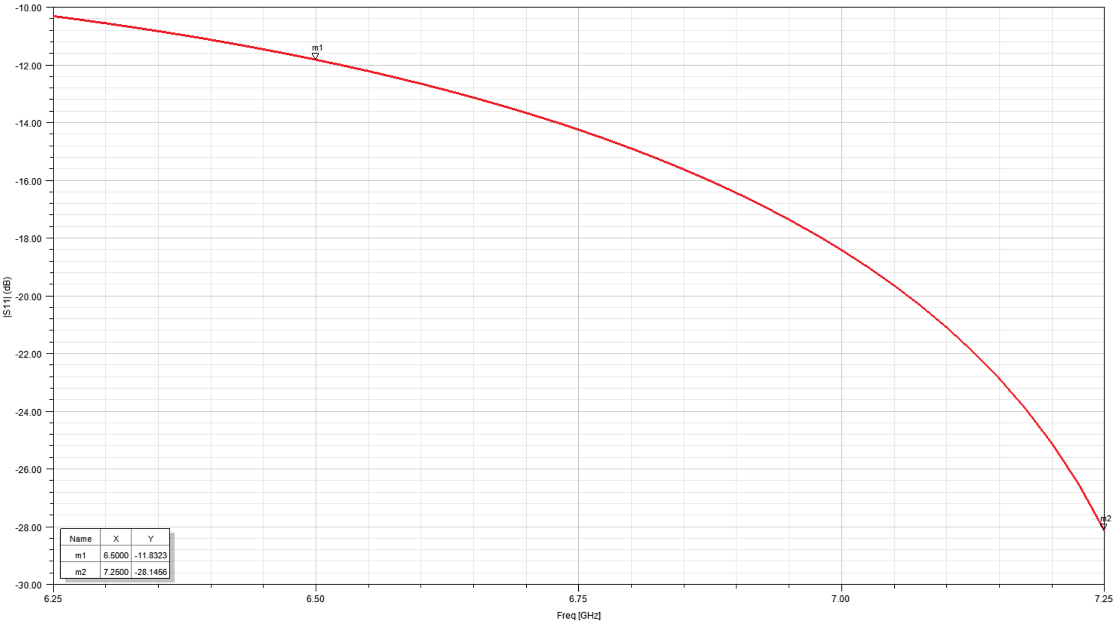

Figure 3.30 S-Line Return loss vs. frequency

In the insertion loss plot, the S21 parameter is -0.14 dB at 7.25 GHz, while it is -0.4 dB at 6.5 GHz, which is in harmony with return loss results as better performance is observed at 7.25 GHz than at 6.5 GHz. At 7.25 GHz, the transmission line exhibits very low signal loss, with only about 3.2% of the signal power being lost, while it is slightly higher at around 8.9% at 6.5 GHz. It could be concluded that the s-line shows more promising results compared to the Γ-line in terms of return loss and insertion loss performances.

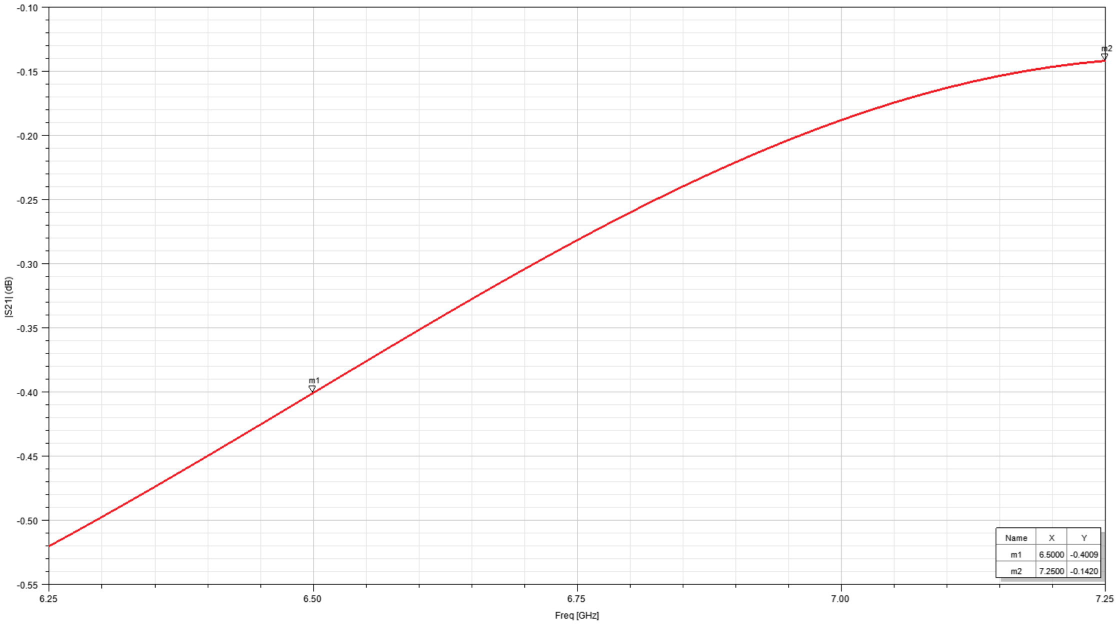

Figure 3.31 S-Line Insertion loss vs. frequency

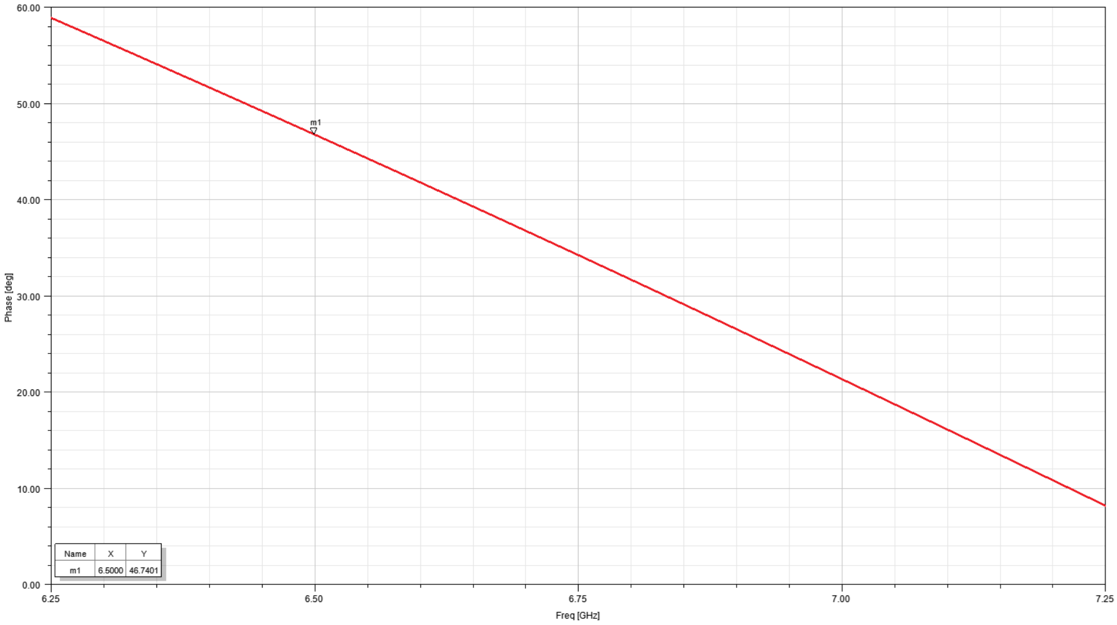

Figure 3.32 S-Line Phase vs. frequency

In Figure 3.32, the phase is observed to be 46.74°, while the design goal was to achieve 90° for the s-line. There is a deviation of half from the desired value.

As the next step, a patch is attached to the s-line, and the new structure can be seen in Figure 3.33.

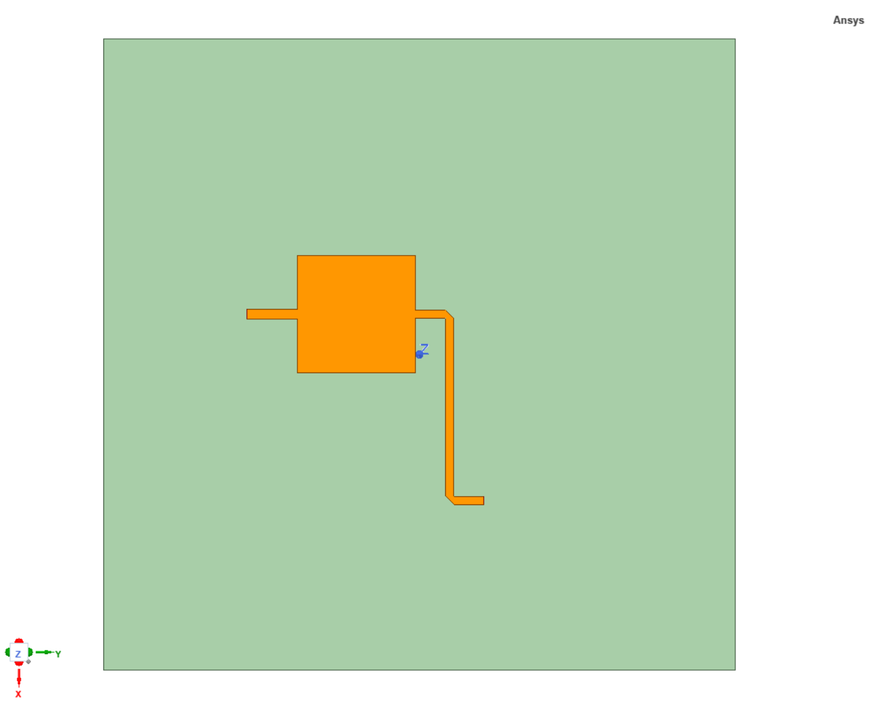

Figure 3.33 Patch and S-line vs. frequency

In Figure 3.34, the S11 parameter is -11.94 dB at 6.65 GHz and -9.95 dB at 6.5 GHz. The -10 dB bandwidth is approximately 300 MHz. These results are acceptable with 6.35% reflected power, meaning 93.65% transmitted power at 6.65 GHz, while approximately 10.11% reflected power and 89.89% transmitted power. In the insertion loss plot shown in 3.35, the S21 value is -1.56 dB at 6.5 GHz and -1.23 dB at 6.675 GHz. This indicates that at 6.5 GHz, the signal loss is 30.2%; in other words, only 69.8% of the power is successfully transmitted, while at 6.675 GHz, the signal loss is lower at 25%, meaning that 75% of the power is transmitted.

The phase vs. frequency graph for the new structure, including a patch and an s-line, can be seen in Figure 3.36. In this graph, the phase is 166.71° at 6.5 GHz and 141.69° at 6.675 GHz. These phase values are affected by the feed line connected to the patch.

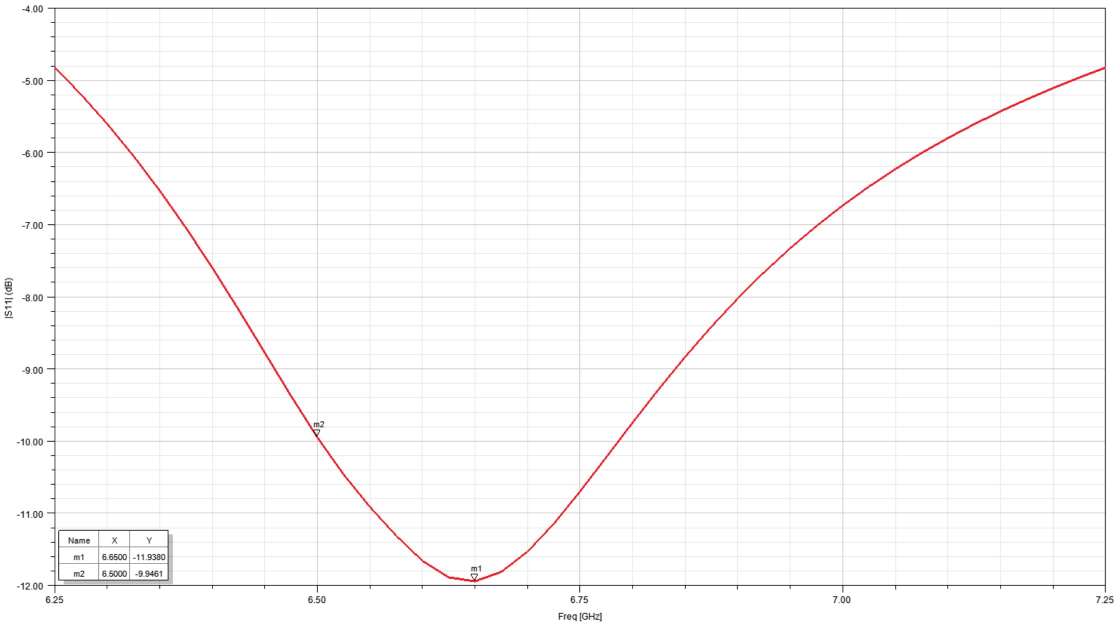

Figure 3.34 Patch and S-line Return loss vs. frequency

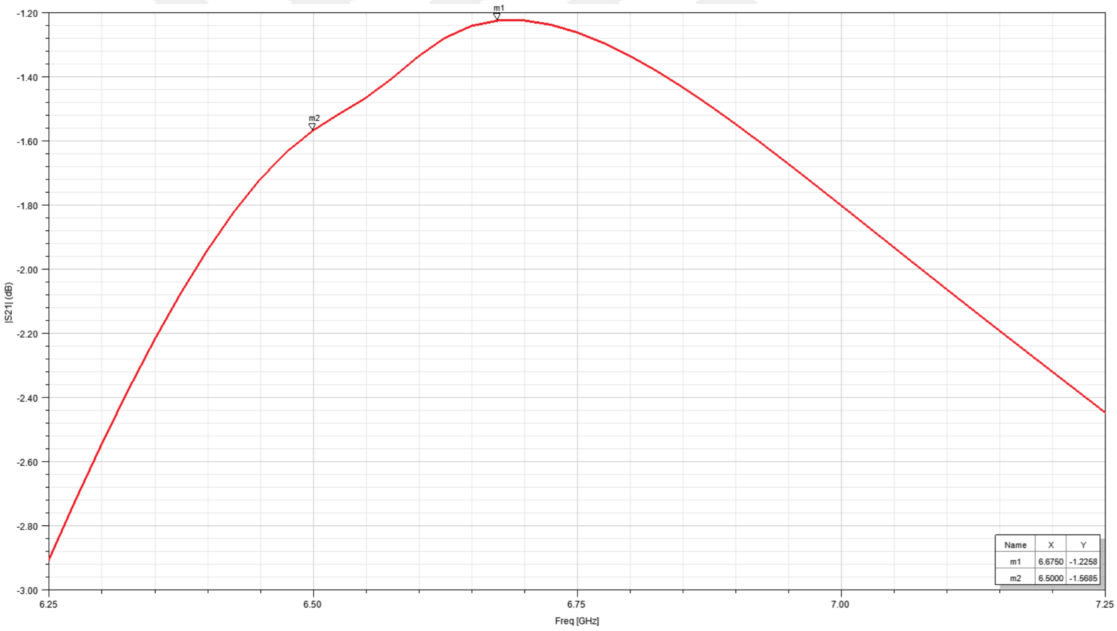

Figure 3.35 Patch and S-line Insertion loss vs. frequency

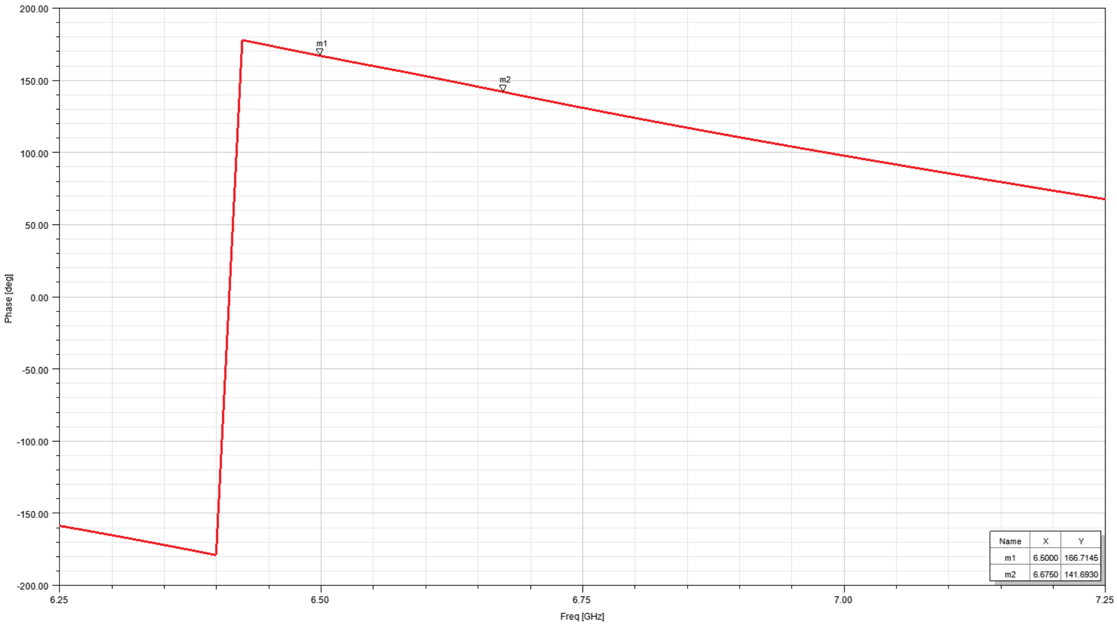

Figure 3.36 Patch and S-line Phase vs. frequency

Lastly, one more patch is adjoined to the empty side of the s-line, and the obtained sub-component can be seen in Figure 3.37, and the same results are generated in simulation. In Figures 3.38, 3.39 and 3.40, the return loss (S11), insertion loss (S21), and phase plots of the latest design are shown. In the return loss plot, the S11 parameter is obtained as -13.27 dB at 6.25 GHz while it is -14.72 dB at 6.825 GHz. A frequency shift appeared as in the same step of the Γ-line case.

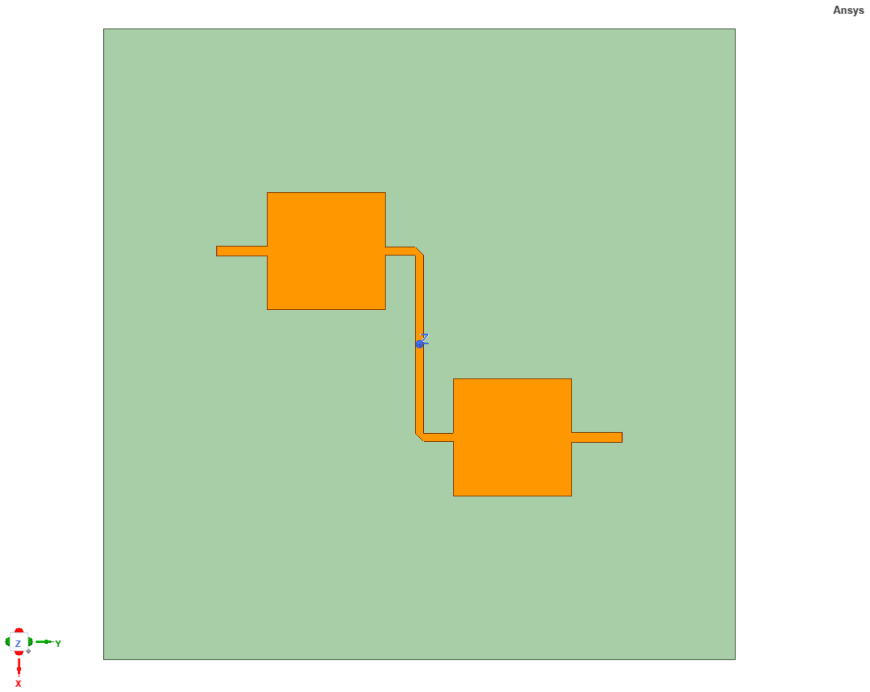

Figure 3.37 2 patches and S-line

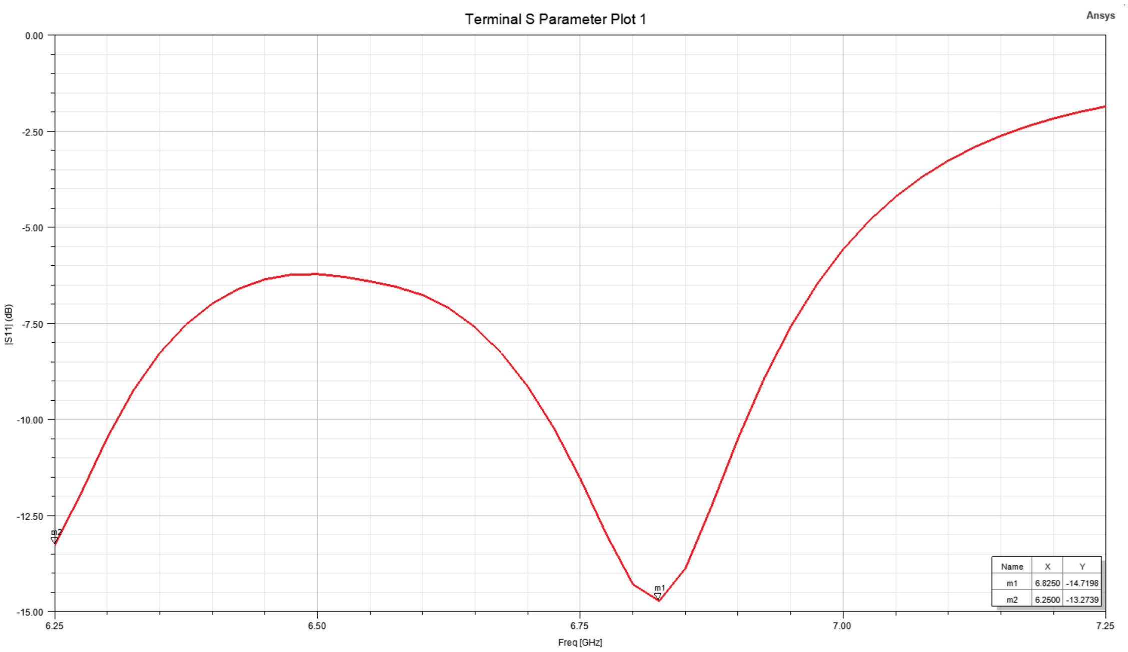

Figure 3.38 2 patches and S-line Return loss vs. frequency

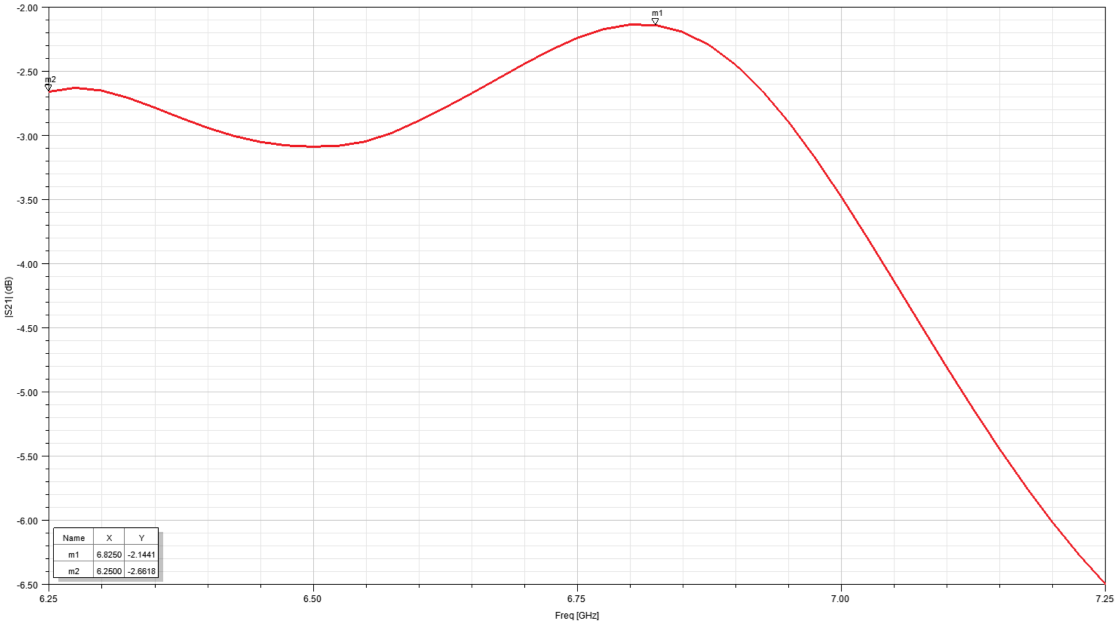

Figure 3.39 2 patches and S-line Insertion loss vs. frequency

In insertion loss plot, S21 parameter is -2.66 dB at 6.25 GHz, while it is -2.14 dB at 6.825 GHz. As can be observed by comparing these results with the previous ones, the transmitted power decreases, and the additional patch makes the system less efficient as more power is lost. The phase of the sub-component is derived as $-83°$ at 6.5 GHz and $-152.13°$ at 6.825 GHz in Figure 3.40.

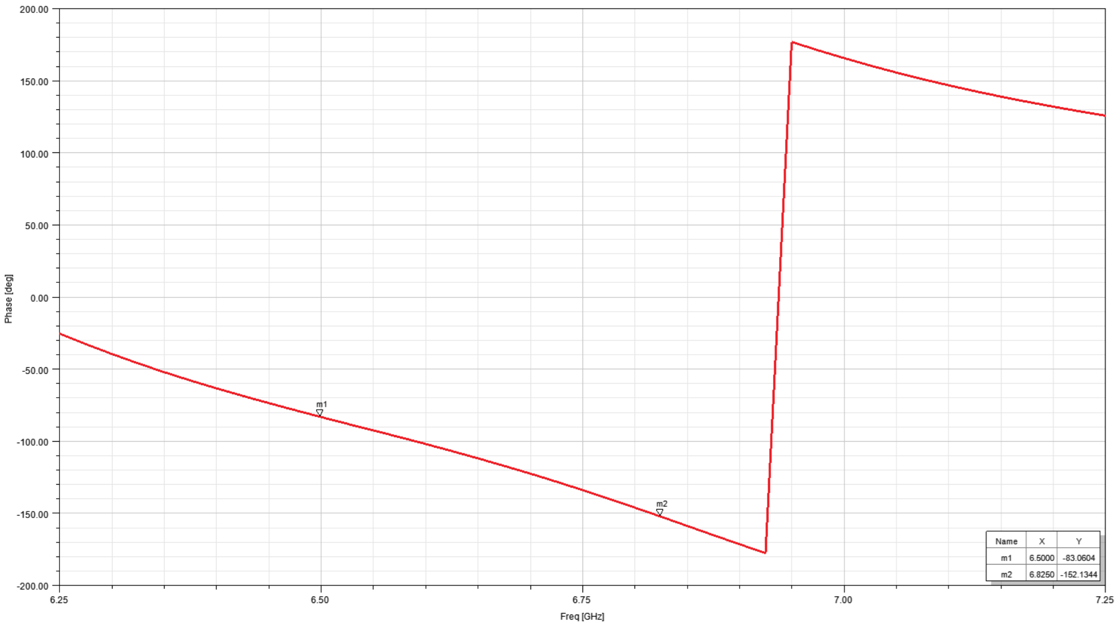

Figure 3.40 2 patches and S-line Phase vs. frequency

After getting results for two different type transmission lines separately, a Γ-line, a patch, and an s-line are assembled, which can be found in 3.41, and the same plots are checked for this structure. The results play a crucial role in the UCA antenna design procedure as they are building blocks of the final UCA design.

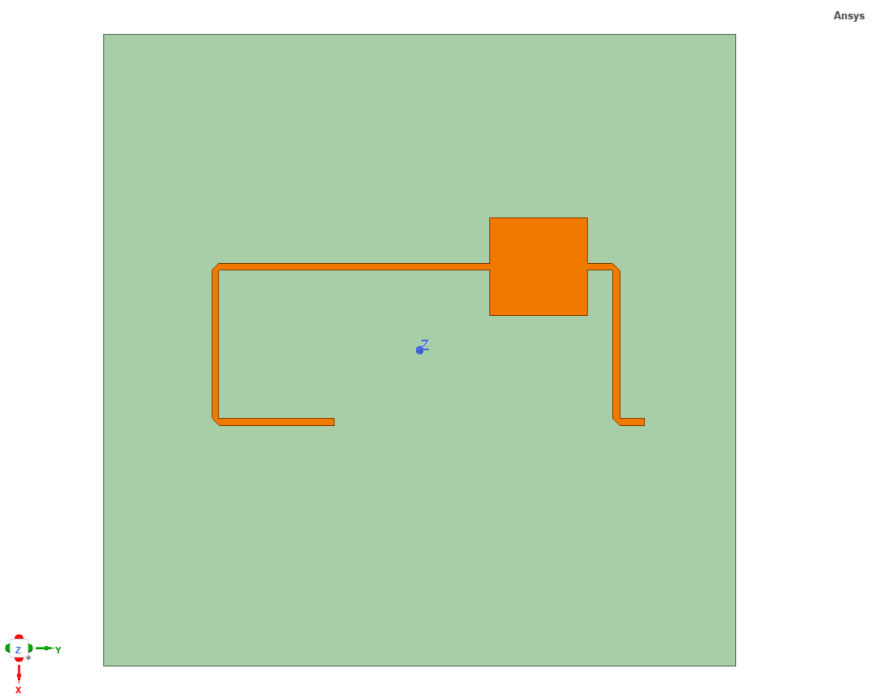

Figure 3.41 Γ-Line, Patch and S-line

Figures 3.42, 3.43, and 3.44 show the return loss, insertion loss, and phase plots, respectively. In Figure 3.42, the S11 values are -10.03 dB at 6.5 GHz and -11.15 dB at 6.6 GHz. S21 values are recorded as -1.71 dB at 6.5 GHz and -1.5 at 6.65 dB. Finally, phase values are found as 144.08° and 105.49° at 6.5 GHz and 6.65 GHz frequencies, respectively.

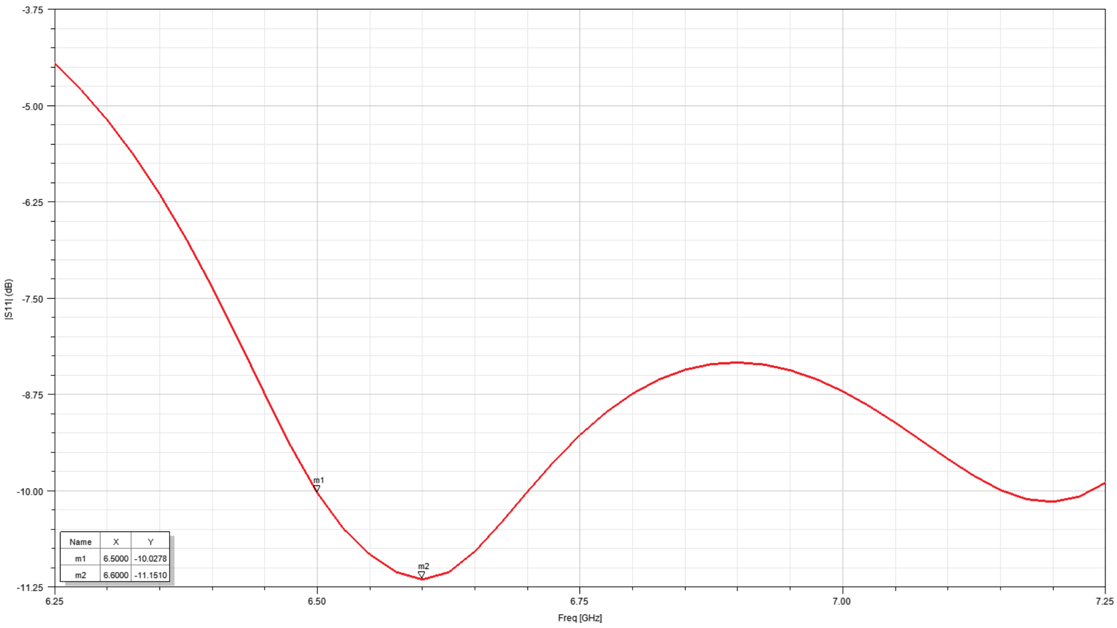

Figure 3.42 Γ-Line, Patch and S-line Return loss vs. frequency

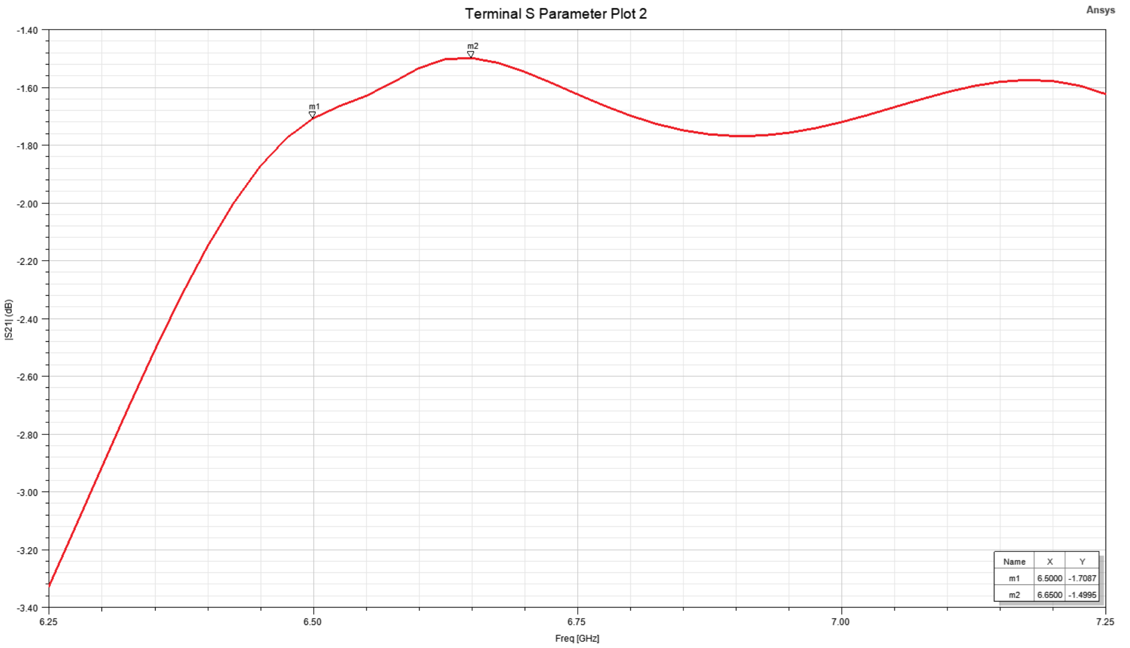

Figure 3.43 Γ-Line, Patch and S-line Insertion loss vs. frequency

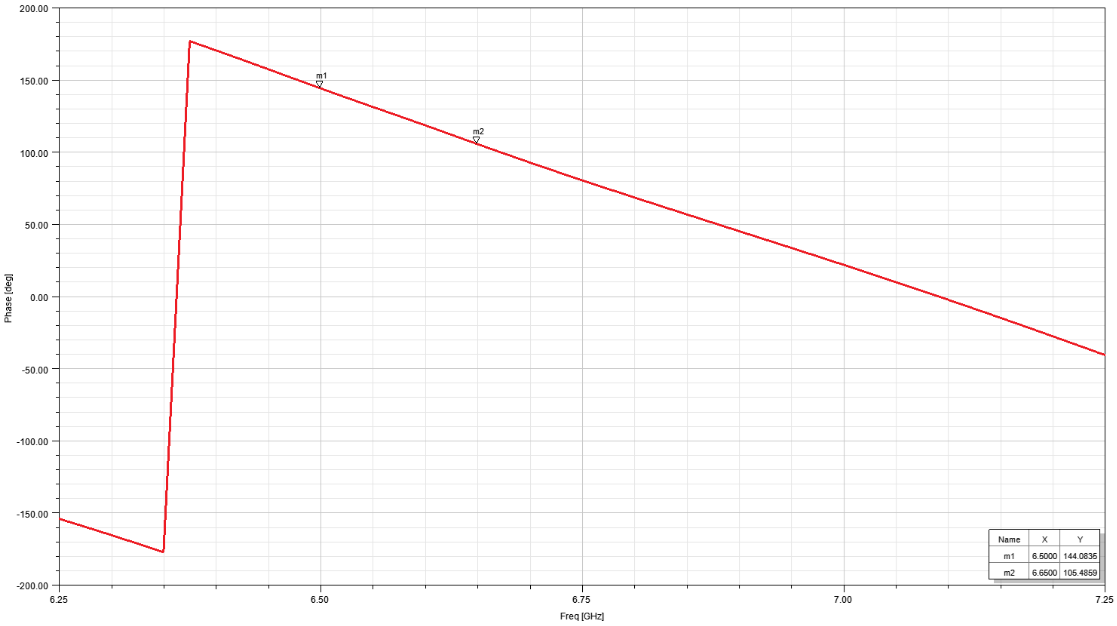

Figure 3.44 Γ-Line, Patch and S-line Phase vs. frequency

3.3.2 Design of OAM Antenna with Linear Polarization

As the final step, the patches in the circular array were connected with microstrip lines to create a two-port system, ensuring that the phase differences between patches were maintained. A diagram of the OAM antenna with physical lengths of design parameters is shown in Figure 3.45. This diagram provides the board's physical lengths, two types of transmission lines, and array radius. Figure 3.46 presents the front view and antenna structure of the complete UCA antenna generating OAM. The s-parameters, 3D radiation pattern, 2D radiation patterns with $\phi = 0°$ and $\phi = 90°$ slices, and the E_x and E_y phase patterns were obtained and can be found in Figures 3.47 to 3.50.

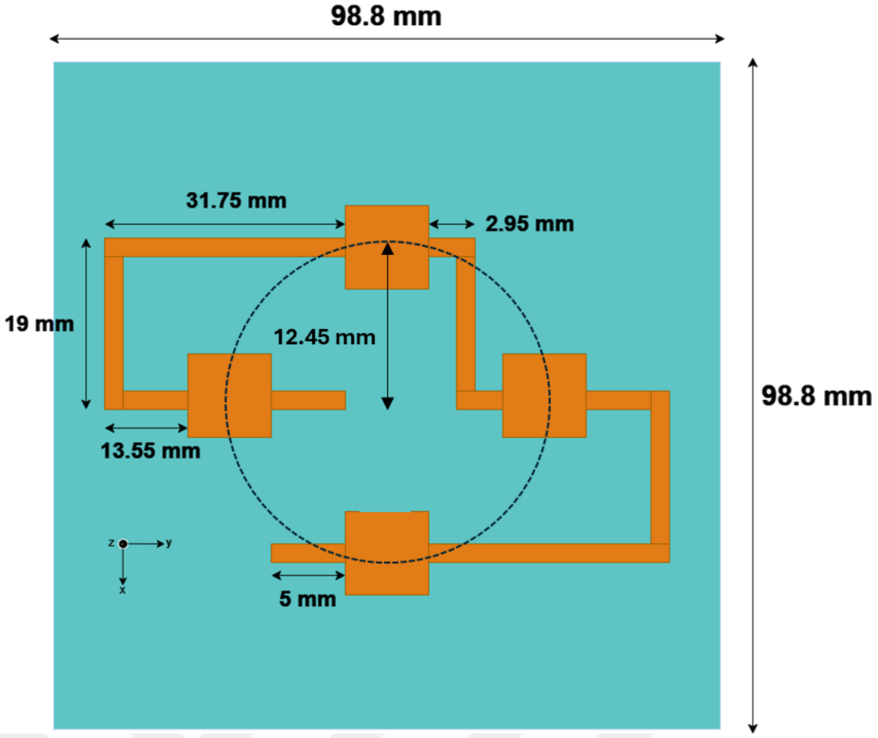

Figure 3.45 Structure of designed OAM antenna with physical lengths

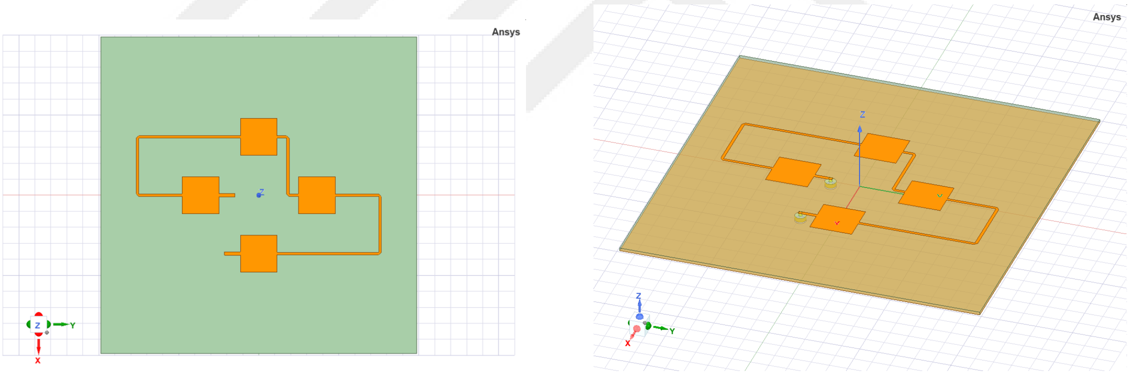

(a) Front view (b) Structure

Figure 3.46 Designed OAM antenna with linear polarization

In Figure 3.47, the antenna exhibits good performance across a 300 MHz bandwidth, with the best impedance matching and efficiency at 6.75 GHz, where the S11 value is -30 dB. This indicates almost no power reflection, making 6.75 GHz the optimal operating frequency. At 6.5 GHz, the S11 value is -15 dB, reflecting about 3.2% of the power, which is still acceptable but not as efficient as at 6.75 GHz. Insertion loss shows a coherent result to return loss, having the best values at the same frequency range.

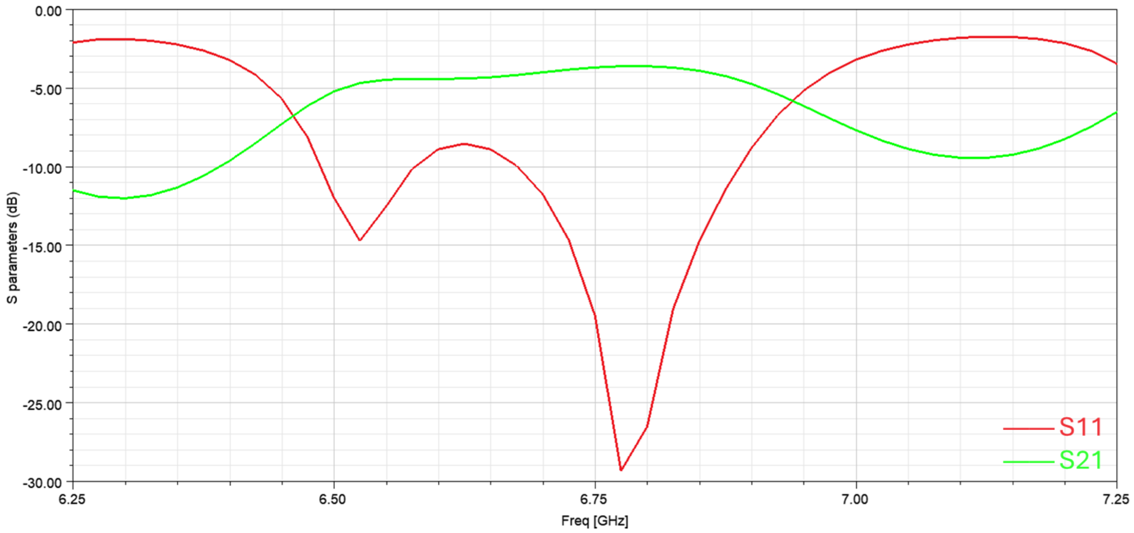

Figure 3.47 S-parameters vs. frequency of the OAM antenna with linear polarization

The radiation pattern in Figure 3.48 shows that the antenna has a maximum realized gain of 5.7 dBi and a singularity observed near the origin. Getting slices from this radiation pattern at $\phi = 0°$ and $\phi = 90°$, the plot in Figure 3.49 is obtained. It shows the antenna's directional characteristics at $\phi = 0°$ and $\phi = 90°$ planes, with strong main lobes indicating effective radiation in these directions. The pattern is generally symmetric but exhibits slight variations, showing asymmetry in radiation performance. The nulls observed in the pattern occur because the antenna generates OAM, leading to regions of minimal radiation. Overall, the antenna demonstrates directional radiation with specific coverage areas and reduced radiation in certain directions due to OAM generation.

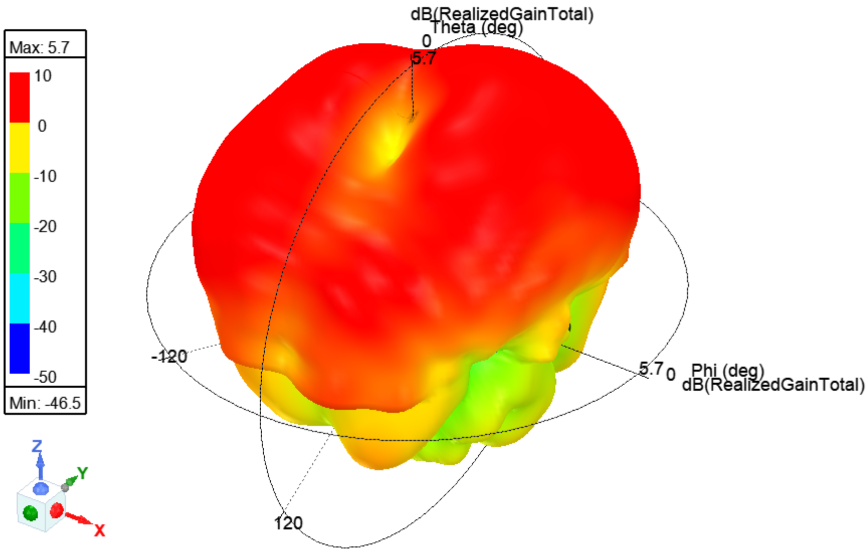

Figure 3.48 3D radiation pattern of the OAM antenna with linear polarization

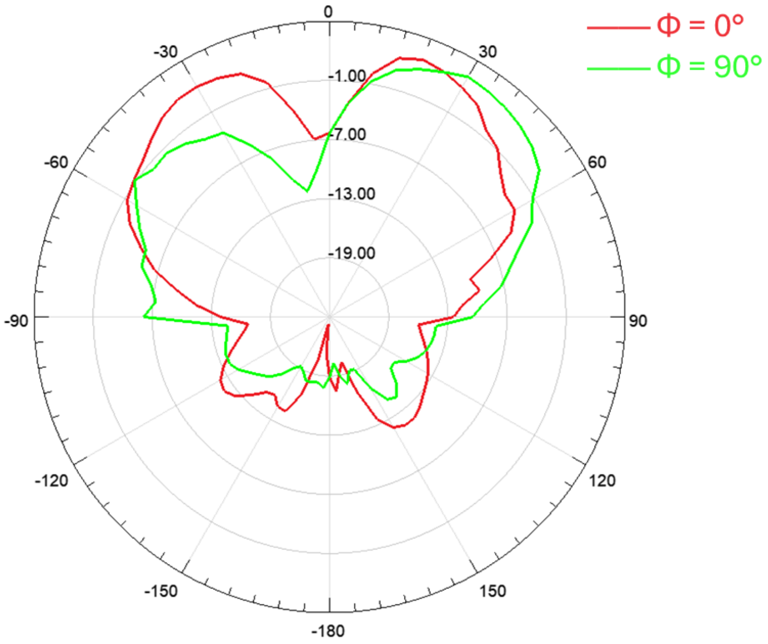

Figure 3.49 2D radiation pattern of the OAM antenna with linear polarization

Different from previous observations, phase patterns were obtained by exciting P1 and P2 separately and can be seen in 3.50. For linear polarization, the phase patterns were in reverse order for different feeding cases. When different ports are excited, the increasing phase order of the antenna elements changes (e.g., in a CW or CCW direction), altering the rotation of the phase pattern. The E_x phase was not in rotational form, but the E_y phase was. This occurs because, in linear polarization, the E_x and E_y components are not inherently phase-shifted by 90°, resulting in a lack of rotational symmetry for the E_x component. In contrast, the E_y component retains some rotational characteristics due to the array configuration.

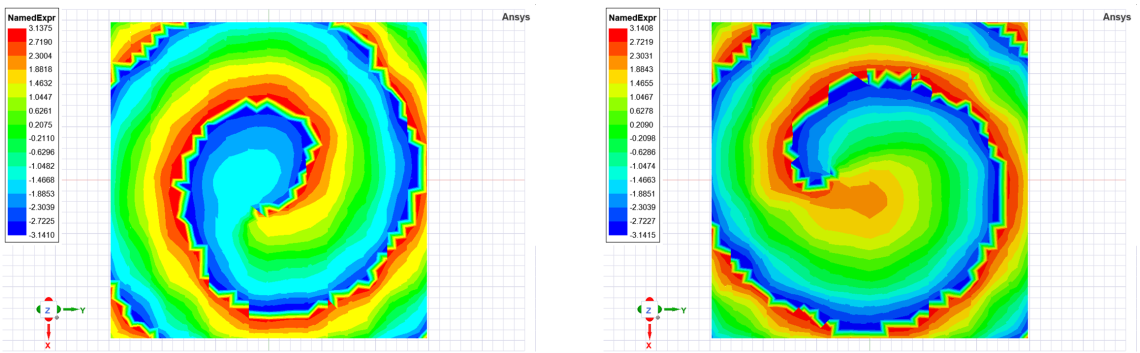

(a) E_y phase port 1

(b) E_y phase port 2

Figure 3.50 Phase pattern of the OAM antenna with linear polarization

3.3.3 Design of OAM Antenna with Circular Polarization

As in the linear polarization case, the patches in the circular array were connected with microstrip lines to create a two-port system. The front view and structure showing antenna and transmission line alignment can be found in 3.51. The s-parameters, 3D radiation pattern, 2D radiation patterns with $\phi = 0°$ and $\phi = 90°$ slices, and the E_x and E_y phase patterns were obtained again by exciting P1 and P2 separately and shown in Figures 3.52 to 3.55.

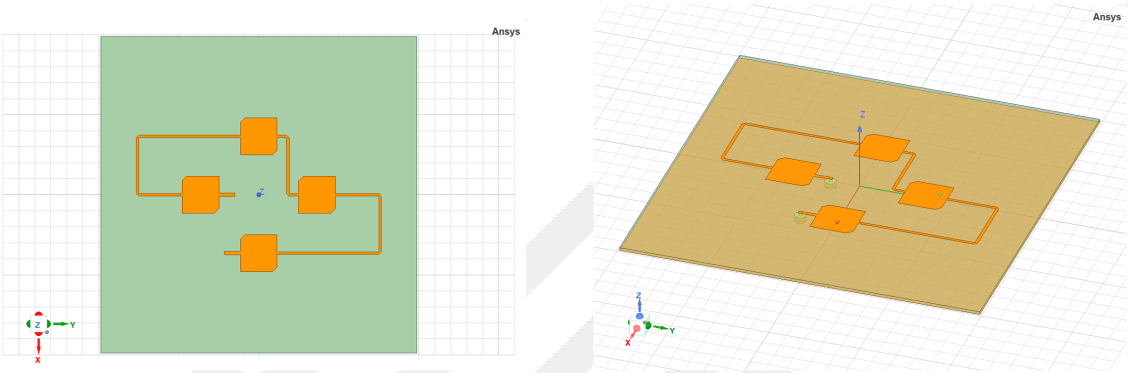

(a) Front view (b) Structure

Figure 3.51 Designed OAM antenna with circular polarization

In Figure 3.52, the OAM antenna shows similar behavior to the linear case, having its best performance between 6.75 and 7 GHz with approximately -20 dB S11 value. It indicates an excellent impedance matching for the antenna, with only 1% of the power reflected and 99% transmitted. Unlike the antenna with linear polarization case, the bandwidth is wider for a circularly polarized antenna with 500 MHz bandwidth. This ensures an efficient performance, minimal signal loss, and effective radiation of the input power at the specified frequency.

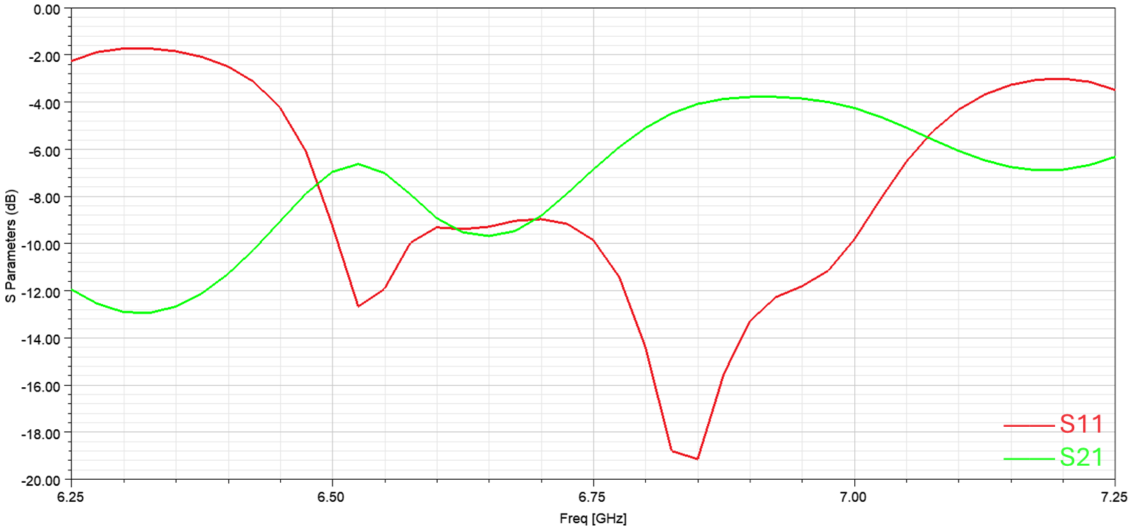

Figure 3.52 S-parameters vs. frequency of the OAM antenna with circular polarization

The radiation pattern in Figure 3.53 shows that the antenna has a maximum realized gain of 5.7 dBic, and a more apparent singularity is observed near the origin. Again, getting slices from this radiation pattern at $\phi = 0°$ and $\phi = 90°$, the plot in Figure 3.54 is obtained. It has strong main lobes indicating effective radiation in these directions, while also has minimal radiation points (nulls or singularities) as clearly seen for $\phi = 0°$. The pattern is more asymmetric compared to the linearly polarized antenna. The nulls are more clearly observed in the pattern caused by OAM generation.

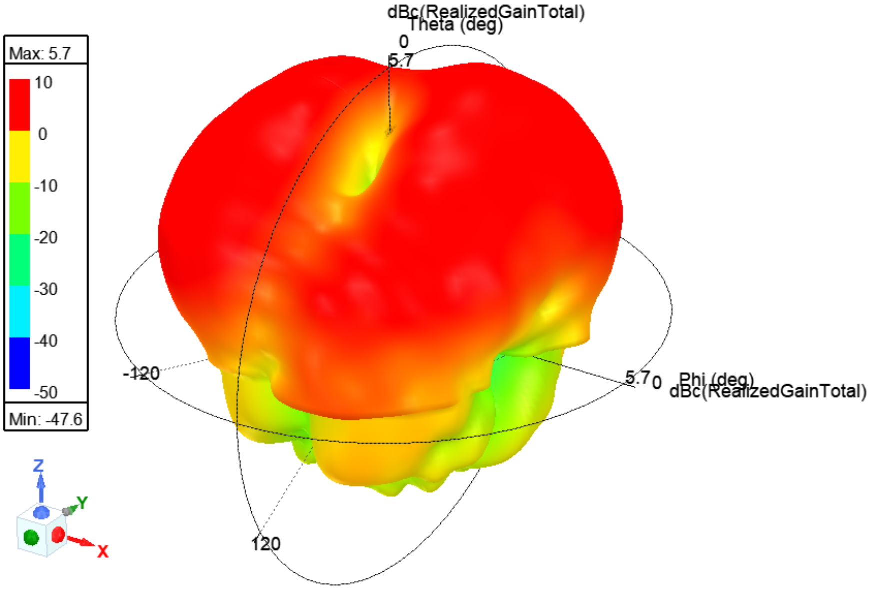

Figure 3.53 3D radiation pattern of the OAM antenna with circular polarization

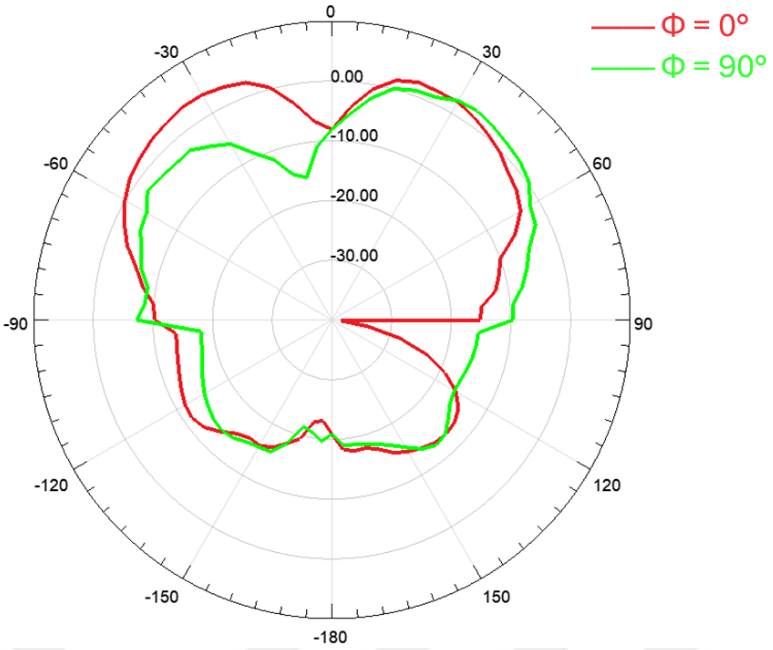

Figure 3.54 2D radiation pattern of the OAM antenna with circular polarization

From 3.55, it could be observed that the phase patterns rotate in reverse order for different feeding cases of the same component of the electric field. Besides, both E_x and E_y phase patterns are in rotational form and are in reverse order to each other. This is because circular polarization involves a 90° phase shift between E_x and E_y components within each patch antenna, which is maintained in the array configuration. When the feeding is switched between ports 1 and 2, the phase relationship between E_x and E_y components is reversed, leading to opposite rotational directions in the phase patterns. This behavior is consistent with the nature of circular polarization, where the orthogonal components rotate synchronously but in opposite directions when the phase relationship is reversed.

The performance and characteristics of the circular array antenna with microstrip line connections differ significantly between the linear and circular polarization cases. In the linear polarization case, the phase patterns for E_x and E_y are observed to rotate in reverse directions, with E_x lacking rotational symmetry, while E_y shows rotational characteristics due to the array configuration. This occurs because, in linear polarization, the orthogonal components of the electric field do not exhibit a natural phase shift, resulting in asymmetry in the phase patterns when a 90° phase shift is introduced between array elements.

Conversely, in the circular polarization case, both E_x and E_y phase patterns exhibit rotational form and are in reverse order relative to each other when fed from different ports. This is a direct result of the intrinsic 90° phase shift between orthogonal components in circular polarization. The synchronized rotational behavior of E_x and E_y components ensures that the circular polarization state is consistently maintained throughout the radiation pattern, even when phase relationships are reversed by switching feed ports.

In conclusion, there occurs a contrast between linear and circular polarization in terms of their phase pattern characteristics. Due to the lack of inherent phase difference between orthogonal components, linear polarization shows diverse rotational characteristics in its phase patterns. On the contrary, circular polarization maintains a consistent rotational form for both E_x and E_y components due to its intrinsic phase shift.

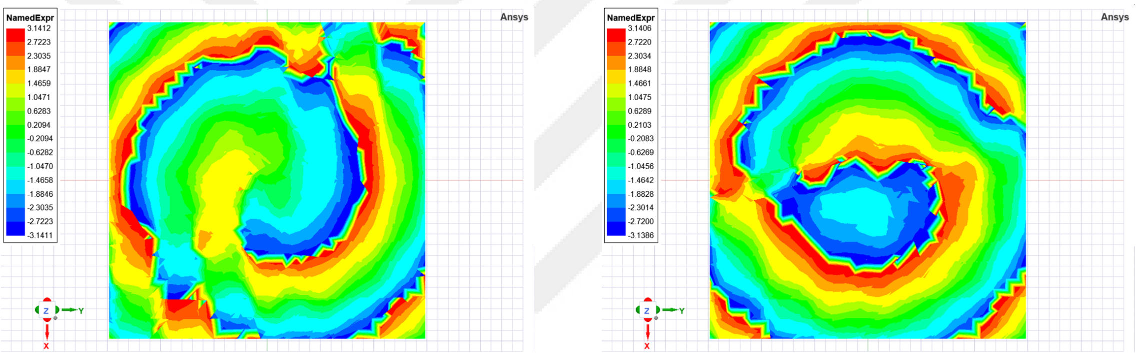

(a) E_x phase port 1

(b) E_x phase port 2

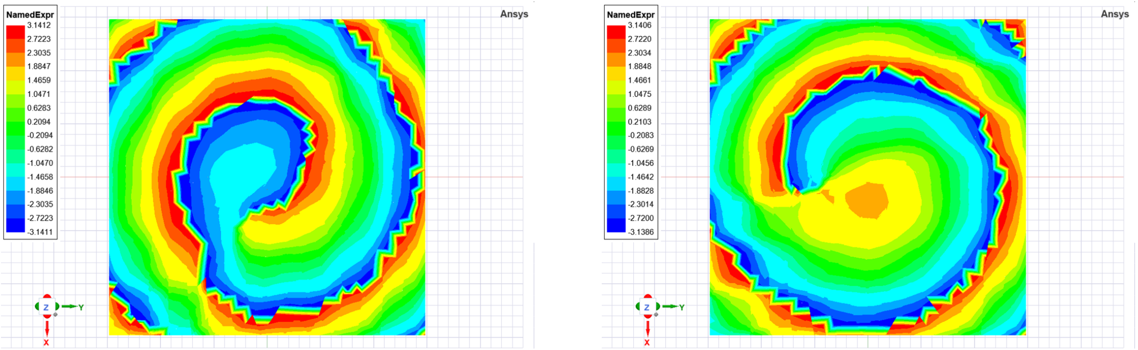

(a) E_y phase port 1

(b) E_y phase port 2

Figure 3.55 Phase pattern of the OAM antenna with circular polarization

4. FABRICATION AND MEASUREMENT

This chapter provides a comprehensive overview of the fabrication process, employed measurement techniques, results and analysis of the designed OAM antennas. The fabrication process and the system used for testing antenna characteristics and performance are introduced in section 4.1 and section 4.2. Measurement results including s-parameters, gain, phase patterns, radiation patterns, and discussions can be found in section 4.3.

4.1 Fabrication

The designed OAM antennas were fabricated using a low-cost PCB prototyping technique with an LPKF Circuit Board Plotter ProtoMat S63 at Sabancı University CoSpace. This method offers cost-effectiveness, rapid prototyping, precision, flexibility, and excellent repeatability, making it ideal for research and development of high-frequency antenna designs. The ProtoMat S63 excels in 2.5-dimensional material machining and features a spindle speed of 60,000 rpm, making it also suitable for drilling test adapters and housing production [33]. This technique ensures high precision and accuracy in intricate details with a minimum line width of 0.1 mm and repeatability of ±0.001 mm [22]. The fabricated OAM antennas with linear and circular polarizations can be seen in Figure 4.1.

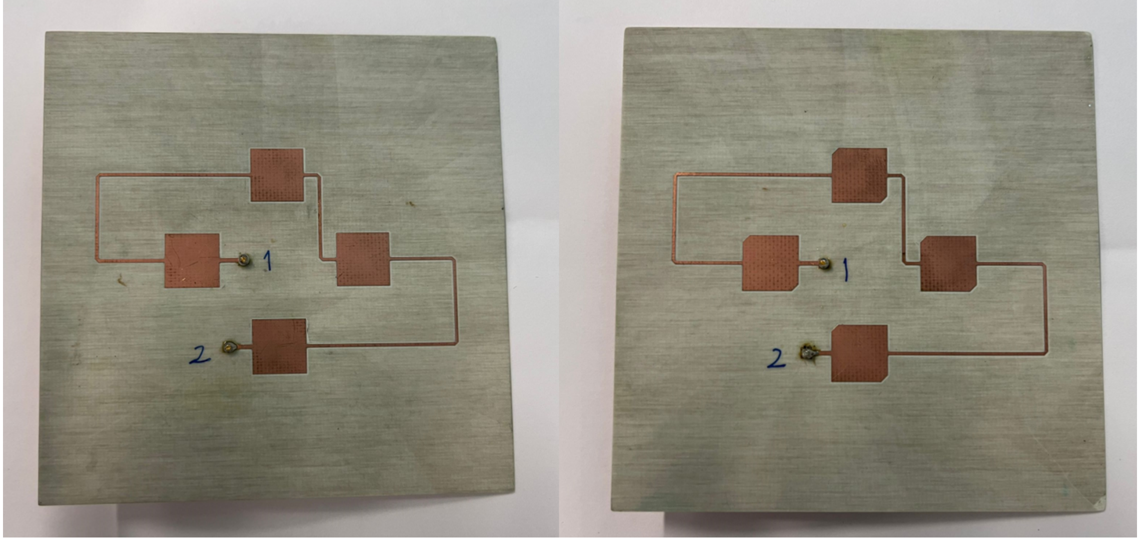

Figure 4.1 Fabricated uniform circular array antennas with linear polarization (left) and circular polarization (right)

After fabrication, Amphenol 132143 connectors are inserted and soldered to the ports of antennas, which can be observed in Figure 4.2. The Amphenol 132143 coaxial connector is selected for its robust design and reliable performance across a broad frequency range, including our 6.5 GHz band. Known for maintaining consistent impedance characteristics and mechanical durability, it ensures efficient signal transmission and longevity in RF and microwave applications [31].

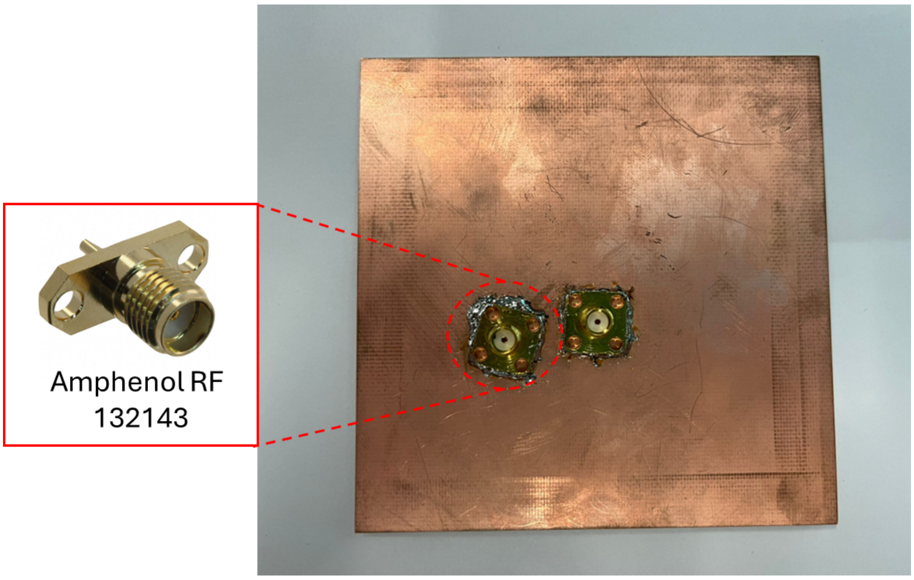

Figure 4.2 Back view of uniform circular array antennas

4.2 Measurement

In order to measure the performance and characteristics of the designed OAM antennas with linear and circular polarizations, the anechoic chamber facility at Sabancı University Nanotechnology Research and Application Center (SUNUM) was used. In this chamber, a reference ANT-SGH-5.85-8.2 standard gain horn antenna, which can be seen in Figure 4.3, is used to measure the radiation pattern and gain of AUT (Antenna Under Test). The standard gain horn antenna used as a reference antenna can be found in Figure 4.3. The AUT was located at a 1.7 m distance from the transmitter antenna (TX), which can be seen in Figure 4.4. In order to measure the gain and radiation patterns of designed antennas, the AUT was rotated in azimuth and elevation axes by 5° intervals.

This facility has an advanced near-field antenna measurement system designed by Nearfield Systems Inc., NSI2000. It ensures comprehensive performance analysis and high accuracy in the characterization of radiation properties. Due to its precise probe and positioning system to scan the near-field region, it captures amplitude and phase data and transforms them into far-field radiation patterns [25]. Various measurement types, including planar, cylindrical, and spherical scanning, are supported. It is widely used in antenna design, development, and quality control of modern wireless communication systems.

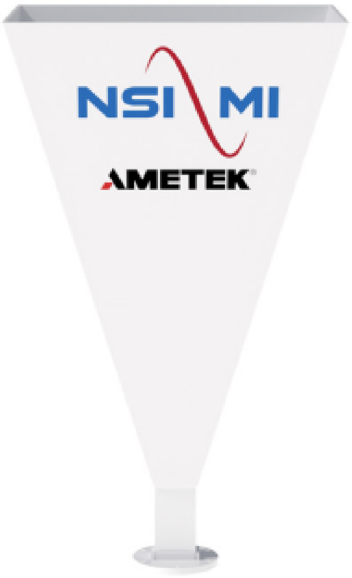

Figure 4.3 Standard gain horn antenna
[28]

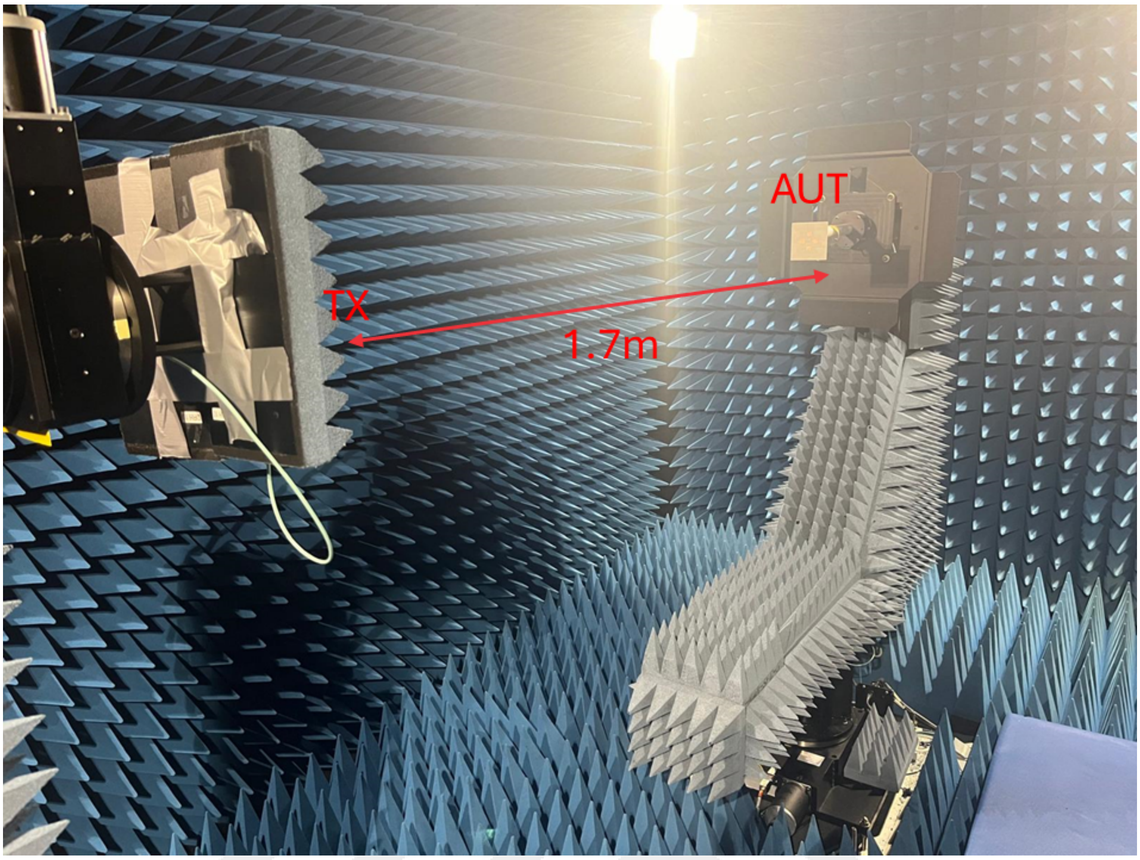

Figure 4.4 The position of AUT and TX in anechoic chamber

4.3 Results & Analysis

Antenna measurements were performed to determine the performance and various characteristics of the designed OAM antennas, such as the S11 parameter for the 4-8 GHz band, gain, and radiation pattern for 6.25 to 7.25 GHz with 100 MHz intervals (for 11 frequency values). The measurements were repeated for different frequencies by exciting different ports and polarizations (horizontal and vertical). The AUT was rotated by 5° for θ between [-90°,90°] and ϕ between [0°,360°]. The fabricated antenna in anechoic chamber showing azimuth and elevation axes can be seen in Figure 4.5. Then, the measurement results were exported as CSV (comma-separated values) files, and the necessary plots were generated using MATLAB R2021b.

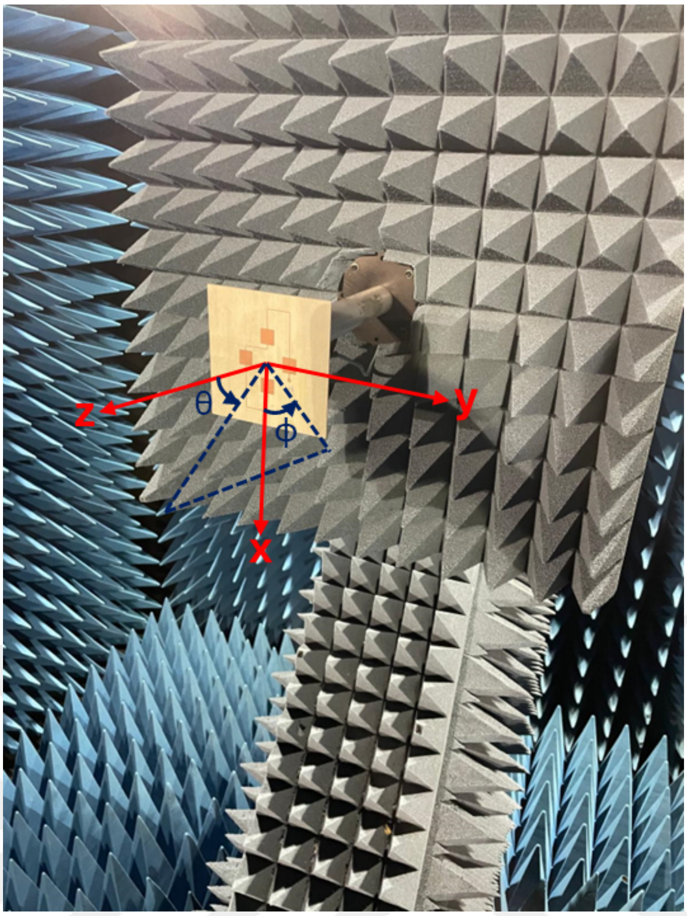

Figure 4.5 Fabricated OAM antenna in measurement setup

During the measurements, gains of both the designed OAM antennas and the standard horn antenna used as the transmitter (TX) were measured. The standard horn antenna functioned as a reference due to its known and stable gain value. This approach leads to more reliable and precise results by comparing the gain characteristics of the designed antennas against an objective reference point. The gain vs. frequency plot of the standard horn antenna for the 6.25 - 7.25 GHz band is shown in Figure 4.6. Using these gain values, normalized gain plots for designed OAM antennas were obtained using Equation 4.1.

(4.1)

$$\mathrm{Gain}_{\mathrm{AUT}} = \mathrm{Gain}_{\mathrm{Measured\ AUT}} + \mathrm{Gain}_{\mathrm{Standard\ Horn\ Antenna}} - \mathrm{Gain}_{\mathrm{Measured\ Horn\ Antenna}}$$

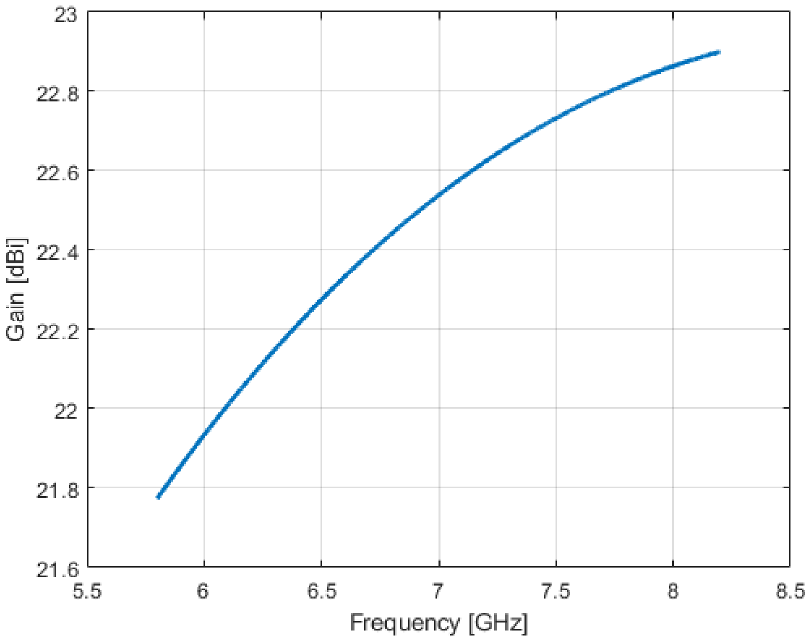

Figure 4.6 Gain vs. frequency for standard horn antenna

4.3.1 OAM Antenna with Linear Polarization

In this section, the measurement results of the OAM antenna with linear polarization are shown. In Figure 4.7, normalized gain vs. frequency plots are shown for port 1 (P1) and port 2 (P2) in (a) and (b) parts, respectively. The gain plot for Port 1 in Figure 4.7(a) shows significant variation across the frequency range of 6.2 GHz to 7.4 GHz. The antenna exhibits strong performance at certain frequencies, particularly around 6.2 GHz and 6.9 GHz, where the gain exceeds 5 dBi. However, there is a sharp drop in gain around 6.4 GHz, with values falling below -15 dBi, indicating a significant reduction in radiated power at that frequency. This suggests that the antenna's efficiency is highly dependent on the operating frequency, with better performance at specific points within the range.

For Port 2 in Figure 4.7(b), the gain also fluctuates with frequency, showing a slightly different pattern than Port 1. The gain is positive, reaching up to 5 dBi around 6.2 GHz and 6.9 GHz, similar to Port 1. However, the gain decreases at frequencies like 6.4 GHz and 7.2 GHz, with the lowest point around -10 dBi. This indicates that while Port 2 has different frequency characteristics, both ports demonstrate frequency-dependent gain variations critical for the antenna's performance in OAM communication systems.

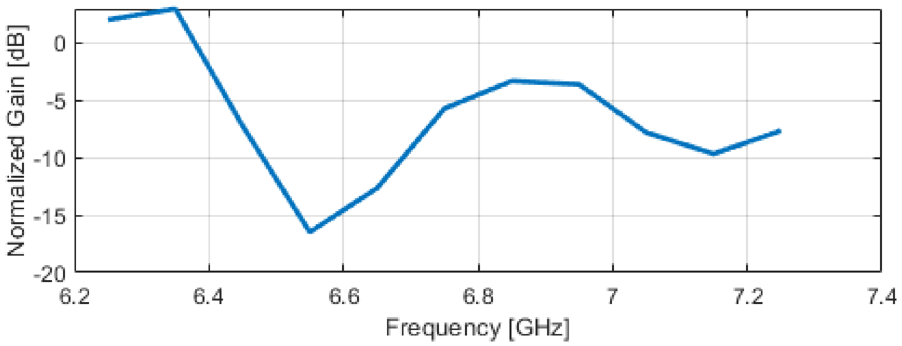

(a) Port 1

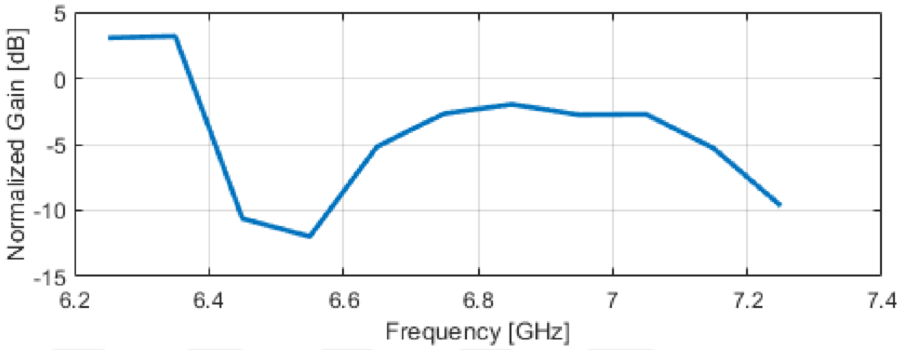

(b) Port 2

Figure 4.7 Normalized gain vs. frequency for OAM antenna with linear polarization

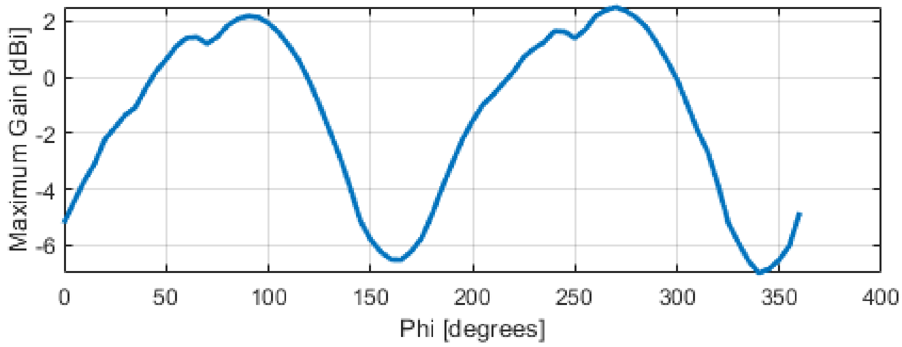

(a) Maximum gain vs. phi

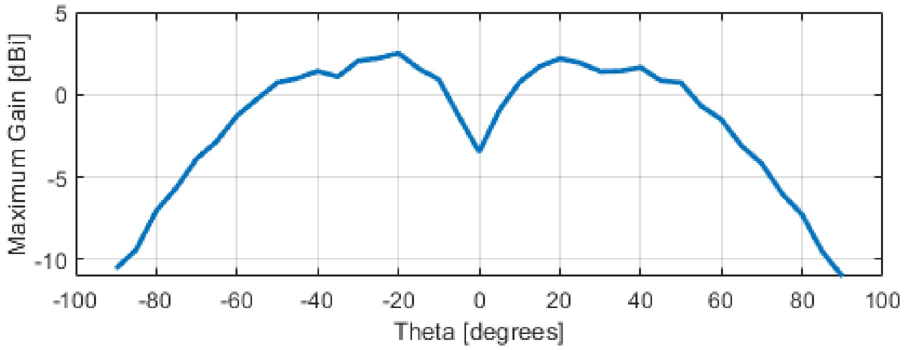

(b) Maximum gain vs. theta

Figure 4.8 Maximum gain vs. angle for Port 1

In Figures 4.8 and 4.9, maximum gain vs. angle plots for Port 1 and 2 are shown, respectively. Figure 4.8(a) shows how the antenna's gain varies with the azimuthal angle (ϕ) from 0° to 360°. The gain pattern is periodic, with peaks around 90°, 210°, and 330°, where the gain reaches approximately 2 dBi. These angles correspond to directions where the antenna radiates most effectively. However, the gain drops significantly near 60°, 180°, and 300°, indicating weaker radiation in those directions, with the gain nearing 0 dBi. These points of weaker radiation are known as singularity (or null) points, which are characteristic of OAM antennas and represent directions where the antenna's radiation is inherently minimized.

For Port 1's gain as a function of the elevation angle (θ), Figure 4.8(b) indicates that the antenna radiates most strongly at around 0°, where the gain reaches up to 5 dBi. As the elevation angle moves away from 0°, either towards $-90°$ or 90°, the gain gradually decreases, reaching a minimum of about -5 dBi. There is a noticeable dip in gain around $-20°$, which is another singularity point, characteristic to OAM antennas, suggesting reduced radiation efficiency at that specific angle. These variations in gain with angle, including the presence of singularity points, highlight the antenna's directional characteristics, which are essential for optimizing its performance in specific applications.

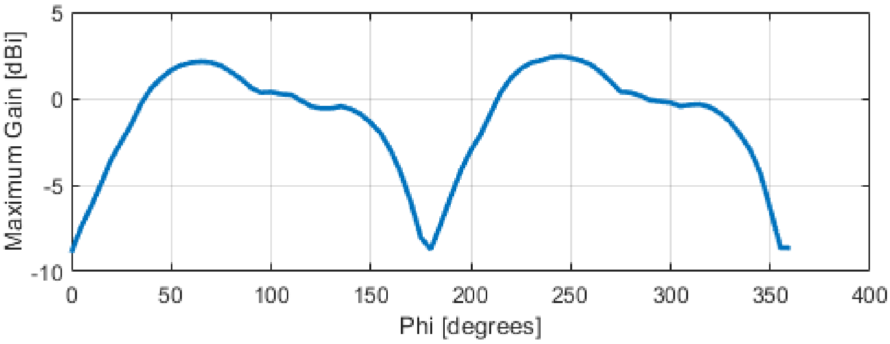

(a) Maximum gain vs. phi

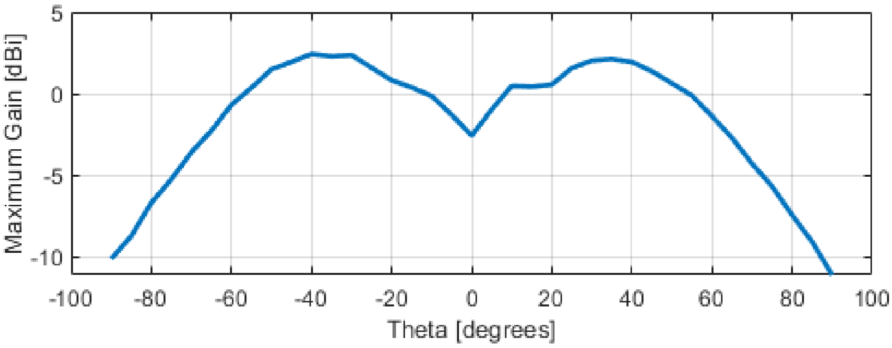

(b) Maximum gain vs. theta

Figure 4.9 Maximum gain vs. angle for Port 2

For Port 2, similar behavior is observed for both the azimuthal and elevation angles with minimum and maximum gain values for different angle values in Figure 4.9.

Figure 4.10 illustrates the return loss (RL) change of the OAM antenna with linear polarization according to frequency. As RL measures how much power is reflected back from the antenna, the least power is reflected back towards the source around 7 GHz, and the best performance is obtained. The S11 value is measured as -24.95 dB at 6.92 GHz, while S22 is -32.13 dB at 6.96 GHz, both indicating good impedance matching at their respective ports and frequencies. These findings expose the reflected power of 0.32% for P1 and only 0.06% for P2. This reflects a good impedance match, leading to nearly all the power transmission or reception through this port, minimizing loss.

Figure 4.11 shows that when P1 is excited, the phase pattern of linearly polarized OAM antenna rotates in a clockwise (CW) direction, while when P2 is excited, the phase pattern rotates in the reverse direction, which is counter-clockwise (CCW).

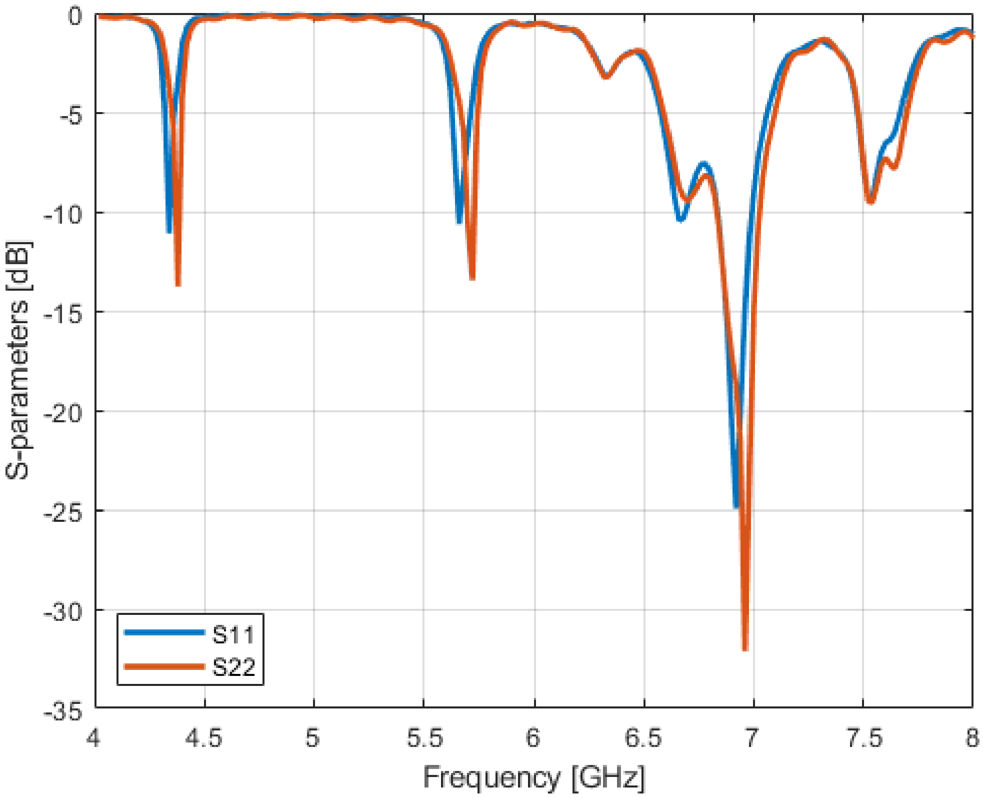

Figure 4.10 S-parameters vs. frequency for OAM with linear polarization

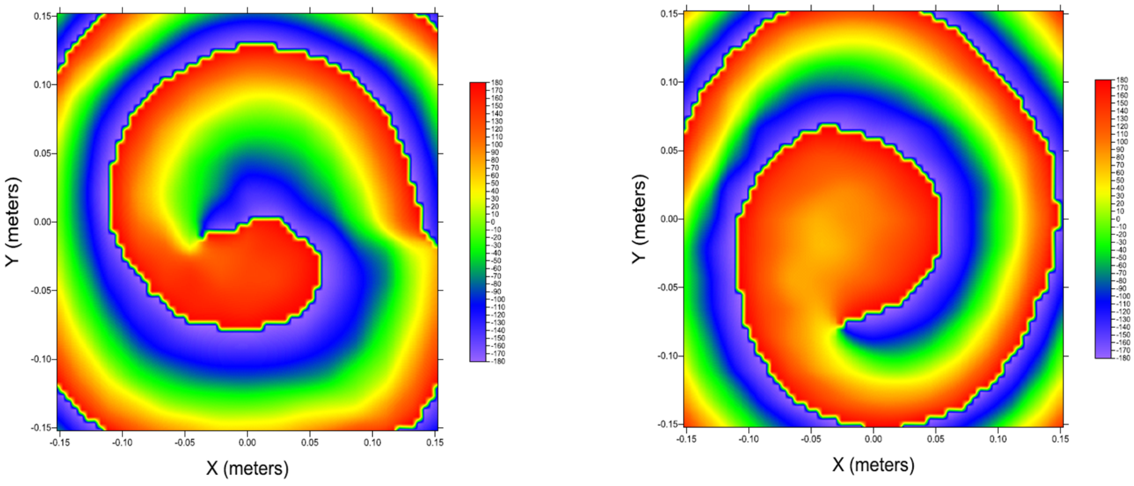

(a) Port 1

(b) Port 2

Figure 4.11 Phase patterns for OAM antenna with linear polarization

Measurements were conducted for the frequencies in 6.25 and 7.25 GHz interval and the radiation patterns for the linear polarized UCA antenna were investigated for the 11 distinct frequency values. It was observed that OAM modes are not generated in every frequency in this frequency interval. The best OAM generation occurs at 6.75 GHz and 6.85 GHz; acceptable results were also obtained at 6.65 GHz and 6.95 GHz. Thus, only the results of these four frequencies out of 11 are provided and discussed for radiation pattern analysis, as OAM modes are not generated successfully in the remaining frequencies.

The 3D radiation patterns at 6.65, 6.75, 6.85 and 6.95 GHz frequencies for OAM antenna with linear polarization for different ports and polarizations are shown in Figures 4.12, 4.13, 4.14 and 4.15. In these figures, as it could be noticed, the patterns show different orientations and null points for distinct ports and polarizations. While red regions show high radiation intensity, there exist cyan points that correspond to low radiation points (null or singularity). The radiation patterns exhibit areas of high intensity (red) and null points or singularities (blue). At 6.75 GHz, the null points are in the vicinity of the center, similar to what is observed in HFSS simulation, while for the other frequencies, they are more distributed. Generally, the number of null points increases, and they become more apparent as the frequency increases from 6.65 GHz to 6.95 GHz. At 6.95 GHz, multiple singularities occur and spread.

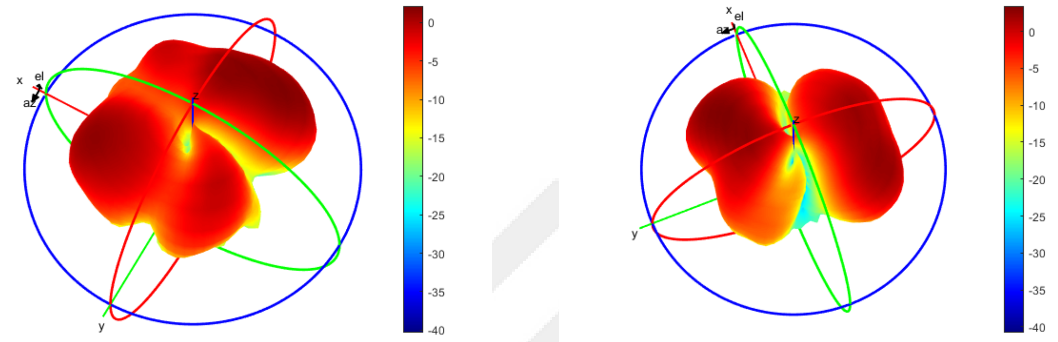

(a) Port 1 Pol 1 (b) Port 1 Pol 2

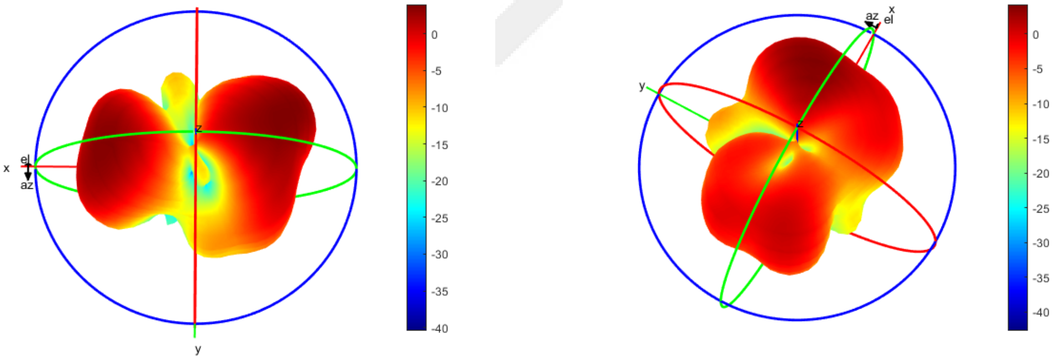

(c) Port 2 Pol 1 (d) Port 2 Pol 2

Figure 4.12 3D radiation patterns of OAM antenna with linear polarization at 6.65 GHz

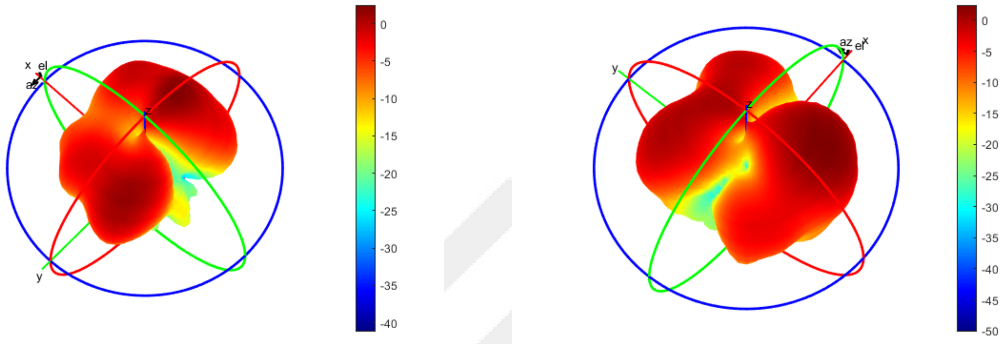

(a) Port 1 Pol 1 (b) Port 1 Pol 2

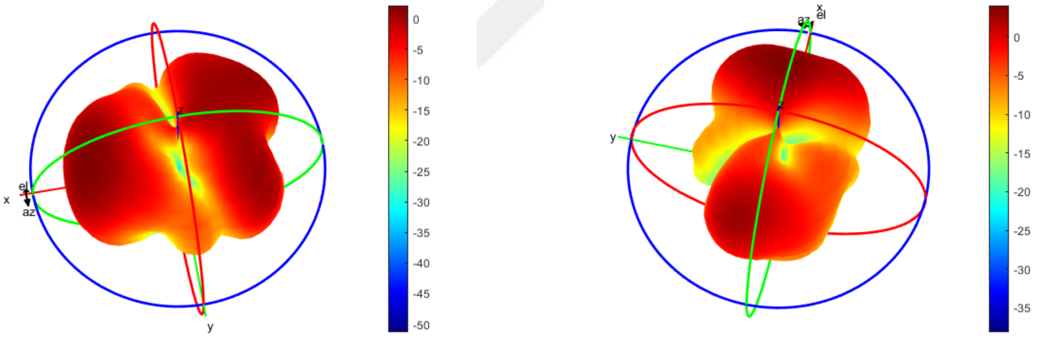

(c) Port 2 Pol 1 (d) Port 2 Pol 2

Figure 4.13 3D radiation patterns of OAM antenna with linear polarization at 6.75 GHz

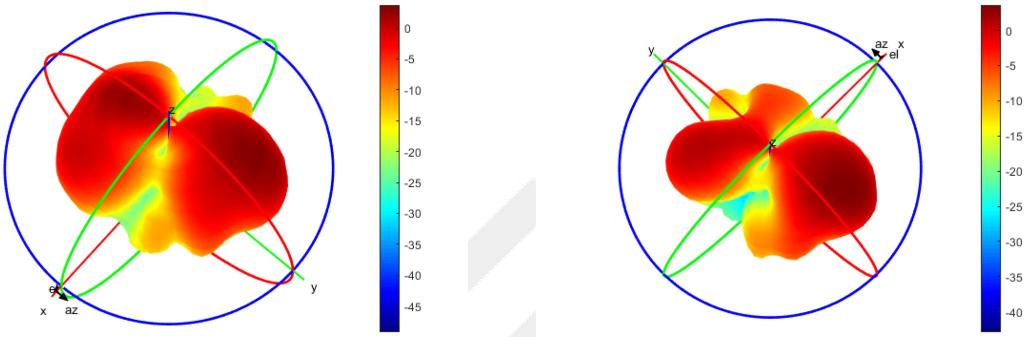

(a) Port 1 Pol 1 (b) Port 1 Pol 2

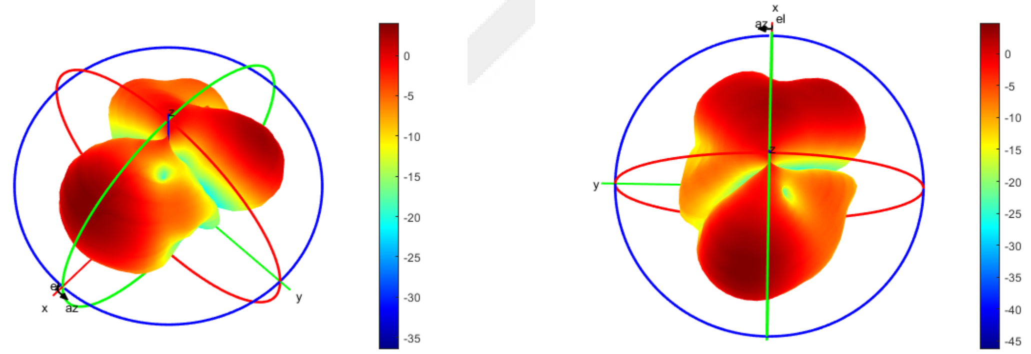

(c) Port 2 Pol 1 (d) Port 2 Pol 2

Figure 4.14 3D radiation patterns of OAM antenna with linear polarization at 6.85 GHz

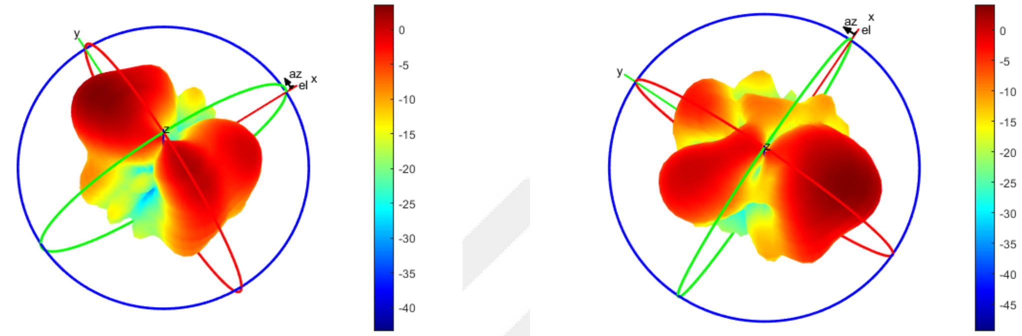

(a) Port 1 Pol 1 (b) Port 1 Pol 2

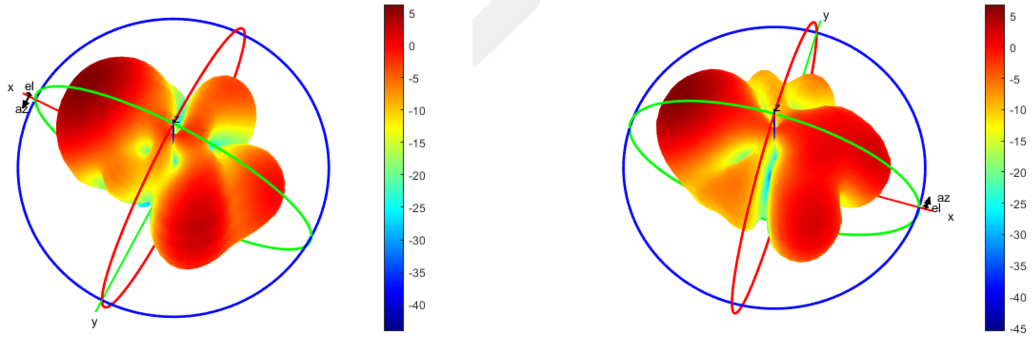

(c) Port 2 Pol 1 (d) Port 2 Pol 2

Figure 4.15 3D radiation patterns of OAM antenna with linear polarization at 6.95 GHz

Figures 4.16, 4.17, 4.18 and 4.19 illustrate the 3D radiation patterns projected to rectangular coordinates for an OAM antenna with linear polarization at 6.65, 6.75, 6.85 and 6.95 GHz respectively across different excited ports and polarizations. As a common property in all of these plots, the radiation patterns create high-intensity areas shown by red and null points (or singularities) shown by dark blue. The blue regions represent null points where the radiation intensity is minimal or zero, typically occurring due to phase cancellations or destructive interference at specific angles. These null points are inherent to the complex field distribution of OAM modes, where the phase structure can lead to localized areas of reduced radiation. From these plots, it was observed that the null points are symmetric around the origin. The ϕ angles that these singularities prominently occur in these plots were determined to take slices of 3D radiation patterns from those angles. The 2D radiation patterns, including results belonging to specific angles for different polarizations and excited ports, are obtained for the designated frequencies.

In Figures 4.20, 4.21, 4.22 and 4.23 the 2D radiation patterns of OAM antenna with linear polarization at 6.65, 6.75, 6.85 and 6.95 GHz for distinct polarizations and ports are presented. The radiation patterns are plotted for different ϕ angles depending on where the null points are located at the radiation pattern. Null points, where the radiation intensity is minimal or zero, are observed at specific angles where the patterns intersect the origin, indicating phase cancellations or destructive interference. These null points are visible in the dips of the polar plots. These nulls highlight the directional properties and angular dependence of the OAM antenna's radiation characteristics. Additionally, the different shapes of the radiation patterns for different ϕ angles demonstrate the anisotropic radiation behavior of the OAM antenna, which is crucial for applications requiring specific directional radiation properties and phase structures.

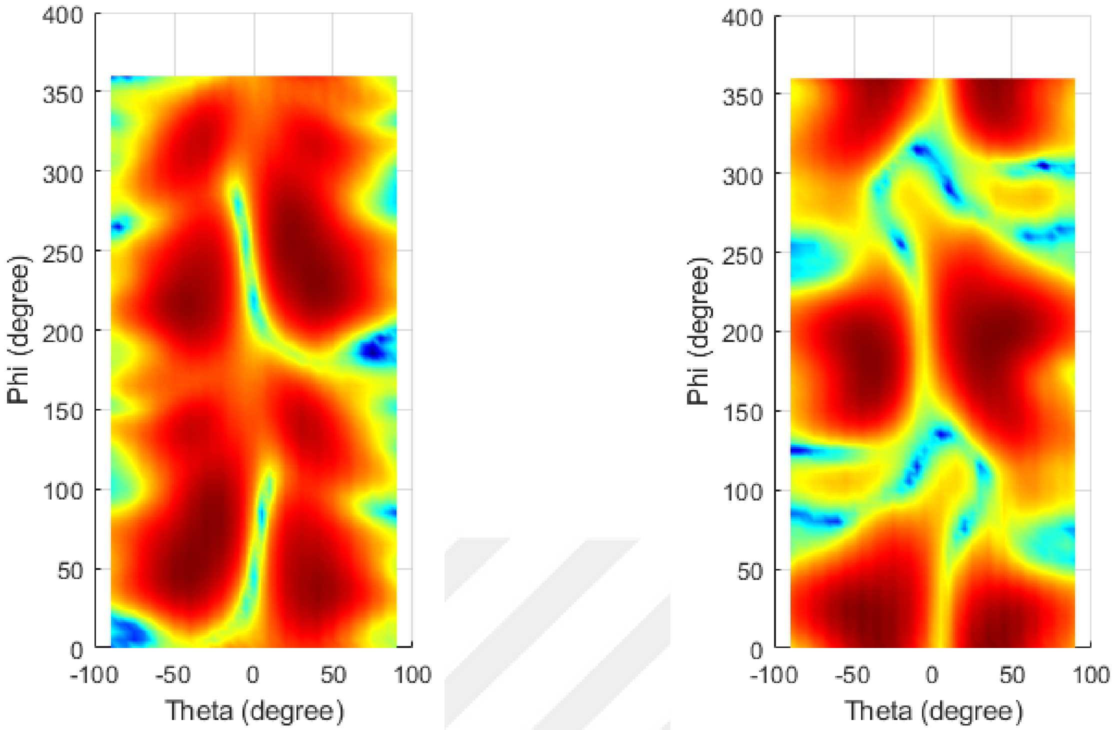

(a) Port 1 Pol 1 (b) Port 1 Pol 2

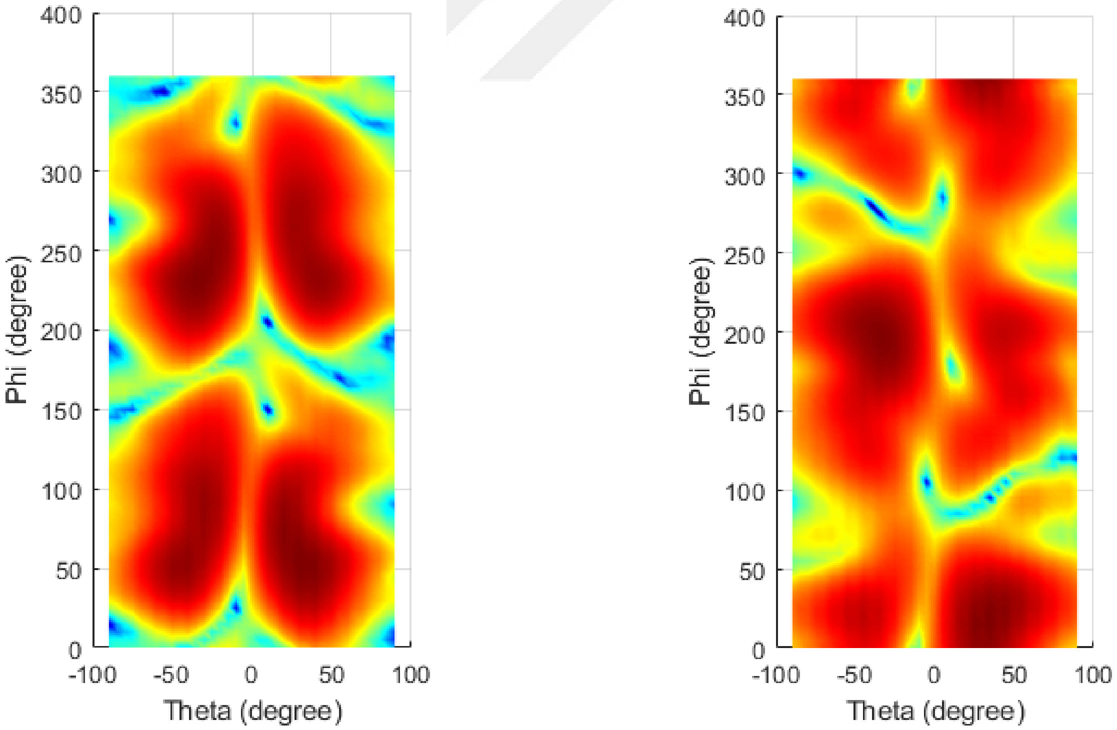

(c) Port 2 Pol 1 (d) Port 2 Pol 2

Figure 4.16 3D radiation patterns of OAM antenna with linear polarization at 6.65 GHz

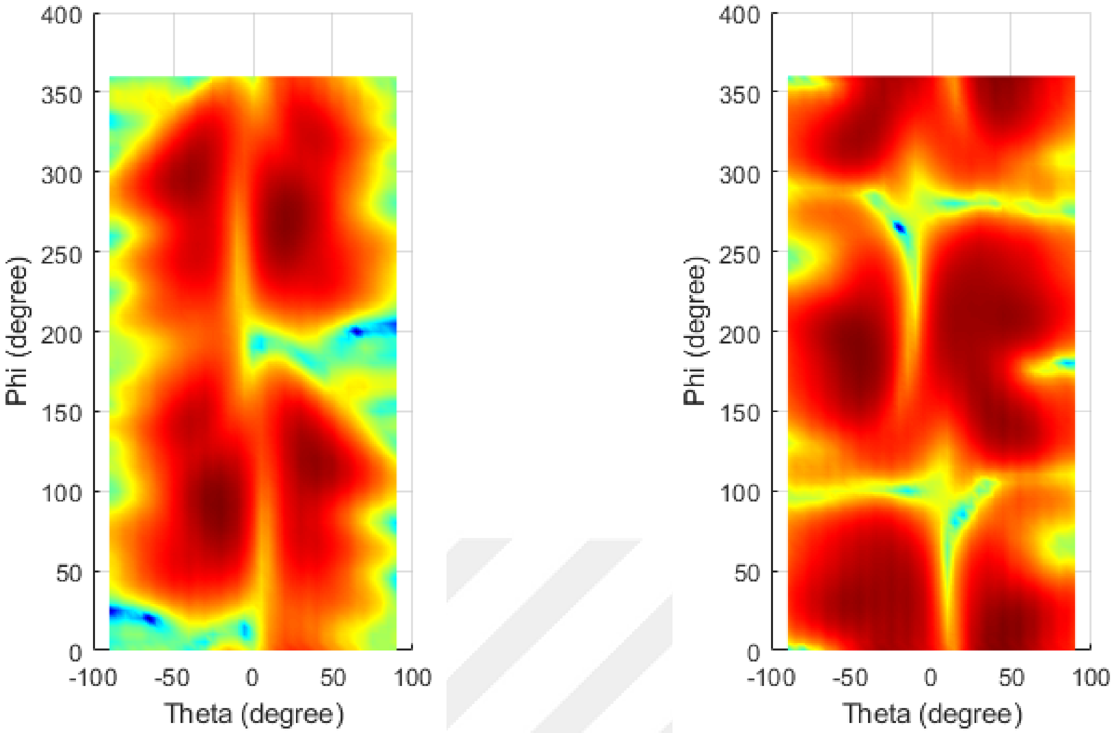

(a) Port 1 Pol 1 (b) Port 1 Pol 2

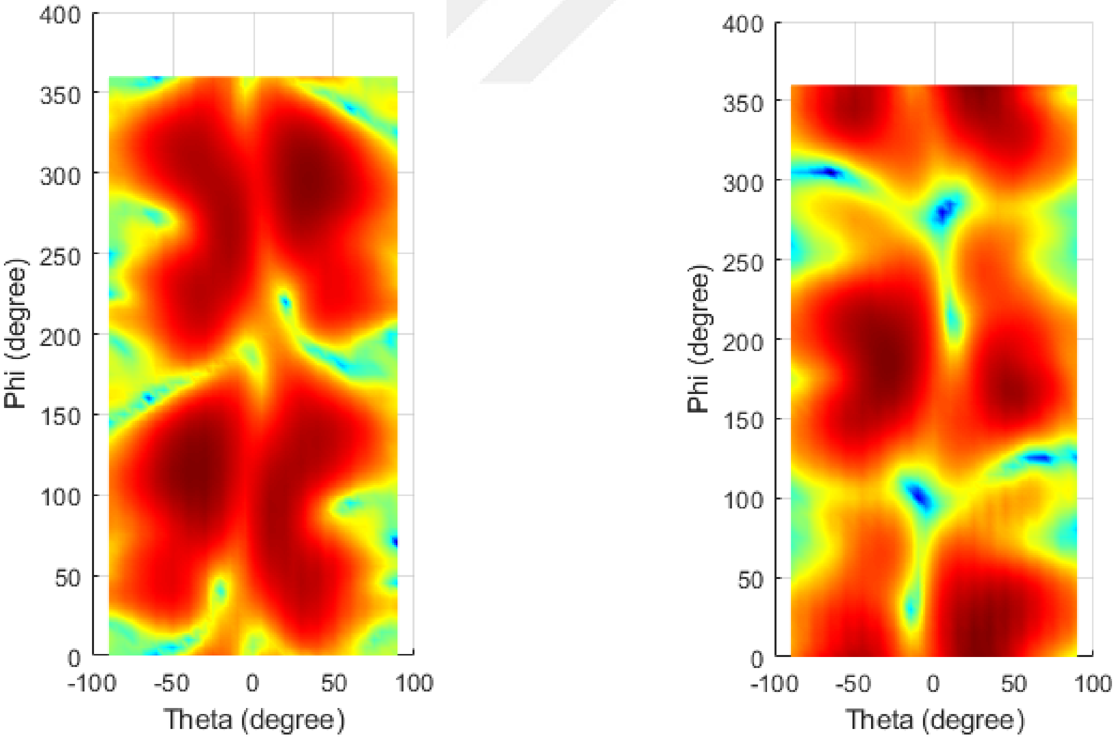

(c) Port 2 Pol 1 (d) Port 2 Pol 2

Figure 4.17 3D radiation patterns of OAM antenna with linear polarization at 6.75 GHz

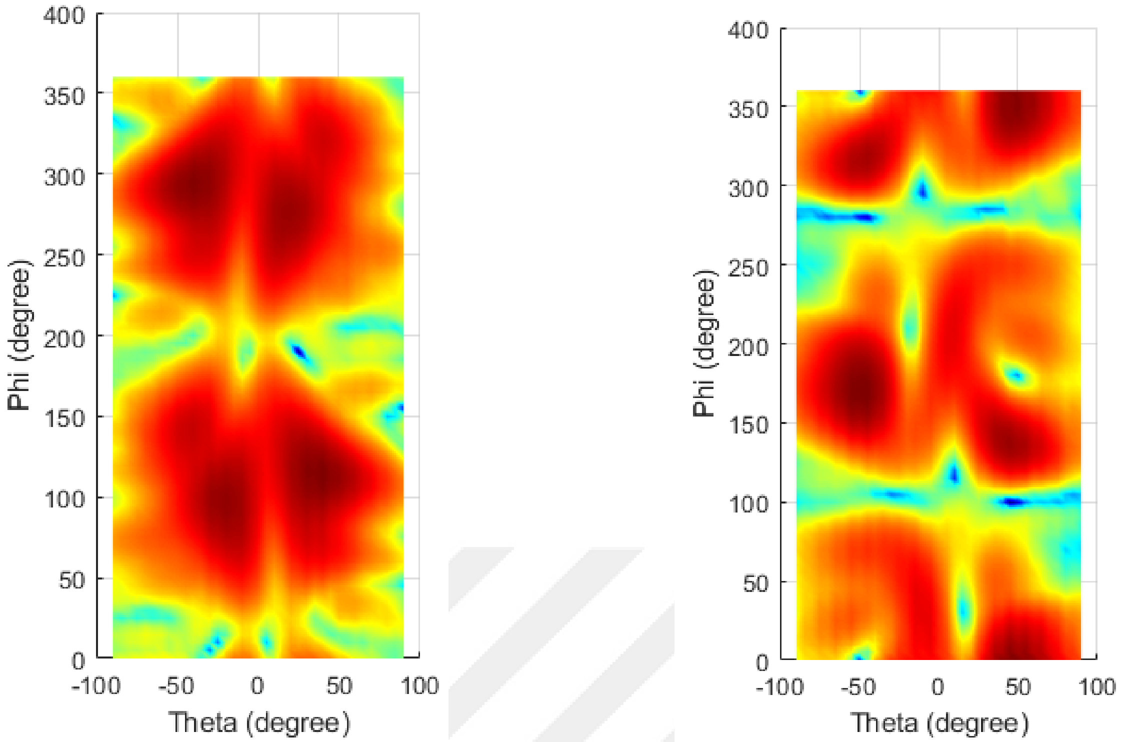

(a) Port 1 Pol 1 (b) Port 1 Pol 2

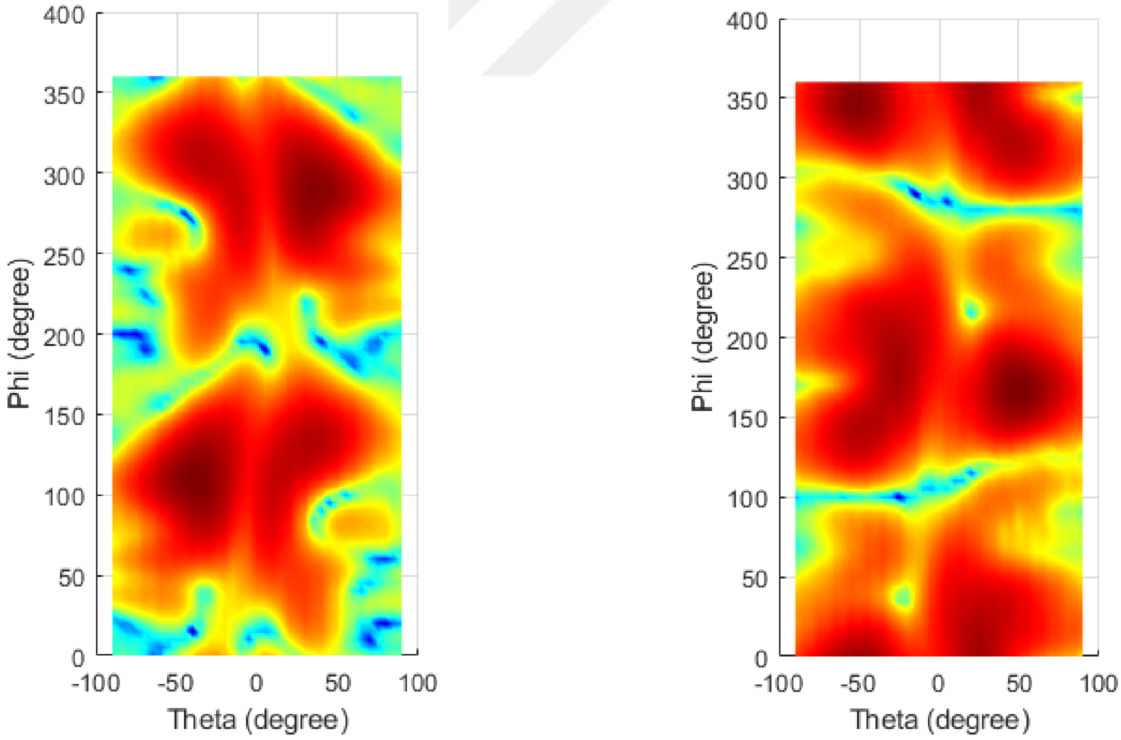

(c) Port 2 Pol 1 (d) Port 2 Pol 2

Figure 4.18 3D radiation patterns of OAM antenna with linear polarization at 6.85 GHz

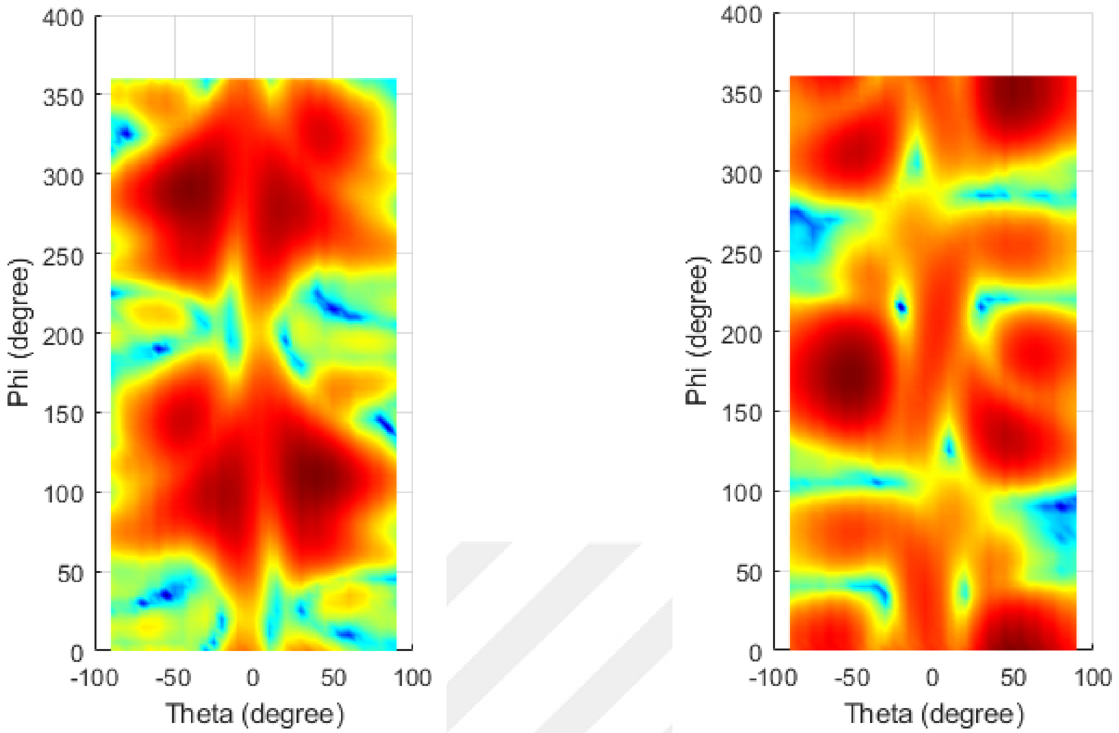

(a) Port 1 Pol 1 (b) Port 1 Pol 2

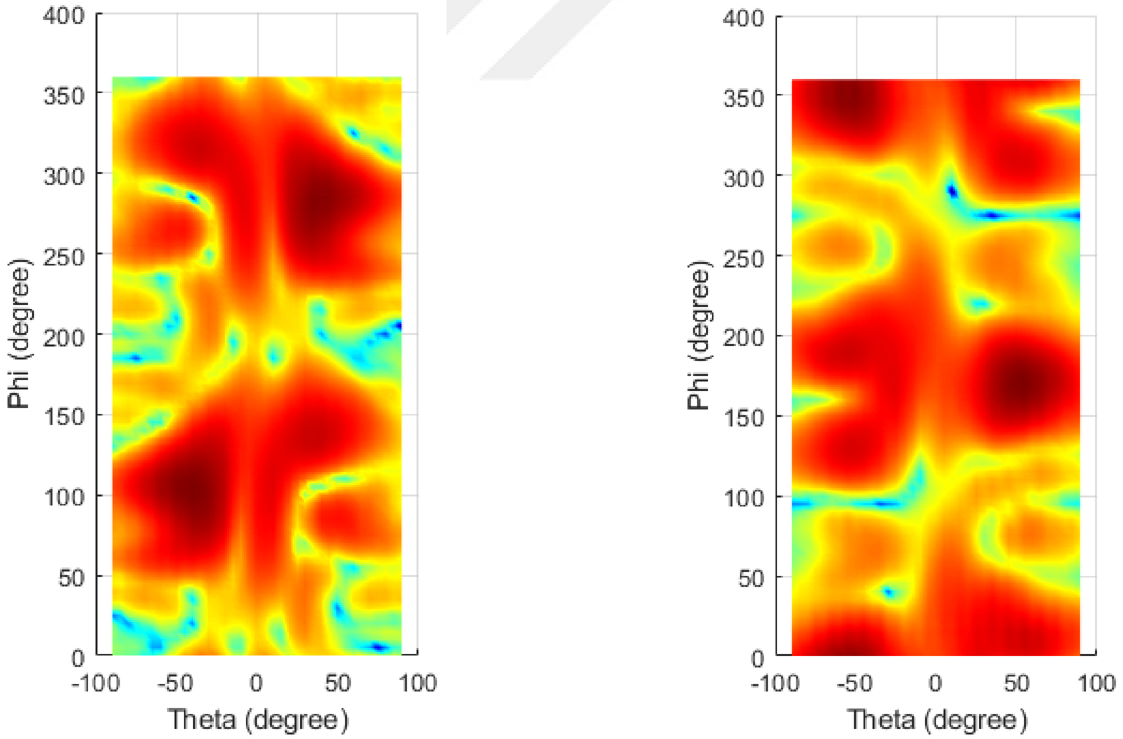

(c) Port 2 Pol 1 (d) Port 2 Pol 2

Figure 4.19 3D radiation patterns of OAM antenna with linear polarization at 6.95 GHz

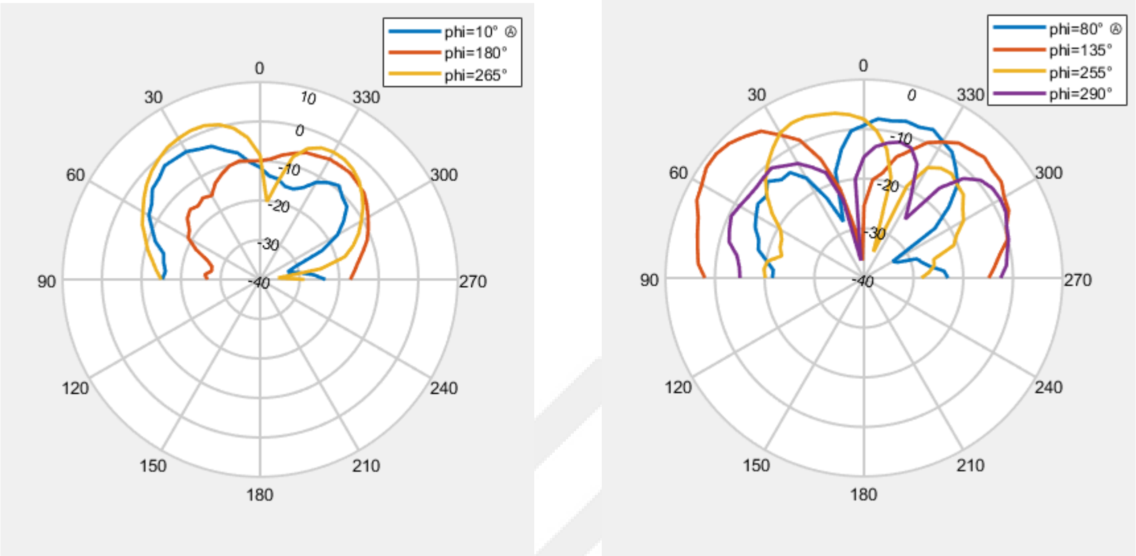

(a) Port 1 Pol 1

(b) Port 1 Pol 2

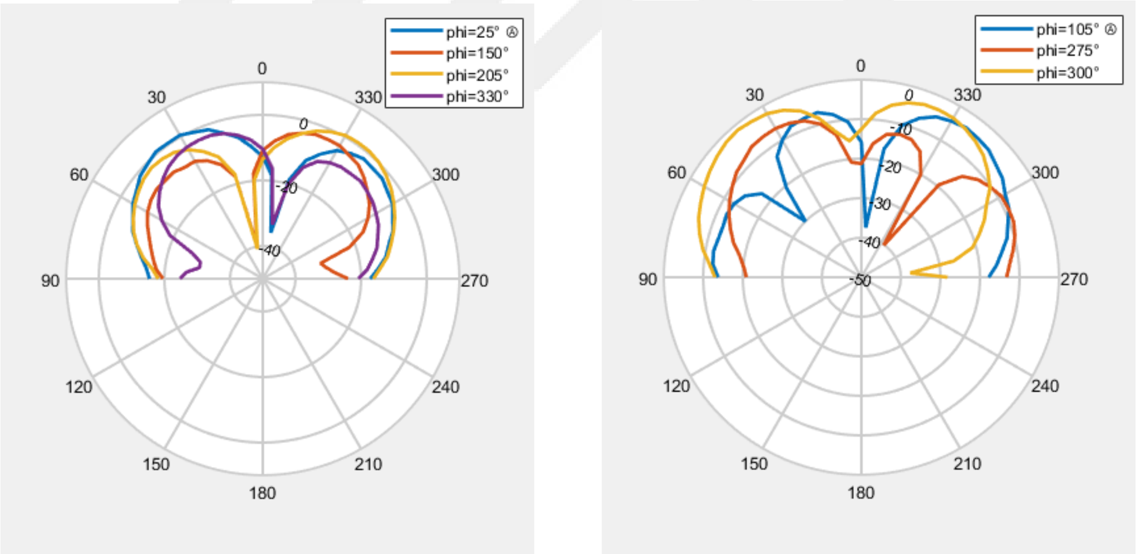

(c) Port 2 Pol 1

(d) Port 2 Pol 2

Figure 4.20 2D radiation patterns of OAM antenna with linear polarization at 6.65 GHz

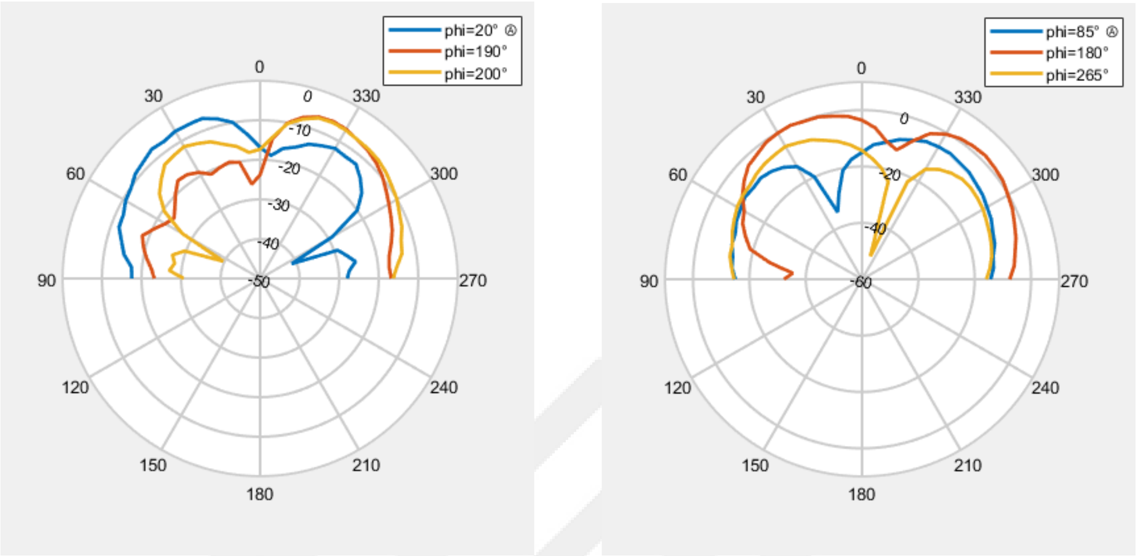

(a) Port 1 Pol 1 (b) Port 1 Pol 2

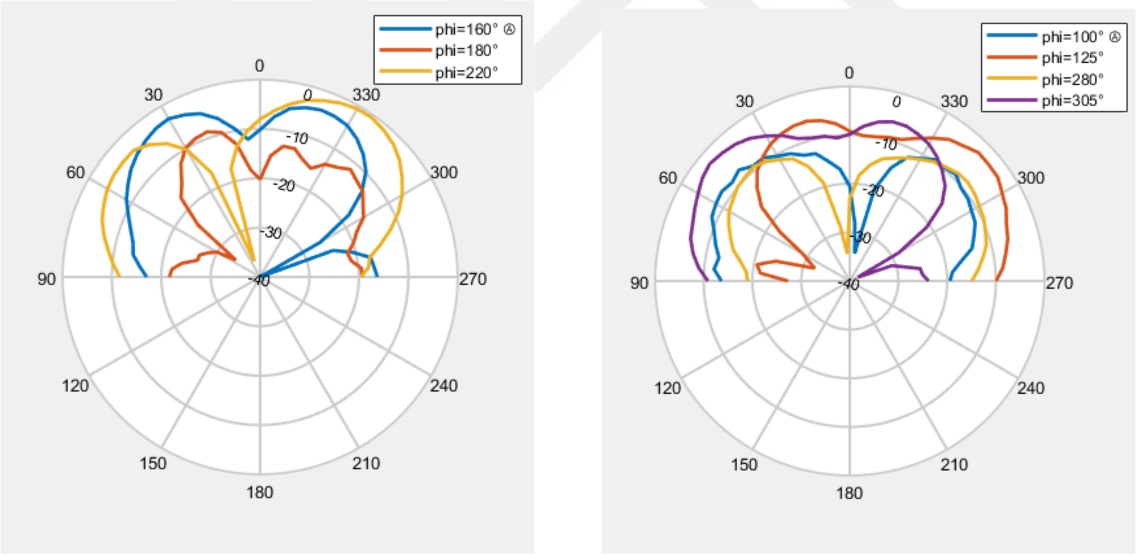

(c) Port 2 Pol 1 (d) Port 2 Pol 2

Figure 4.21 2D radiation patterns of OAM antenna with linear polarization at 6.75 GHz

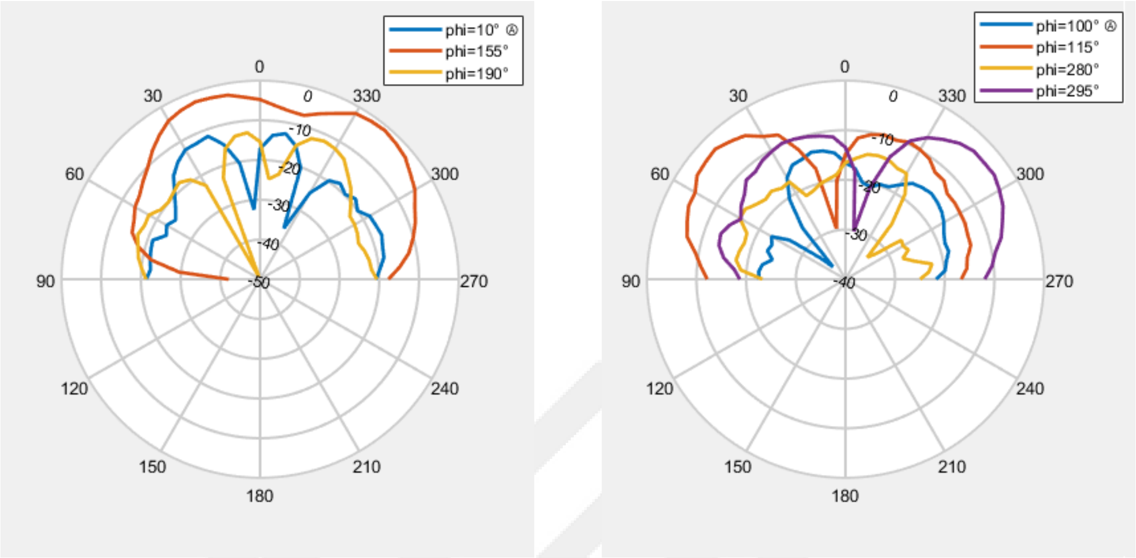

(a) Port 1 Pol 1

(b) Port 1 Pol 2

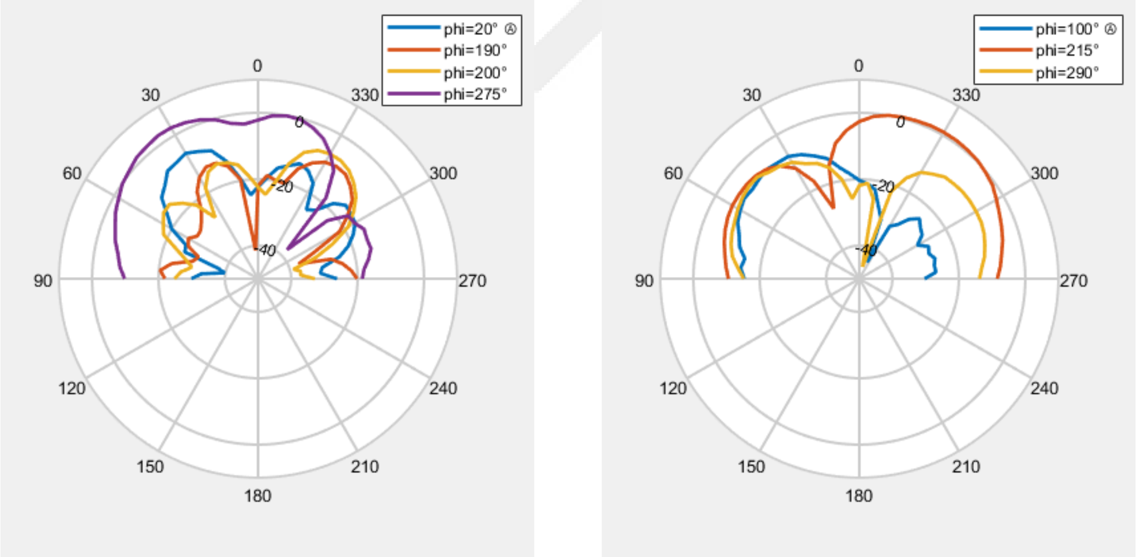

(c) Port 2 Pol 1

(d) Port 2 Pol 2

Figure 4.22 2D radiation patterns of OAM antenna with linear polarization at 6.85 GHz

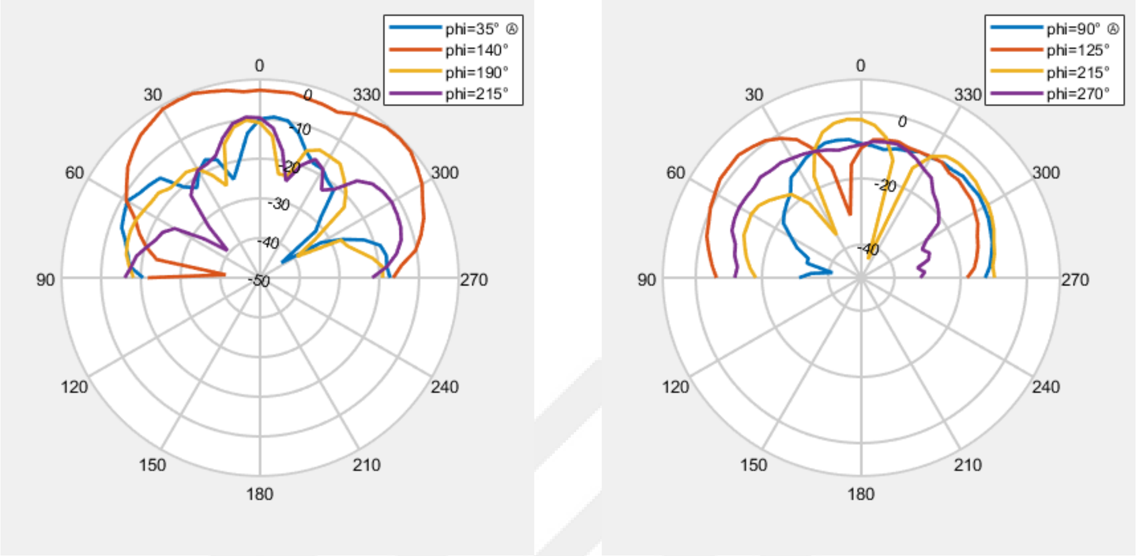

(a) Port 1 Pol 1

(b) Port 1 Pol 2

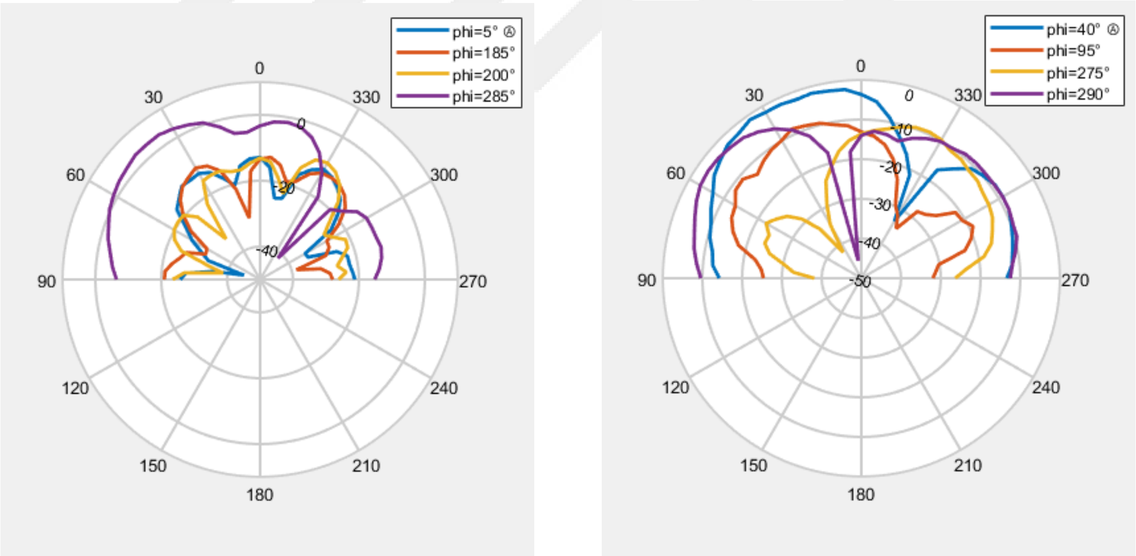

(c) Port 2 Pol 1

(d) Pol 2 Port 2

Figure 4.23 2D radiation patterns of OAM antenna with linear polarization at 6.95 GHz

4.3.2 OAM Antenna with Circular Polarization

In this section, the measurement results of OAM antenna with circular polarization are shown. In Figure 4.24, normalized gain vs. frequency plots are shown for P1 and P2 in (a) and (b) parts respectively. P1 exhibits its highest gain around 0 dBic at 7 GHz while it significantly falls down below -20 dBic at 6.25 GHz. Likewise, P2 shows high gain of 1.21 dBic between 6.85 GHz and 6.95 GHz and lowest gain of -17.1 dBic at 6.55 GHz. This indicates that the antenna's gain and herewith efficiency is dependent on the operating frequency and better performances are obtained in 6.85 GHz to 7 GHz band.

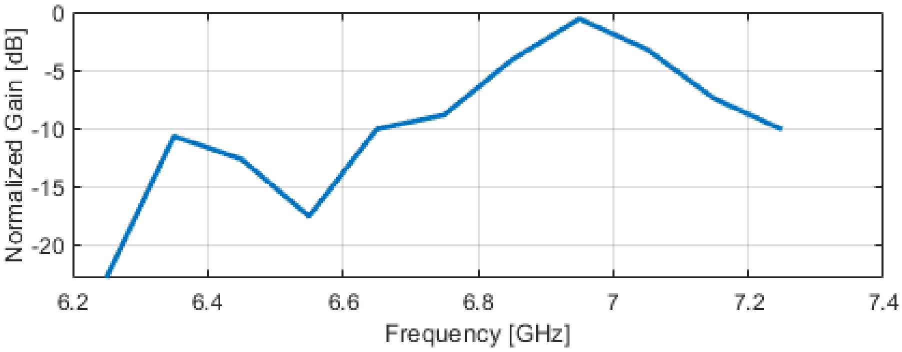

(a) Port 1

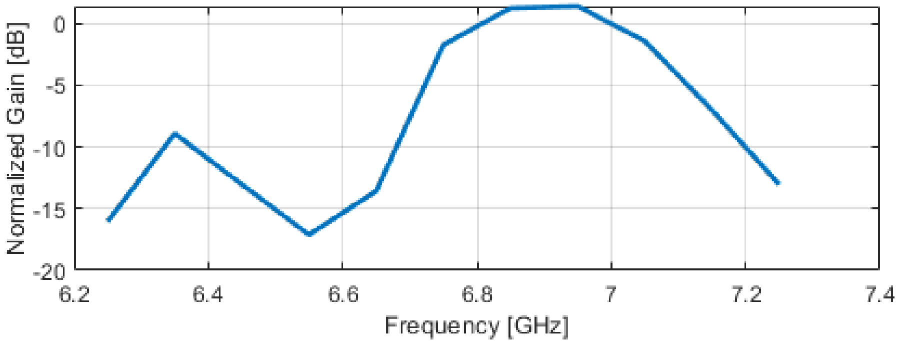

(b) Port 2

Figure 4.24 Normalized gain vs. frequency for OAM antenna with circular polarization

In Figures 4.25 and 4.26, maximum gain vs. angle plots for Port 1 and 2 are shown respectively. Figure 4.25(a) shows how the antenna's gain varies with the azimuthal angle (ϕ) from 0° to 360°. Same as in linear polarization case, the gain pattern is periodic, with peaks around 100° and 270° where the gain reaches approximately 2 dBic. However, the gain drops significantly near 160° and 340° indicating weaker radiation in those directions, with the gain close to 0 dBic. The maximum gain vs. elevation angle (θ) for P1 can be seen in the (b) part of the same figure. For $\theta = \pm 20°$, the maximum gain reaches to its peak value with is approximately 3 dBic.

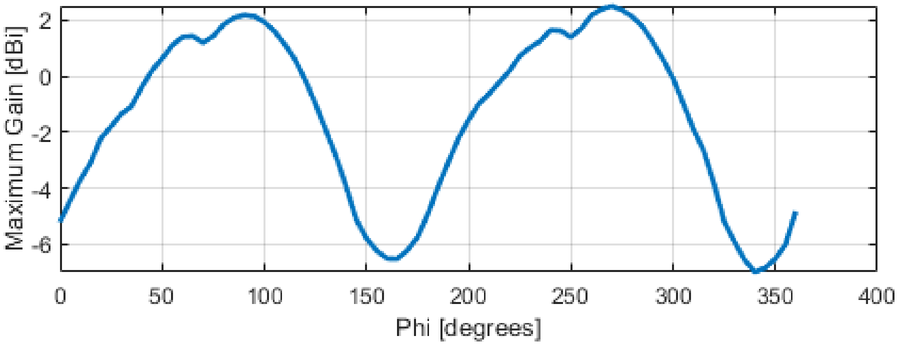

(a) Maximum gain vs. phi

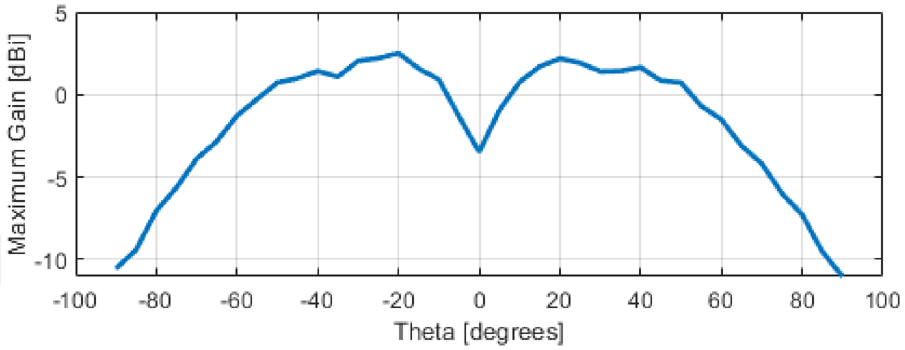

(b) Maximum gain vs. theta

Figure 4.25 Maximum gain vs. angle for Port 1

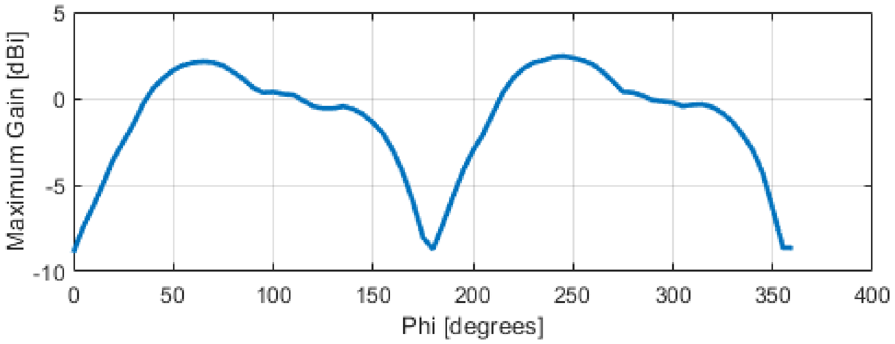

(a) Maximum gain vs. phi

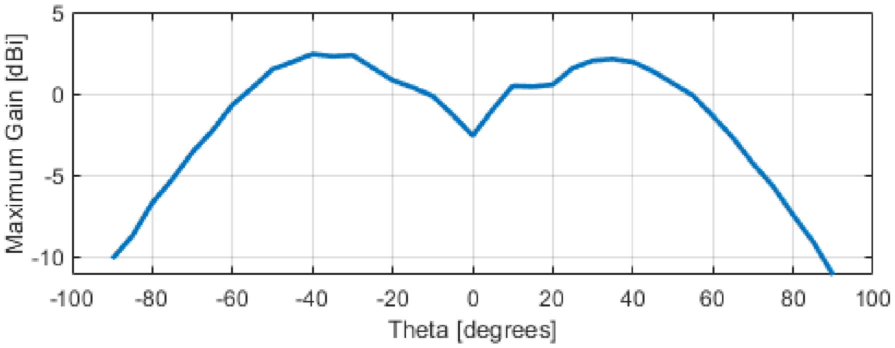

(b) Maximum gain vs. theta

Figure 4.26 Maximum gain vs. angle for Port 2

For P2, a similar behaviour is observed for both of the azimuthal and elevation angles with minimum and maximum gain values for different angle values in Figure 4.26. Figure 4.26(a) displays that the maximum gain is repeats itself with a 180° degree periods. In part (b) of the same figure, the maximum gain shows a symmetric behavior around $\theta = 180°$ and attaims its maximum for $\theta = \pm 40°$.

Figure 4.27 illustrates the return loss (RL) vs. frequency of OAM antenna with circular polarization for P1 and P2. From this figure, it can be interpreted that the least power is reflected back towards the source at 7 GHz. The S11 value is measured as -14.07 dB at 7 GHz, while S22 is -18.88 dB at again 7 GHz, which means reflected power of 3.91% for P1 and only 1.3% for P2. The second port has a lower reflection compared to the first port, indicating more efficient power transfer and slightly better performance. The s-parameter results are worse than the linear polarized antenna but still acceptable.

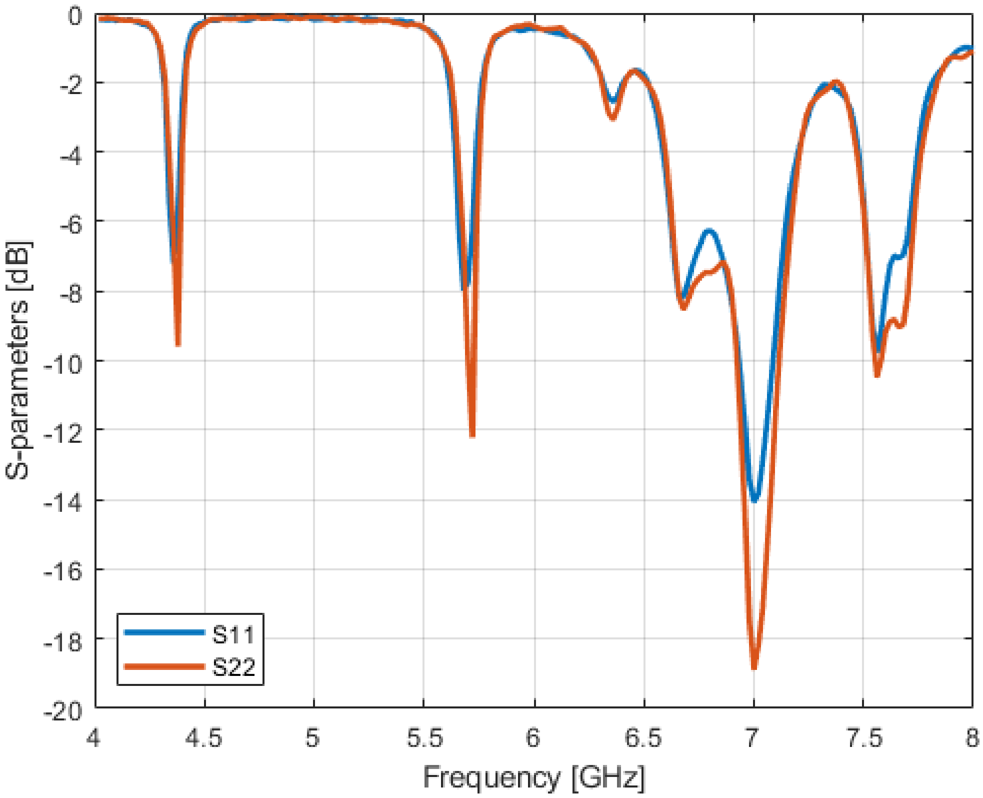

Figure 4.27 S-parameters vs. frequency for OAM with circular polarization

From Figure 4.28, it can be observed that the phase pattern rotates as expected from an OAM wave-generating antenna. As in the linear polarization case, when different ports are excited, the direction of rotation in the phase pattern is reversed. This situation occurs as the phases of the array elements in the same feeding order increase or decrease with identical amounts depending on the port excited. When P1 is excited for the OAM antenna with circular polarization, the phase pattern rotates in the CW direction. In contrast, when P2 is excited, the phase pattern rotates in the CCW direction for both polarizations. As distinct from the previous case, the phase pattern rotates in the same direction for both polarizations of the same port.

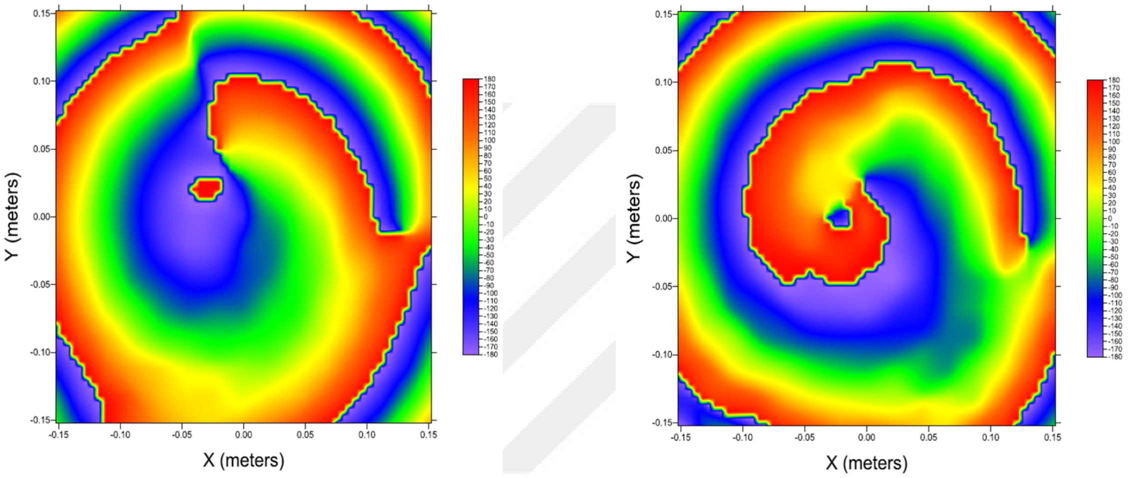

(a) Port 1 Pol 1

(b) Port 1 Pol 2

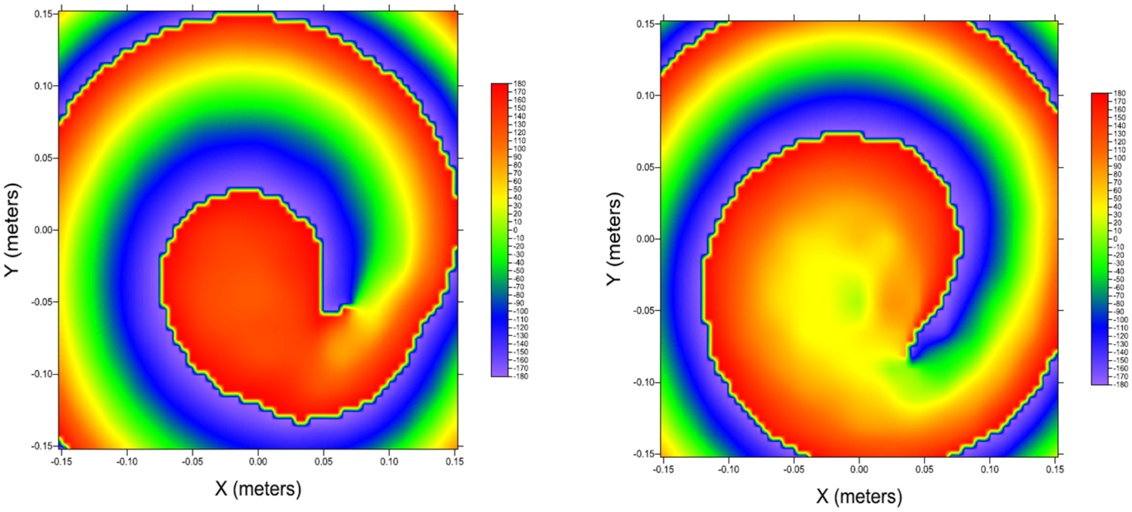

(c) Port 2 Pol 1

(d) Port 2 Pol 2

Figure 4.28 Phase patterns for OAM antenna with circular polarization

For circularly polarized antenna, the same measurements were conducted as linear polarization. OAM mode observability were similar with the previous case, thus the radiation pattern results for 6.65 GHz, 6.75 GHz, 6.85 GHz and 6.95 GHz are given and analysis made on these frequencies.

The 3D radiation patterns at 6.65 GHz, 6.75 GHz, 6.85 GHz and 6.95 GHz frequencies for OAM antenna with circular polarization for different ports and polarizations are shown in Figures 4.29, 4.30, 4.31 and 4.32. Similar behaviors in radiation patterns are observed when compared to the linearly polarized OAM antenna in the previous section. Null points (or singularities) are observed in the vicinity of the center in the radiation pattern, where the radiation is minimal or zero as an indicator of OAM generation. These singularities are best observed at 6.75 and 6.85 GHz, while the singularities are corrupted for frequencies 6.95 GHz and above. For lower frequencies than 6.75 GHz, the OAM wave is not generated properly, and singularities do not occur as expected. Compared to the linear polarization, at 6.75 GHz, the singularities got closer to the center and became larger.

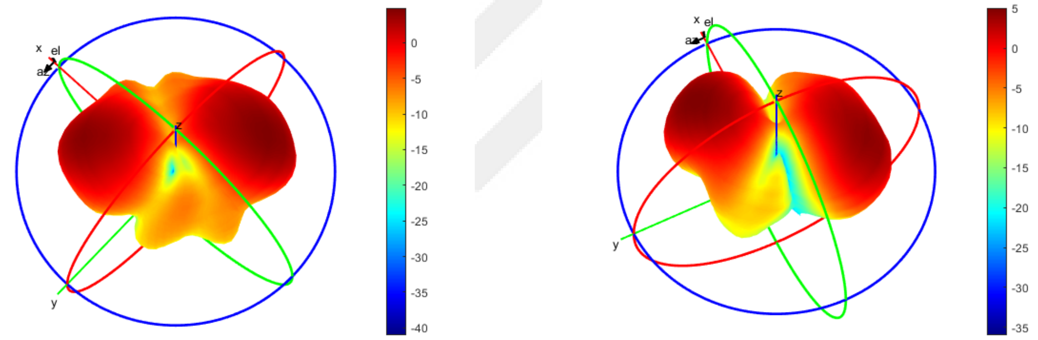

(a) Port 1 Pol 1 (b) Port 1 Pol 2

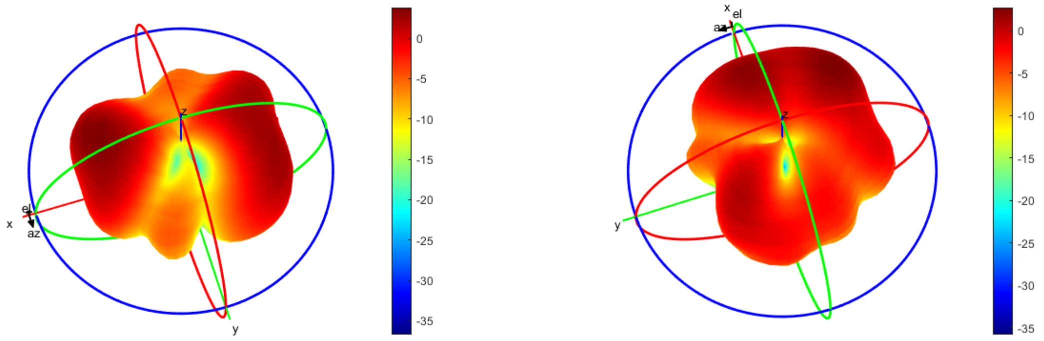

(c) Port 2 Pol 1 (d) Port 2 Pol 2

Figure 4.29 3D radiation patterns of OAM antenna with circular polarization at 6.65 GHz

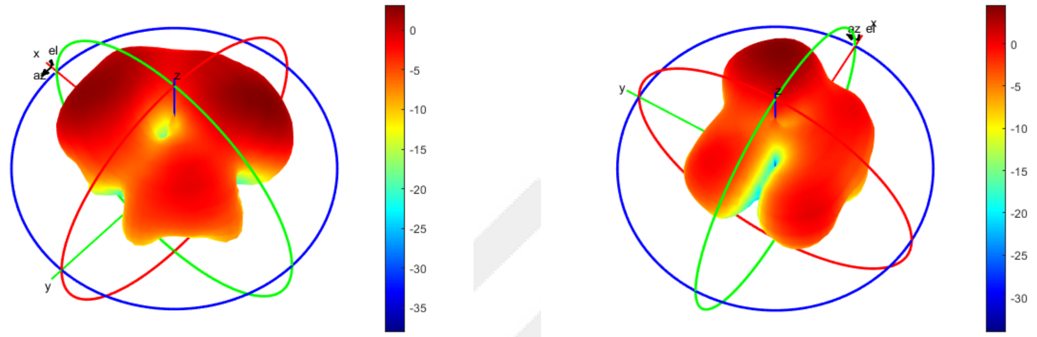

(a) Port 1 Pol 1 (b) Port 1 Pol 2

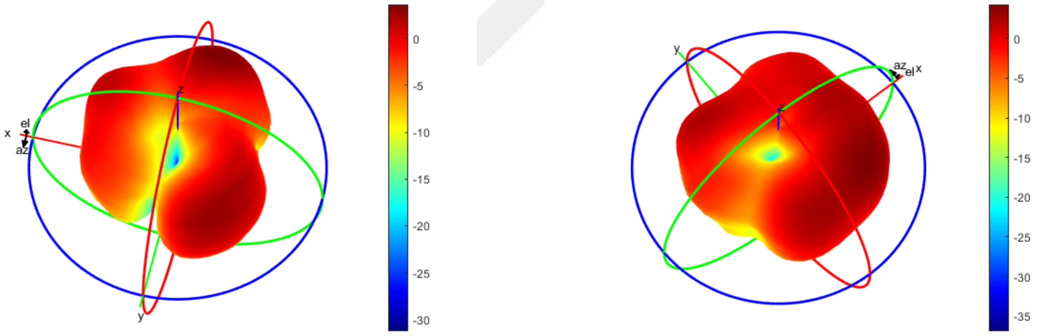

(c) Port 2 Pol 1 (d) Port 2 Pol 2

Figure 4.30 3D radiation patterns of OAM antenna with circular polarization at 6.75 GHz

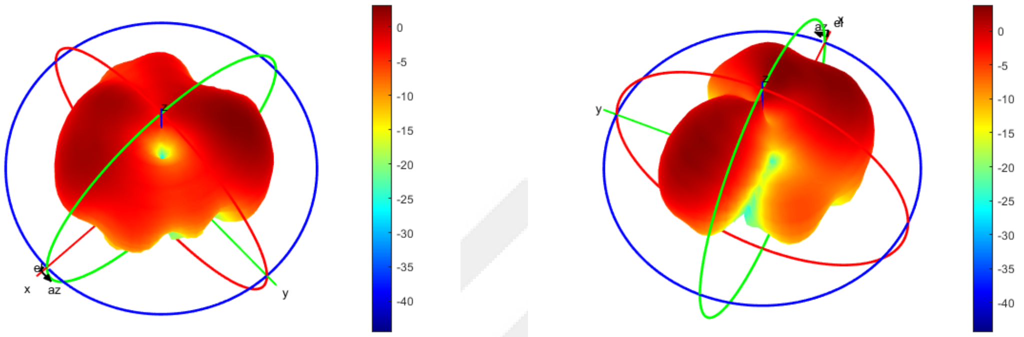

(a) Port 1 Pol 1 (b) Port 1 Pol 2

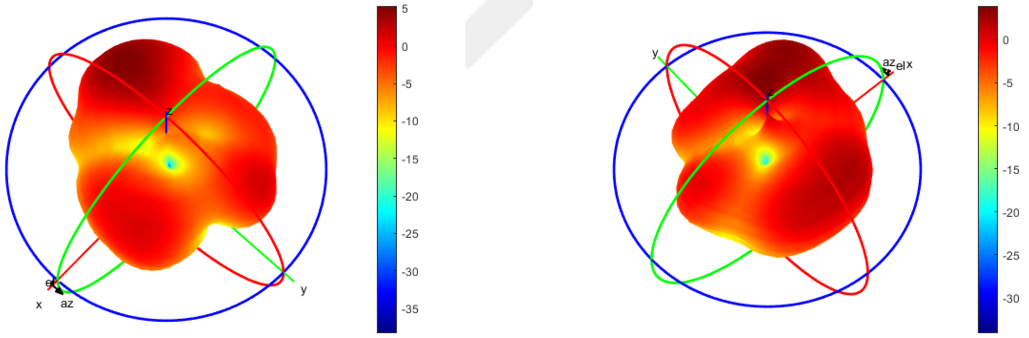

(c) Port 2 Pol 1 (d) Port 2 Pol 2

Figure 4.31 3D radiation patterns of OAM antenna with circular polarization at 6.85 GHz

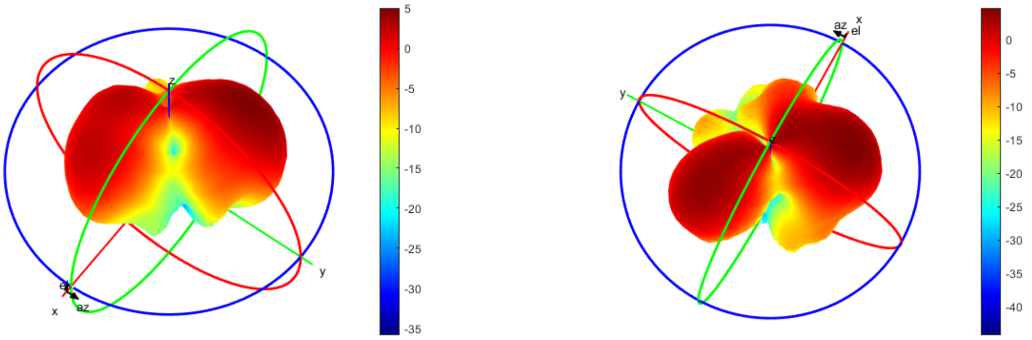

(a) Port 1 Pol 1

(b) Port 1 Pol 2

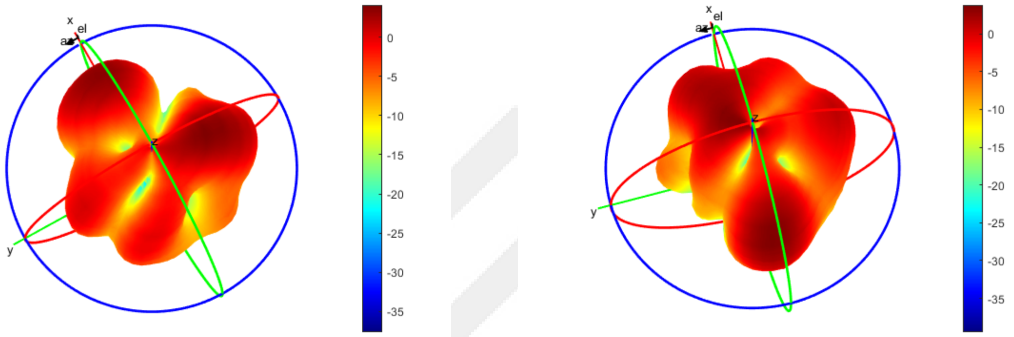

(c) Port 2 Pol 1

(d) Port 2 Pol 2

Figure 4.32 3D radiation patterns of OAM antenna with circular polarization at 6.95 GHz

In figures 4.33, 4.34, 4.35 and 4.36, these radiation patterns projected to rectangular coordinates for the same frequencies. The singularities are more apparent in these figures, where null points appear in dark blue regions and red regions show the areas with high radiation intensity. In these figures, the singularities appear symmetrically around the center ($\phi = 180°$ and $\theta = 0°$) as in the linear polarization case, and the null points become deeper and more remarkable compared to the linear polarization case.

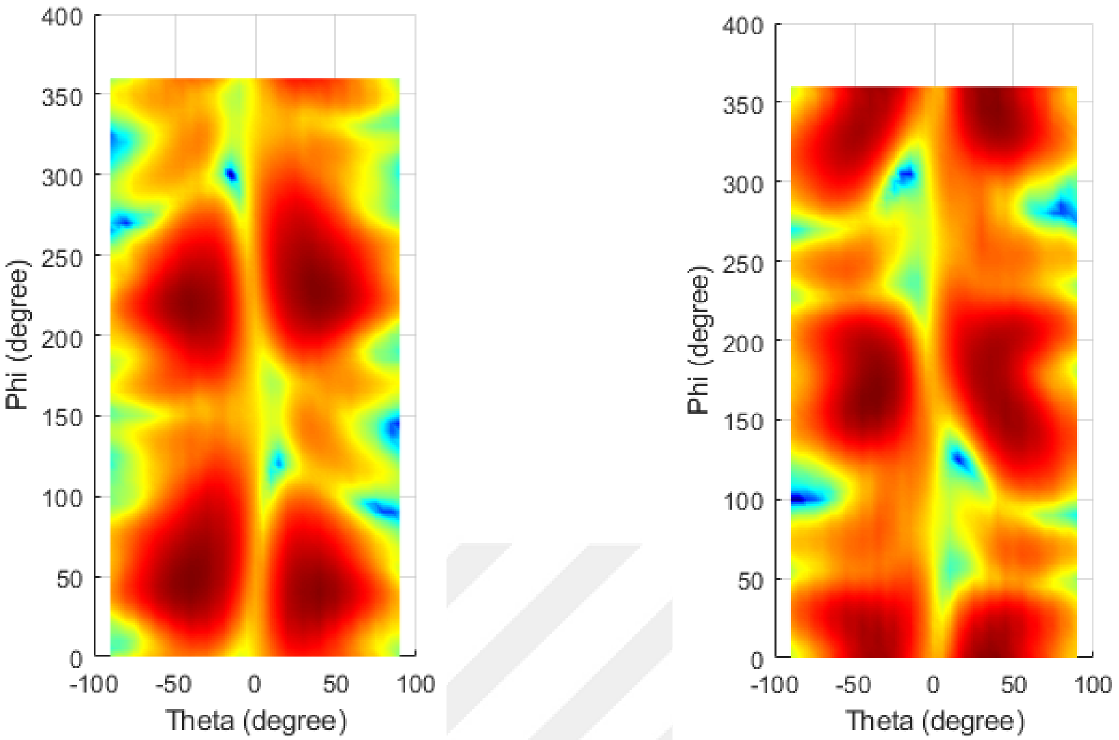

(a) Port 1 Pol 1 (b) Port 1 Pol 2

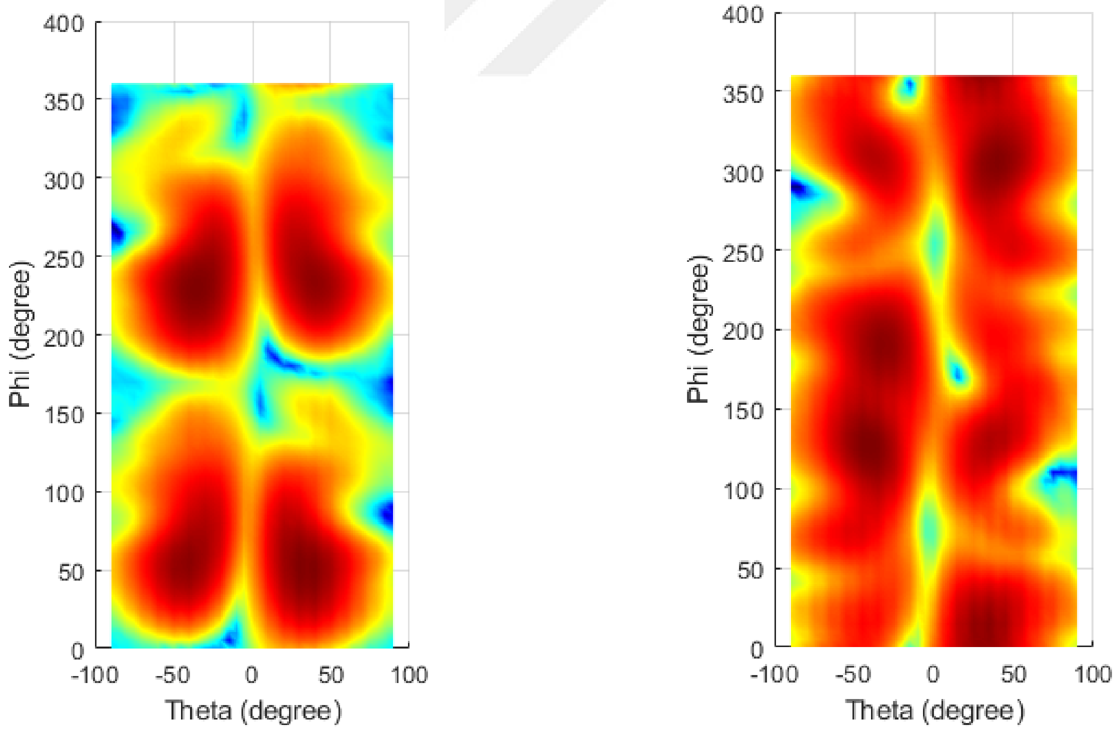

(c) Port 2 Pol 1 (d) Port 2 Pol 2

Figure 4.33 3D radiation patterns of OAM antenna with circular polarization at 6.65 GHz

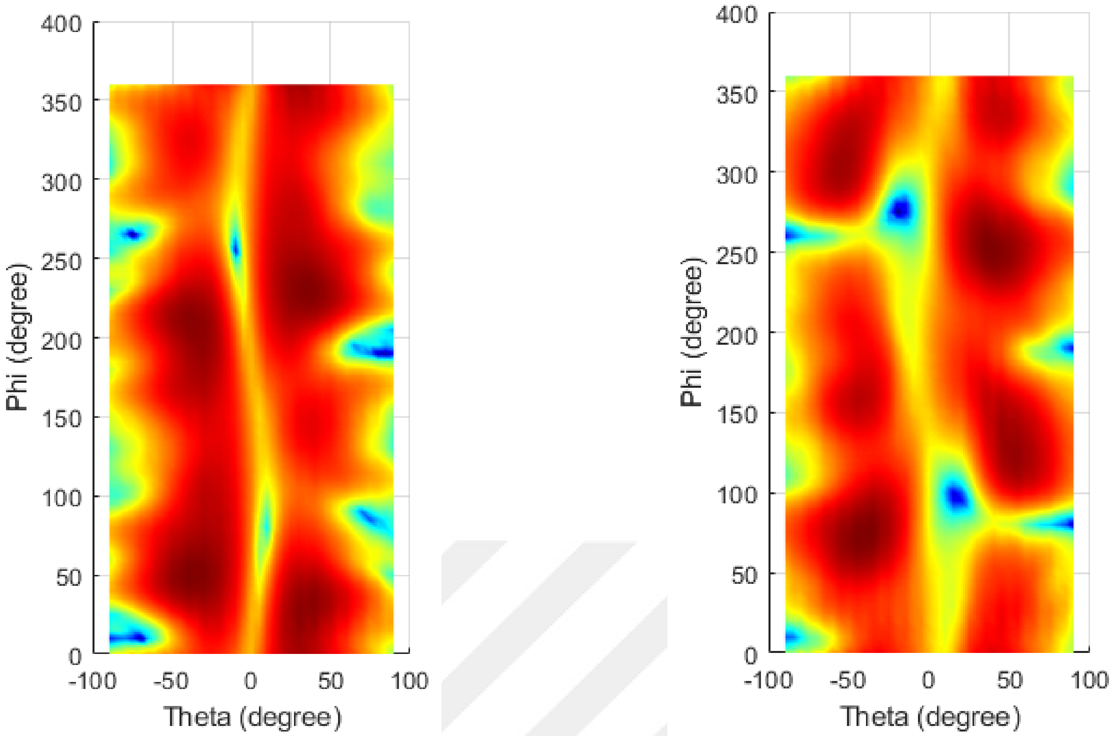

(a) Port 1 Pol 1 (b) Port 1 Pol 2

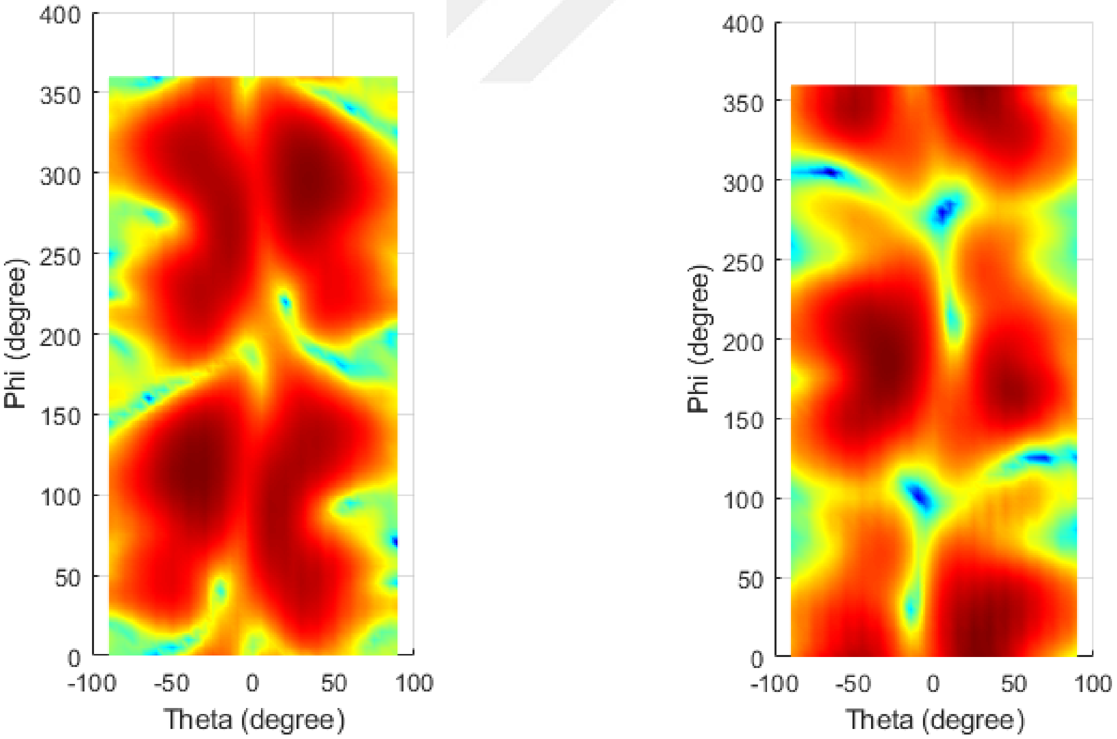

(c) Port 2 Pol 1 (d) Port 2 Pol 2

Figure 4.34 3D radiation patterns of OAM antenna with circular polarization at 6.75 GHz

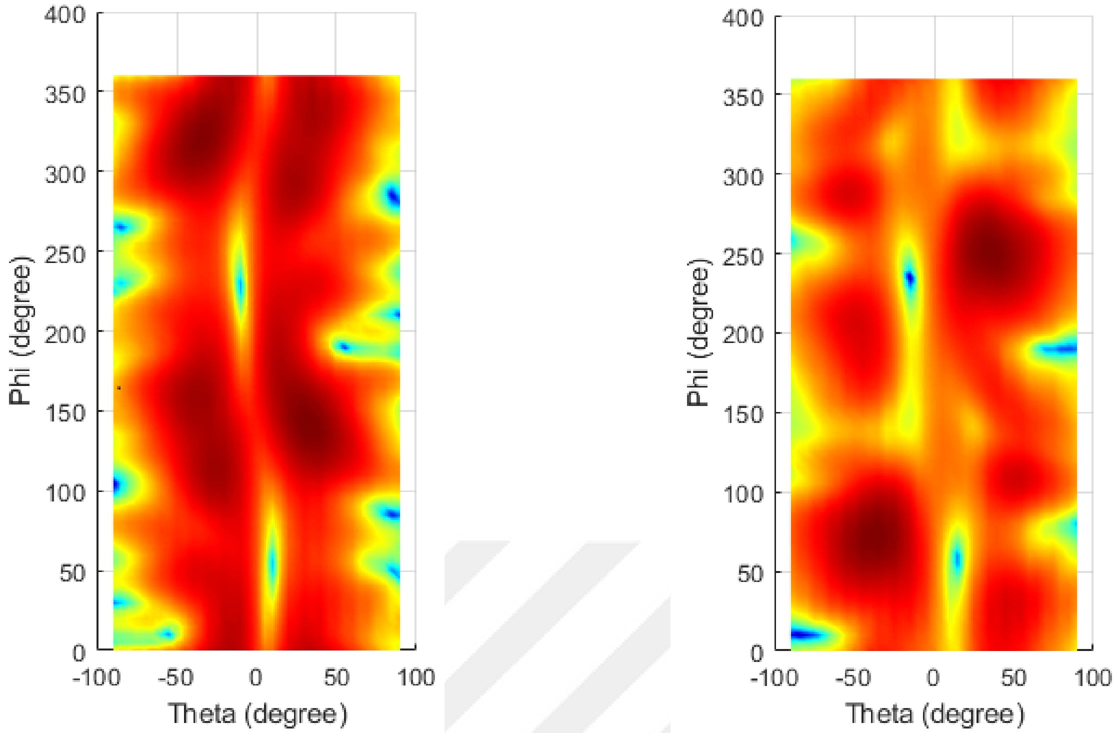

(a) Port 1 Pol 1 (b) Port 1 Pol 2

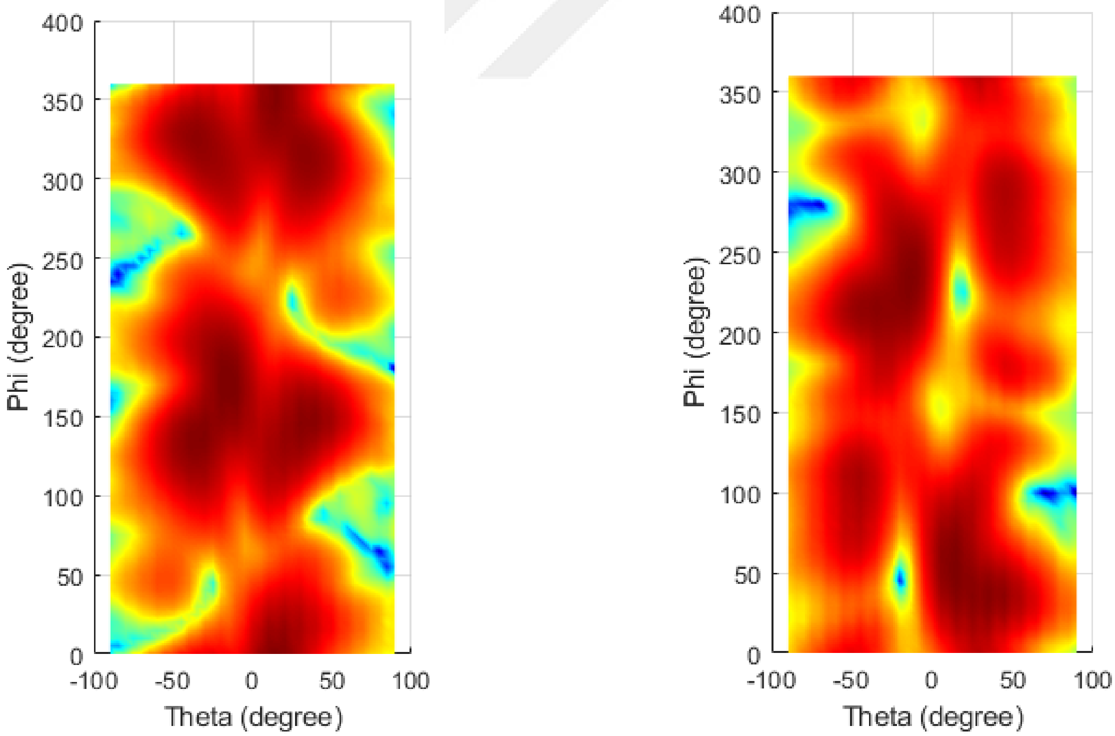

(c) Port 2 Pol 1 (d) Port 2 Pol 2

Figure 4.35 3D radiation patterns of OAM antenna with circular polarization at 6.85 GHz

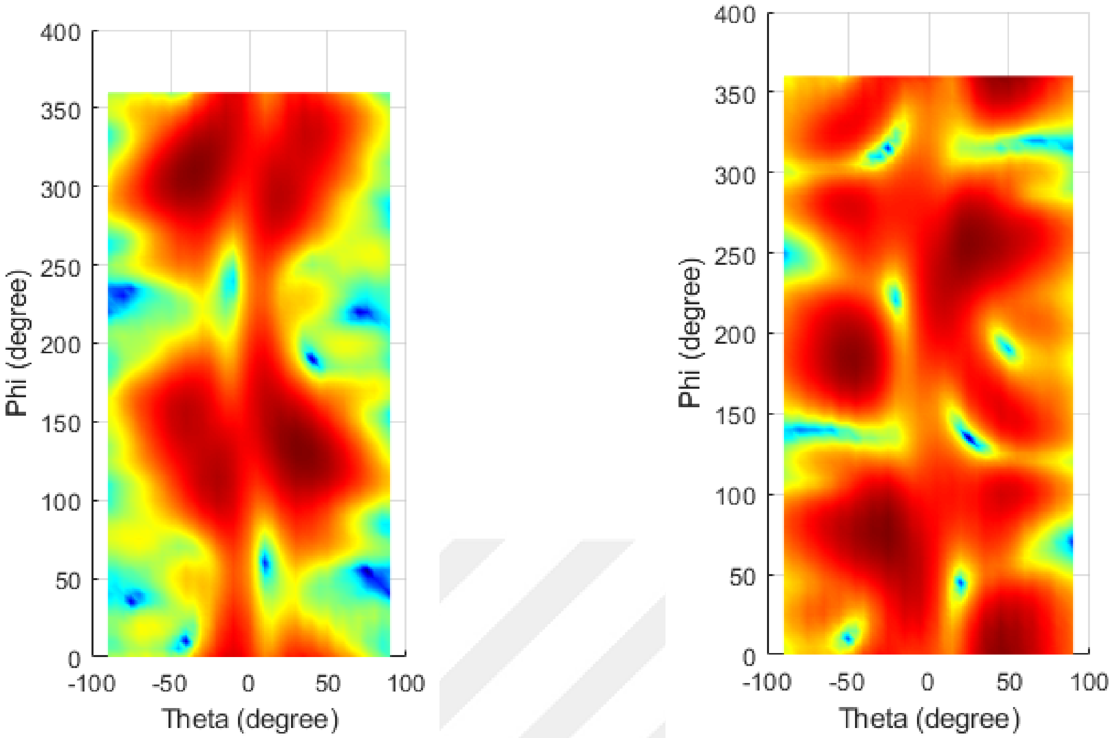

(a) Port 1 Pol 1 (b) Port 1 Pol 2

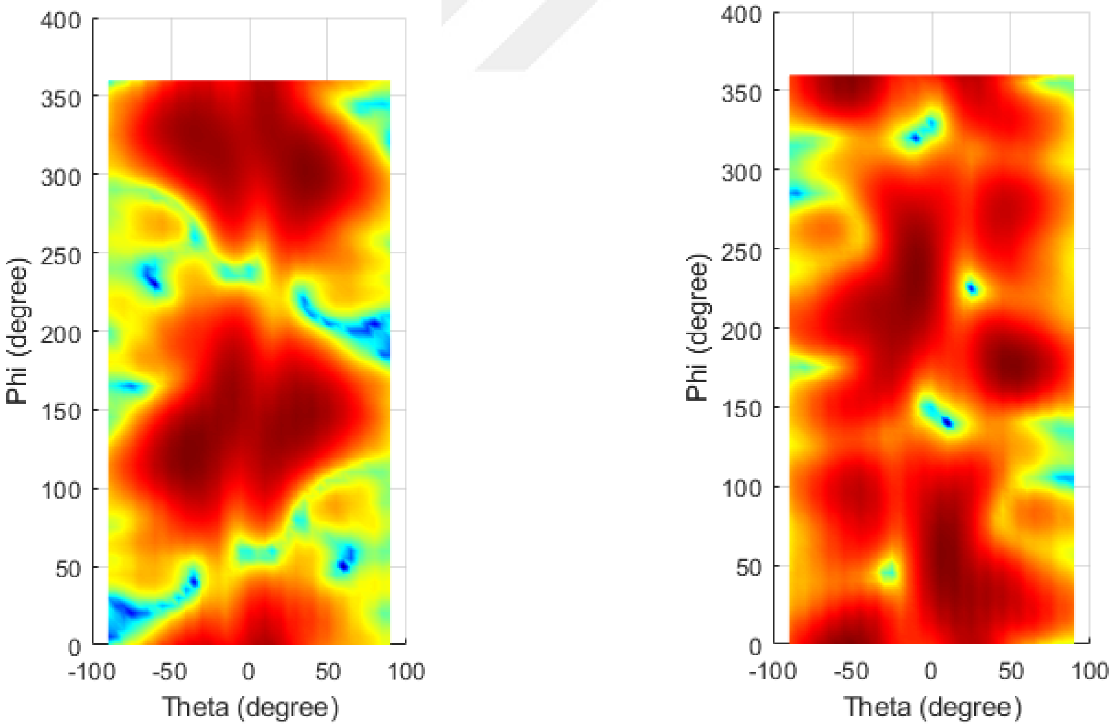

(c) Port 2 Pol 1 (d) Port 2 Pol 2

Figure 4.36 3D radiation patterns of OAM antenna with circular polarization at 6.95 GHz

The 2D radiation patterns of OAM antenna with circular polarization at the same frequencies for distinct polarizations and ports are shown in figures 4.37, 4.38, 4.39 and 4.40. Again, the ϕ values that singularities occur are detected from rectangular 3D radiation figures, and slices are taken from those angles to create 2D radiation pattern plots. At some ϕ angles, it is frankly seen that the radiation intensity immensely decreases for explicit θ angles. This confirms that the circularly polarized uniform circular array antenna can generate OAM modes successfully.

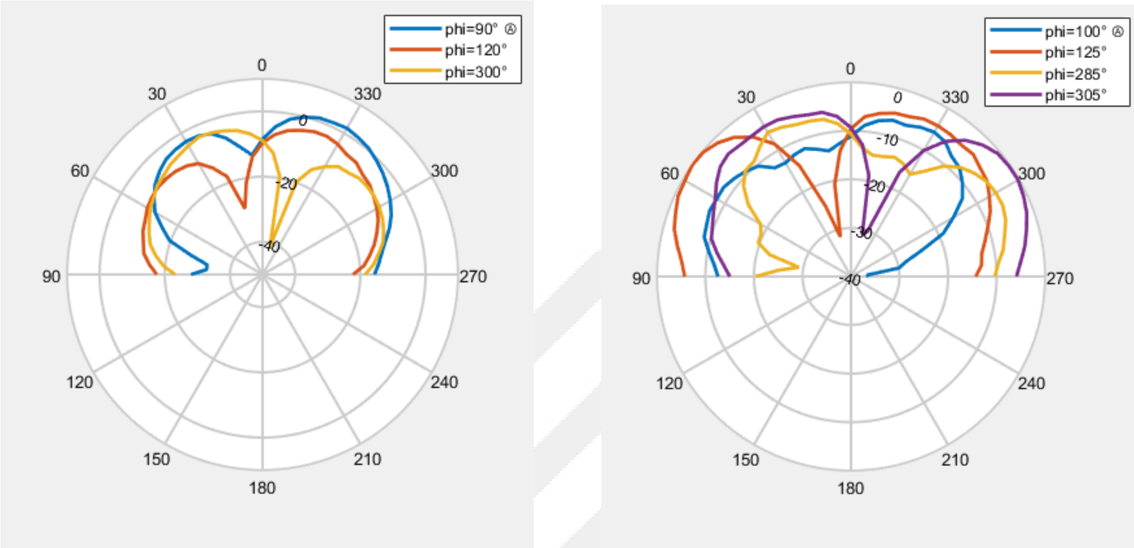

(a) Port 1 Pol 1

(b) Port 1 Pol 2

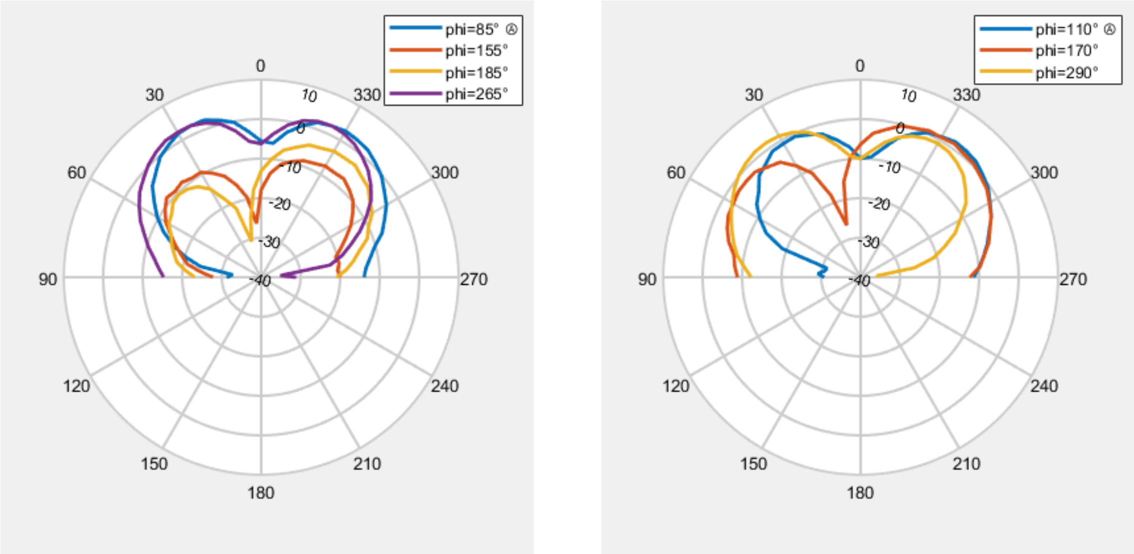

(c) Port 2 Pol 1

(d) Port 2 Pol 2

Figure 4.37 2D radiation patterns of OAM antenna with circular polarization at 6.65 GHz

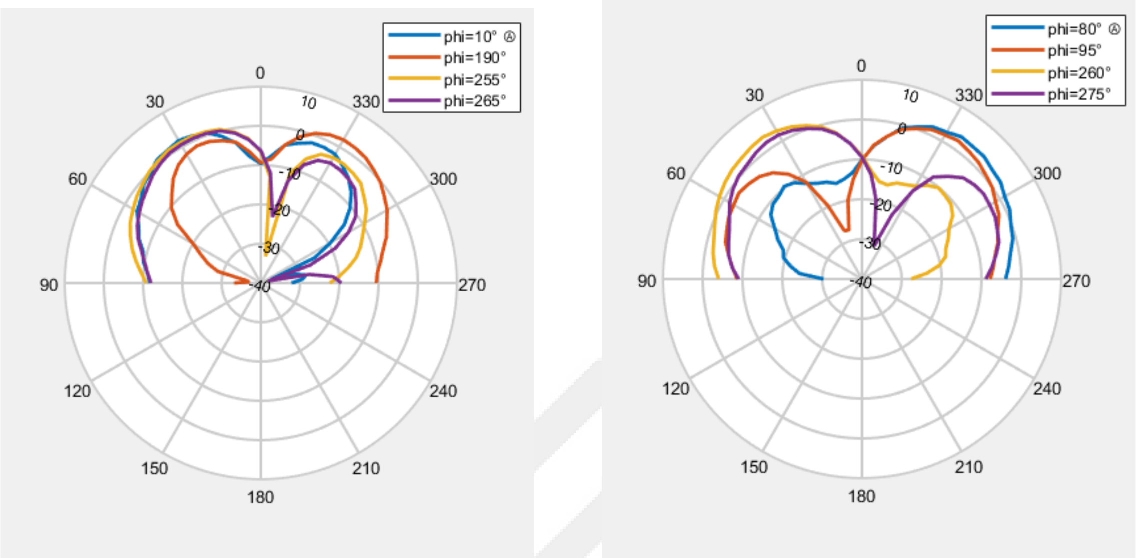

(a) Port 1 Pol 1 (b) Port 1 Pol 2

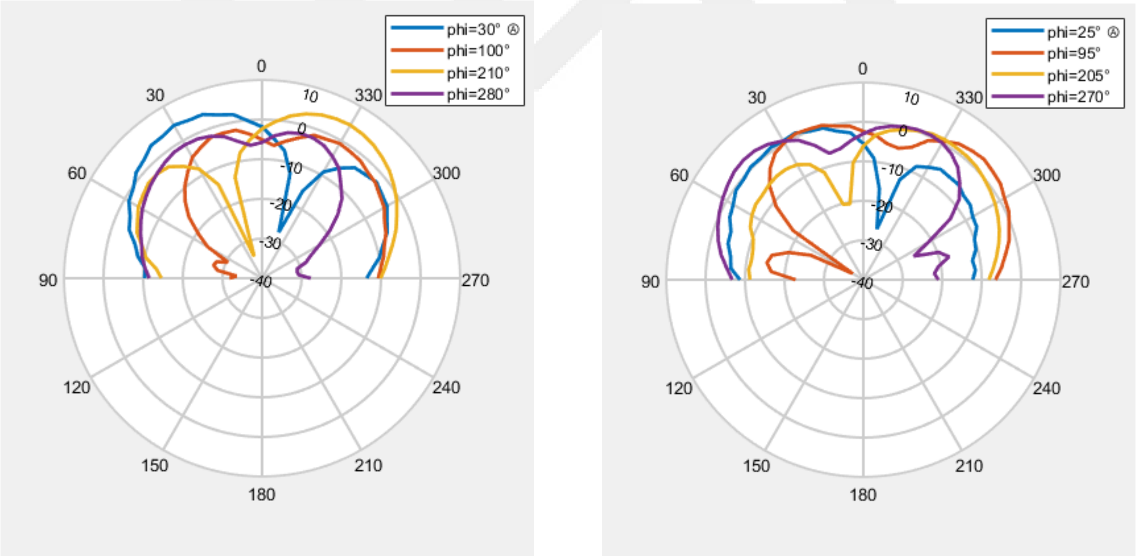

(c) Port 2 Pol 1 (d) Port 2 Pol 2

Figure 4.38 2D radiation patterns of OAM antenna with circular polarization at 6.75 GHz

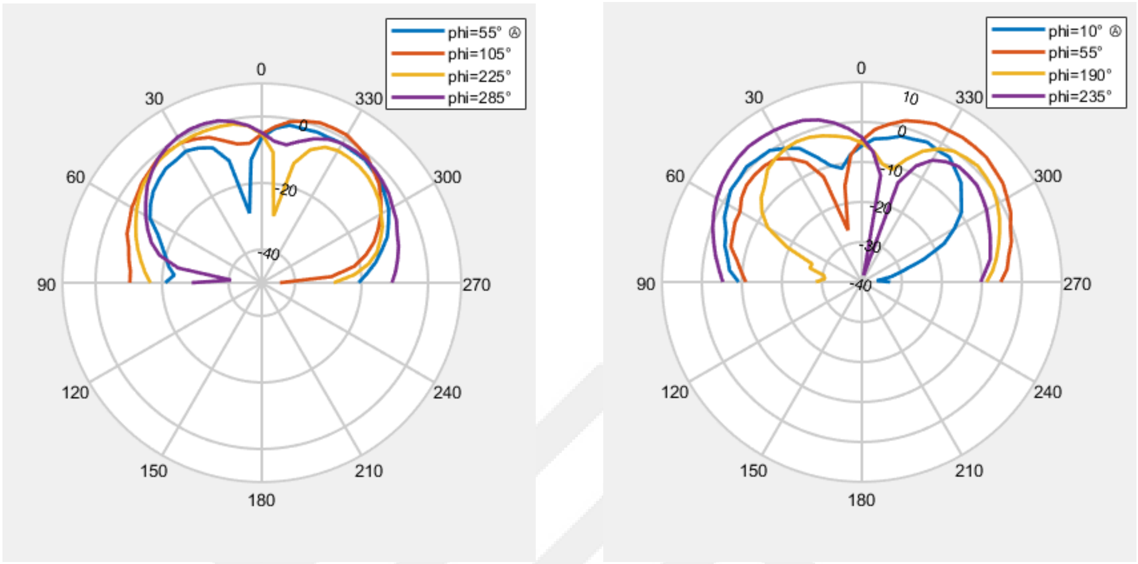

(a) Port 1 Pol 1 (b) Port 1 Pol 2

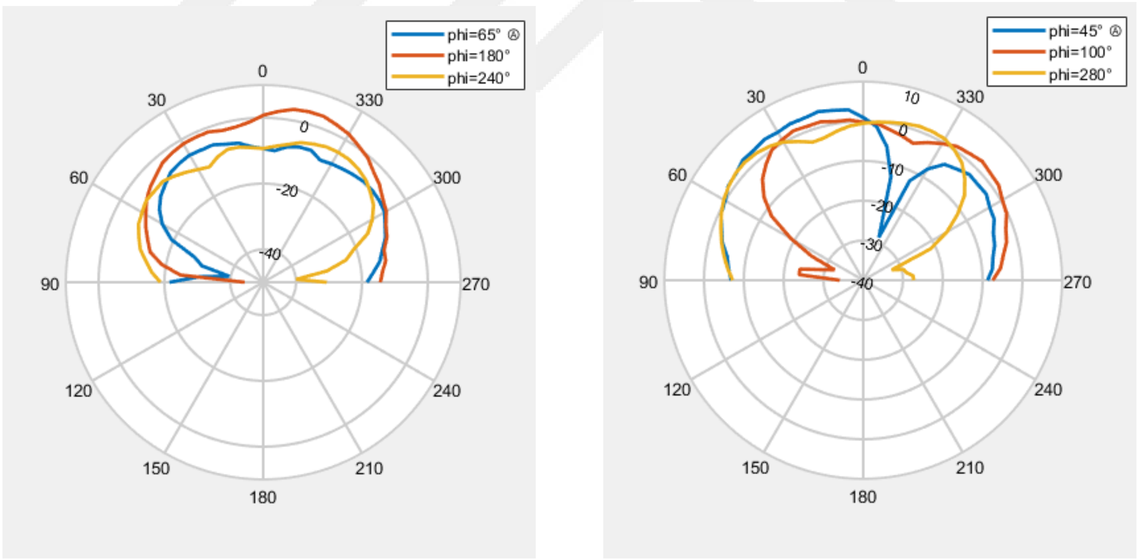

(c) Port 2 Pol 1 (d) Port 2 Pol 2

Figure 4.39 2D radiation patterns of OAM antenna with circular polarization at 6.85 GHz

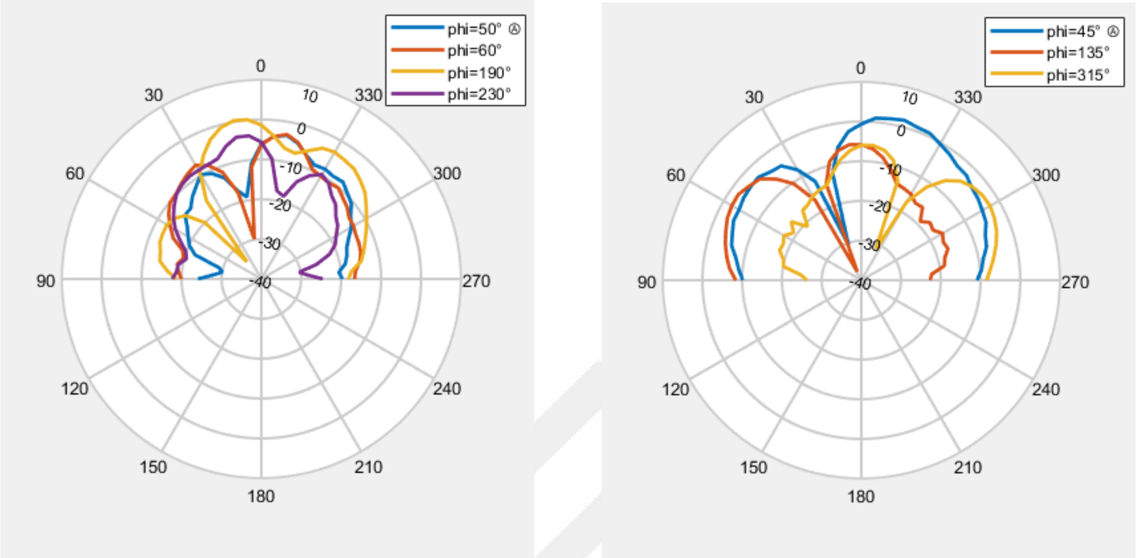

(a) Port 1 Pol 1 (b) Port 1 Pol 2

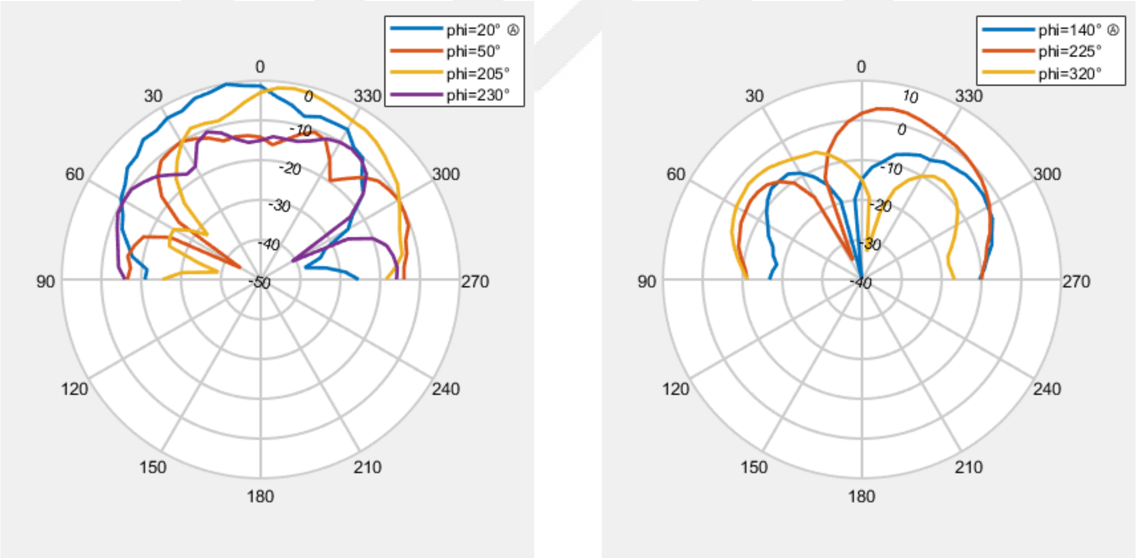

(c) Port 2 Pol 1 (d) Port 2 Pol 2

Figure 4.40 2D radiation patterns of OAM antenna with circular polarization at 6.95 GHz

5. CONCLUSION AND FUTURE WORKS

This thesis explored the design, fabrication, and performance evaluation of uniform circular array antennas capable of generating Orbital Angular Momentum (OAM) at the 6.5 GHz Wi-Fi band. Two UCA antennas of 4-array elements with linear and circular polarizations that generate two OAM modes were designed. The OAM antennas were fabricated using a low-cost PCB prototyping technique, ensuring high precision and accuracy, with an LPKF Circuit Board Plotter ProtoMat S63 at Sabancı University CoSpace.

Extensive measurements were conducted in the anechoic chamber facility at Sabancı University Nano Technology Center (SUNUM) using NSI2000 antenna measurement software. These measurements validated the performance of the fabricated antennas using gain plots, s-parameters vs. frequency plots, phase patterns, and radiation patterns obtained.

In the case of the linearly polarized Uniform Circular Array (UCA) antenna, the return loss at 7 GHz was measured to be -24.95 dB when port P1 was excited and -32.13 dB when port P2 was excited. The corresponding bandwidth was approximately 220 MHz, with a gain of 5.7 dBi. For the circularly polarized UCA antenna, the return loss at 7 GHz was -14.07 dB for P1 excitation and -18.88 dB for P2 excitation. The bandwidth for this configuration was approximately 260 MHz, with a gain of 5.7 dBic at the same frequency. These results demonstrate comparable gain values between both configurations, with the circularly polarized UCA exhibiting a slightly wider bandwidth at the specified frequency.

The designed antennas demonstrated effective OAM generation for linearly and circularly polarized UCA antennas. The comparison between linearly and circularly polarized UCA antennas highlighted the differences in their phase patterns. The circularly polarized UCA antenna doubled the capacity in both orthogonal components E_x and E_y, while the linearly polarized UCA antenna improved spectral efficiency for only E_y component.

Generating OAM with uniform circular array antennas showed potential for capacity enhancement and improved spectral efficiency in wireless communication systems. The findings contribute to advancing state-of-the-art antenna design and wireless communication technologies.

Building on the achievements of this research, several directions for future work are proposed. One direction is the development of a 4-port antenna with additional cross transmission lines to explore further enhancements in OAM generation. Another avenue is to increase the number of circular array elements to increase the OAM mode number and investigate the effects on overall antenna performance.

The insights and methodologies developed in this thesis lay a strong foundation for future research in OAM and antenna design, paving the way for innovative solutions in next-generation wireless communication technologies.

BIBLIOGRAPHY

[1] Terabit free-space data transmission employing orbital angular momentum multiplexing. *Nature Photonics*, 2012.

[2] L. Allen, M. W. Beijersbergen, R. J. C. Spreeuw, and J. P. Woerdman. Orbital angular momentum of light and the transformation of laguerre-gaussian laser modes. *Phys. Rev. A*, 45(11):8185–8189, June 1992. doi: 10.1103/PhysRevA.45.8185.

[3] Q. Bai, A. Tennant, E. Cano, and B. Allen. An experimental phased array for oam generation. In *2014 Loughborough Antennas and Propagation Conference (LAPC)*, pages 165–168, 2014. doi: 10.1109/LAPC.2014.6996347.

[4] Qiang Bai, Alan Tennant, Ben Allen, and Masood Ur Rehman. Generation of orbital angular momentum (oam) radio beams with phased patch array. In *2013 Loughborough Antennas Propagation Conference*, pages 379–382, Loughborough, UK, Nov 2013. IEEE. doi: 10.1109/LAPC.2013.6711915.

[5] X. Bai et al. Experimental array for generating dual circularly-polarized dual-mode oam radio beams. *Sci. Rep.*, 7:1–8, 2017. doi: 10.1038/srep40099.

[6] Constantine A. Balanis. *Antenna Theory: Analysis and Design.* John Wiley & Sons, Hoboken, NJ, 3rd edition, 2005.

[7] L. Basics and H. Suyari. A study of radio frequency orbital angular momentum generation by non-reflective components. *IEEE Transactions on Antennas and Propagation*, 67(12):7820–7829, 2019.

[8] B. Basu and A. K. Agrawal. *Electromagnetic Vortices: Wave Phenomena and Engineering Applications.* Wiley, 2023. doi: 10.1002/9781119662945.ch1.

[9] R. A. Beth. Mechanical detection and measurement of the angular momentum of light. *Physical Review*, 50:115–125, 1936.

[10] Z. Bomzon, G. Biener, V. Kleiner, and E. Hasman. Radially and azimuthally polarized beams generated by space-variant dielectric subwavelength gratings. *Optics Letters*, 27(5):285–287, 2001.

[11] W. Cheng, W. Zhang, H. Jing, S. Gao, and H. Zhang. Orbital angular momentum for wireless communications. *IEEE Wireless Communications*, 2018.

[12] Robert E. Collin. *Antennas and Radiowave Propagation.* McGraw-Hill, New York, NY, 1985.

[13] Douglas C. Giancoli. *Physics for Scientists and Engineers with Modern Physics.* Pearson Prentice Hall, Upper Saddle River, NJ, 4th edition, 2008. ISBN 9780131495081.

[14] Y. Gong. Generation and transmission of oam-carrying vortex beams using circular antenna array. *IEEE Transactions on Antennas and Propagation*, 2017.

[15] David J. Griffiths. *Introduction to Electrodynamics*. Prentice Hall, 3rd ed edition, 1999. ISBN 013805326X,9780138053260,9780139199608,0139199608.

[16] Y. Huang, X. Li, Q. Li, et al. Generation of broadband high-purity dual-mode oam beams using a four-feed patch antenna: Theory and implementation. *Scientific Reports*, 9:12977, 2019. doi: 10.1038/s41598-019-49377-6.

[17] Y. Huang, C. Chen, S. Zhang, W. Zhang, H. Yang, and X. Fang. Optimal design of flat phase plates for radio orbital angular momentum (oam) generation. *IEEE Access*, 8:159337–159347, 2020.

[18] Z. H. Jiang and D. H. Werner. *Electromagnetic Fields Carry Orbital Angular Momentum*. Wiley-IEEE Press, 2022.

[19] Patan Imran Khan. Introduction to ultra-wideband antennas. *Pacific International Journal*, 01(04), April 2018. ISSN 2616-4825. URL https://core.ac.uk/download/480543559.pdf.

[20] K. Kona and Y. Rahmat-Samii. Novel probe-feeding architectures for stacked microstrip patch antennas. *Microwave and Optical Technology Letters*, 39(6): 471–476, 2003. doi: 10.1002/mop.11092. URL https://doi.org/10.1002/mop.11092.

[21] Yan Liu, Jin-Liang Bai, Bing Xiao, Rui Zhao, Qiwen Qiu, Xi Chen, Bo Wang, and Yue Zhao. Orbital-angular-momentum-based electromagnetic vortex imaging. *IEEE Antennas and Wireless Propagation Letters*, 14:711–714, 2015.

[22] LPKF Laser Electronics AG. Lpkf protomat: In-house pcb prototyping, n.d. URL https://www.lpkf.com/en/industries-technologies/research-in-house-pcb-prototyping/products/lpkf-protomat.

[23] P. Mahmouli and S. J. Walker. Holography-based generation of radio orbital angular momentum modes. *IEEE Transactions on Antennas and Propagation*, 66(8):4010–4019, 2018.

[24] Robert J Mailloux, editor. *Phased Array Antenna Handbook*. Artech House, 2nd edition, 2015.

[25] Medit-Tech. Nsi-mi-nsi2000 standard edition, n.d. URL https://medit-tech.it/PDF/NSI-MI-NSI2000-Standard-Edition.pdf.

[26] S Michael Mohammadi, LKS Daldorff, JE Bergman, ME Gushchin, R Surutka, Bo Thidé, and K Forozesh. Orbital angular momentum in radio: Measurement methods. *IEEE Transactions on Antennas and Propagation*, 58(2):565–572, 2010.

[27] Fabien Niel. *Orbital Angular Momentum of Light: A State of the Art*, pages 193–210. Springer International Publishing, Cham, 2021. ISBN 978-3-030-73547-0. doi: 10.1007/978-3-030-73547-0_9. URL https://doi.org/10.1007/978-3-030-73547-0_9.

[28] NSI-MI Technologies. 5.85 GHz to 8.2 GHz WR137 Standard Gain Horn, 2024. URL https://store.nsi-mi.com/5-85-ghz-to-8-2-ghz-wr137-standard-gain-horn/.

[29] J.H. Poynting. The wave motion of a revolving shaft, and a suggestion as to the angular momentum in a beam of circularly polarised light. *Proceedings of the Royal Society of London*, 82(557):560–567, 1909.

[30] David M. Pozar. *Microwave Engineering*. Wiley, Hoboken, NJ, 2012.

[31] Amphenol RF. 132143 bnc straight crimp plug for rg-58 cable, n.d. URL https://www.amphenolrf.com/132143.html. Accessed: 2024-09-08.

[32] Rogers Corporation. RO4000 Laminates RO4003C and RO4350B - Data Sheet, 2024. URL https://www.rogerscorp.com/advanced-electronics-solutions/ro4000-series-laminates/ro4003c-laminates.

[33] Sabancı University Nanotechnology Research and Application Center. Lpkf circuit board plotter protomat s63, n.d. URL https://cospace.sabanciuniv.edu/en/equipment/lpkf-circuit-board-plotter-protomat-s63-0.

[34] Amit Sharma, Rajni Sharma, Mayur Agarwal, and Abneesh Kumar. Design and simulation of single band rectangular patch antenna. *International Journal of Advance Research and Innovation*, 2(1):86–88, 2014. ISSN 2347-3258. URL https://core.ac.uk/download/357254040.pdf.

[35] Sourabh Singhroha, Naman Gaur, Chaitanya Sharma, Nilanjan Mukherjee, Bimal Raj Dutta, and Ashutosh Tripathi. Improved microstrip patch antenna design for x band communication at 10 ghz. EasyChair Preprint 11414, EasyChair, 2023.

[36] E. Skafidas and R. Evans. Antenna effects on the capacity of mimo communications systems in rayleigh channels. In *Proceedings of the 2004 IEEE 15th International Symposium on Personal, Indoor and Mobile Radio Communications*, 2005. doi: 10.1109/pimrc.2004.1370944. URL https://doi.org/10.1109/pimrc.2004.1370944.

[37] Warren L. Stutzman and Gary A. Thiele. *Antenna Theory and Design*. Wiley, New York, NY, 2nd edition, 1997.

[38] Fabrizio Tamburini, Enrico Mari, Alessandra Sponselli, Bo Thidé, Andrea Bianchini, and Filippo Romanato. Encoding many channels on the same frequency through radio vorticity: First experimental test. *New Journal of Physics*, 14: 033001, 2012. doi: 10.1088/1367-2630/14/3/033001.

[39] B. Thidé, F. then Avallone, B. then G., J. then Lindgren, V. then B., K. then Eriksson, and E. then D. Utilization of photon orbital angular momentum in the low-frequency radio domain. *Physical Review Letters*, 99(4):1762–1765, 2007.

[40] A. Uzun and I. Tekin. Series-fed dual-mode oam antenna at 6 ghz. In *2024 IEEE International Symposium on Antennas and Propagation and ITCN-USNC-URSI Radio Science Meeting*, pages 2495–2496, Florence, Italy, 2024.

[41] Harry L Van Trees. *Optimum Array Processing: Part IV of Detection, Estimation, and Modulation Theory*. Wiley, 2002.

[42] W. Wei, K. Mahdjoubi, C. Brousseau, and O. Emile. Generation of oam waves with circular phase shifter and array of patch antennas. *Electron. Lett.*, 51(6): 442–443, 2015. doi: 10.1049/el.2014.4425.

[43] Alison Yao and Miles Padgett. Orbital angular momentum: Origins, behavior and applications. *Advances in Optics and Photonics*, 3:161–204, 06 2011. doi: 10.1364/AOP.3.000161.

[44] Nan Yu, Tiezhu Cai, Yuan Cheng, Qian Zhao, and Xianshan Luo. Holographic generation of tunable orbital angular momentum vortex beams at millimeter wavelengths. *Optics Express*, 27(9):12213–12222, 2019.

[45] Rui Zhang, Lei Zhu, and Yu Wang. Orbital angular momentum modes generation and detection using uniform circular arrays. *IEEE Transactions on Antennas and Propagation*, 64(10):4080–4090, 2016.